NUREG/CR-6161
IS-5103

Buckling Evaluation of System 80+™ Containment

Prepared by
L. Greimann, F. Fanous, S. Safar, R. Challa, D. Bluhm

Ames Laboratory
Iowa State University

Prepared for
U.S. Nuclear Regulatory Commission

AVAILABILITY NOTICE

Availability of Reference Materials Cited in NRC Publications

Most documents cited in NRC publications will be available from one of the following sources:

1. The NRC Public Document Room, 2120 L Street, NW., Lower Level, Washington, DC 20555-0001

2. The Superintendent of Documents, U.S. Government Printing Office, Mail Stop SSOP, Washington, DC 20402-9328

3. The National Technical Information Service, Springfield, VA 22161

Although the listing that follows represents the majority of documents cited in NRC publications, it is not intended to be exhaustive.

Referenced documents available for inspection and copying for a fee from the NRC Public Document Room include NRC correspondence and internal NRC memoranda; NRC bulletins, circulars, information notices, inspection and investigation notices; licensee event reports; vendor reports and correspondence; Commission papers; and applicant and licensee documents and correspondence.

The following documents in the NUREG series are available for purchase from the GPO Sales Program: formal NRC staff and contractor reports, NRC-sponsored conference proceedings, international agreement reports, grant publications, and NRC booklets and brochures. Also available are regulatory guides, NRC regulations in the *Code of Federal Regulations*, and *Nuclear Regulatory Commission Issuances*.

Documents available from the National Technical Information Service include NUREG-series reports and technical reports prepared by other Federal agencies and reports prepared by the Atomic Energy Commission, forerunner agency to the Nuclear Regulatory Commission.

Documents available from public and special technical libraries include all open literature items, such as books, journal articles, and transactions. *Federal Register* notices, Federal and State legislation, and congressional reports can usually be obtained from these libraries.

Documents such as theses, dissertations, foreign reports and translations, and non-NRC conference proceedings are available for purchase from the organization sponsoring the publication cited.

Single copies of NRC draft reports are available free, to the extent of supply, upon written request to the Office of Administration, Distribution and Mail Services Section, U.S. Nuclear Regulatory Commission, Washington, DC 20555-0001.

Copies of industry codes and standards used in a substantive manner in the NRC regulatory process are maintained at the NRC Library, 7920 Norfolk Avenue, Bethesda, Maryland, for use by the public. Codes and standards are usually copyrighted and may be purchased from the originating organization or, if they are American National Standards, from the American National Standards Institute, 1430 Broadway, New York, NY 10018.

DISCLAIMER NOTICE

For sale by the U.S. Government Printing Office
Superintendent of Documents, Mail Stop: SSOP, Washington, DC 20402-9328
ISBN 0-16-045217-1

NUREG/CR-6161
IS-5103

Buckling Evaluation of System 80+™ Containment

Manuscript Completed: June 1994
Date Published: August 1994

Prepared by
L. Greimann, F. Fanous, S. Safar, R. Challa, D. Bluhm

Ames Laboratory
Iowa State University
Ames, IA 50011

Prepared for
Division of Engineering
Office of Nuclear Reactor Regulation
U.S. Nuclear Regulatory Commission
Washington, DC 20555-0001
NRC FIN L2582

ABSTRACT

The System 80+™ containment may be subjected to compressive forces which could cause it to become unstable. The stability of the containment shell under prescribed loading combinations was investigated with two analysis levels: axisymmetric and three dimensional.

An axisymmetric shell model, including additional mass to account for penetrations and the spray header system, was analyzed using BOSOR4 and BOSOR5 finite difference codes. Loading combinations with pressure, temperature, self weight, and seismic satisfied the American Society of Mechanical Engineers (ASME) stress allowables. The buckling assessment was performed using the worst meridian assumption, including material nonlinearities and a sinusoidal axisymmetric imperfection. The minimum factor of safety for Service Level C was 2.35. A SSE seismic margin of 2.91 was calculated.

The ABAQUS finite element code was selected for the three dimensional analysis and tested with classical and BOSOR solutions. The three dimensional model included the equipment hatch, two personnel airlocks, and additional mass for the spray system and small penetrations. Material nonlinearity and an axisymmetric sinusoidal imperfection were incorporated. Several vibration modes contained large local vibrations near the equipment hatch and personnel airlocks. The maximum structural response was computed using response spectrum analysis and six potential buckling regions were identified. A set of equivalent static loads was determined for each of the six regions to regenerate the maximum SRSS stress resultants. For each region, combined loads were increased until an instability was detected. A minimum factor of safety of 1.91 was predicted, which does not satisfy ASME Section NE3222.1 or Regulatory Guide 1.57. Code Case N-284 is satisfied. The analysis is conservative primarily because the SRSS 10% method provides a conservative estimate of modal coupling.

TABLE OF CONTENTS

LIST OF TABLES

LIST OF FIGURES

ACKNOWLEDGMENT

The authors would like to express their appreciation for the members of the U.S. Nuclear Regulatory Commission, Dr. Syed A. Ali (Project Officer), Mr. Goutam Bagchi (Branch Chief, Structural and Geosciences), and Mr. Bernard L. Grenier, (Program Manager, Division of Engineering) for their help throughout the course of this work. The authors would also like to acknowledge the project Secretaries, Ms. Jeanine Crosman and Ms. Denise Wood for word processor operations and secretarial services associated with this project. Additionally, they would like to thank Ms. Connie Bates, Administrative Specialist for her assistance on financial planning and tracking.

EXECUTIVE SUMMARY

The System 80+™ containment is a spherical structure of thin steel plates with large radii of curvature. It is embedded in concrete at its base with a flexible transition zone. As it is subjected to various loading conditions, certain regions of the shell are subjected to compressive forces which may cause the shell to become unstable. The objective of this project is to investigate the stability of the containment shell under prescribed loading combinations including pressure, temperature, self weight, and seismic loads. Two basic levels of analysis were used to achieve the objective: an axisymmetric shell analysis and a three dimensional shell analysis of six critical regions.

An axisymmetric shell model, which consisted of several segments subdivided into mesh points, was formulated for the BOSOR4 and BOSOR5 finite difference software. Additional mass was smeared around the model to account for penetrations and the spray header system. The flexible material in the transition region between the steel shell and concrete base was modelled using elastic springs. The stresses due to the individual loads were computed using BOSOR4. The most recent Safe Shutdown Earthquake (SSE) seismic response spectra were used (7/7/93). Modal stresses were combined by the Square Root of the Sum of the Squares (SRSS) 10% method and directional components were combined with the SRSS method. Loading cases were combined as per Standard Review Plan Section 3.8.2 and the resulting stresses were found to satisfy the American Society of Mechanical Engineers (ASME) allowables for Service Level A, C, and D.

Stability was investigated using BOSOR5 with the axisymmetric model. The buckling assessment was performed using the worst meridian assumption, that is, the stresses on the most highly stressed meridian were assumed to exist uniformly around the circumference. Material nonlinearities and residual stresses were incorporated using a stress-strain constitutive relationship derived from the ASME Code Case N-284. A geometric axisymmetric imperfection was introduced into the model in the form of a sine wave. The amplitude of the sine wave satisfied ASME construction tolerances and the wave length was selected to minimize the buckling factor of safety. A minimum factor of safety for Service Level C was calculated to be 2.35, which does not satisfy ASME Section NE3222.1 but does satisfy Code Case N-284 and Regulatory Guide 1.57.

A buckling analysis under seismic loading beyond SSE was also conducted using the axisymmetric model. Dead load was held constant and the seismic loading was increased by a factor of 2.91 at which point buckling occurred.

The ABAQUS finite element code was selected for the three dimensional shell analysis, primarily on the basis of its superior nonlinear solution techniques. ABAQUS capabilities were tested by analyzing elastic buckling of two shells, a perfect cylinder and a perfect sphere, and comparing the results to classical shell buckling theory. It was further validated by comparing its results to those of BOSOR5 for three spherical shell cases: uniform loading (external pressure), gradient loading (self weight), and concentrated loading on an equipment hatch penetration. Mesh size was also selected using these problems.

The complete three dimensional model of the containment included the equipment hatch and two personnel airlocks. Additional masses were added for the small penetrations and the spray system. The material model was the same at that used as in the axisymmetric analysis. An axisymmetric sinusoidal imperfection which satisfied ASME criteria was incorporated. The wave length of the imperfection corresponded to the minimum buckling factor of safety from the axisymmetric analysis. The conditions at the base were modeled to simulate a limited outward movement, as permitted by the flexible material, and no inward movement.

For the seismic analysis, twenty vibration modes were determined, several of which contained large local vibrations near the equipment hatch and personnel airlocks. Modal responses were combined by the SRSS 10% method. Locally high accelerations occurred near the penetrations. The SRSS 10% method, which accounts for modal coupling of closely spaced modes, predicted that the maximum meridional stress resultants varied between 15,940 lb/in. and 11,300 lb/in. around the circumference at the base. The SRSS method without the 10% rule gave an approximately uniform value of 11,300 lb/in. Six areas with locally high compressive stresses were identified: three locations near the base, the two personnel air locks, and the equipment hatch. A set of equivalent static loads was determined for each region which regenerated the maximum SRSS stress resultants within the region.

Pressure, temperature, and self-weight loadings were added to the equivalent seismic loadings. For each region, loads were increased until an instability was detected by ABAQUS. The minimum factor of safety of 1.91 was predicted for buckling near the base. Local buckling near the equipment hatch and personnel air locks did not control. The factor of 1.91 does not satisfy ASME Section NE3222.1 or Regulatory Guide 1.57. Code Case N-284 is satisfied. The analysis is conservative primarily because the SRSS 10% method provides an overly conservative estimate of modal coupling for shell type of structures.

1. INTRODUCTION

1.1 Background

The System 80+™ containment is a spherical structure of thin steel plates with large radii of curvature. It is embedded in concrete at its base with a flexible transition zone (see Fig. 1.1). As the containment is subjected to various loading conditions, regions of compressive membrane forces develop in the steel containment which may cause the shell to become unstable. For the containment to perform its intended safety function and sustain these loads, a sufficient margin of safety against buckling should exist.

1.2 Objectives

The objectives of the present work are to perform:

(1) An axisymmetric stress/buckling analysis of the containment with a new response spectra revised from that in a previous study [Ref. 1.1].

(2) A three dimensional buckling analysis for the effects of localized loads near penetrations such as the equipment hatch and personnel locks.

(3) An axisymmetric analysis to investigate the containment stability beyond the Safe Shutdown Earthquake (SSE).

1.3 Description of System 80+™ Containment

A cross sectional elevation and a plan view of System 80+™ containment are shown in Fig. 1.1. The containment consists of a free-standing spherical steel (SA537-class 2) shell with an inner radius of 100 ft. and a wall thickness of 1.75 in. The containment is embedded in concrete foundation below elevation 91'-9". The portion of the containment building up to elevation 90'-3" is embedded in a concrete foundation (see Fig. 1.2). Between elevation 90'-3" and 91'-9" the vessel has concrete on the inside and cork material of thickness 2.0 in. on the outside. In the transition region, the containment shell thickness was increased to 2 in. to allow for corrosion. Above this region thickness the plate thickness is tapered to 1.75 in. The global coordinate

system is shown on the plan view in Fig. 1.1. The X-axis extends in the East direction, the Y-axis extends in the North direction, and the Z-axis is in the upward direction. The x-y plane passes through the equator at Elev. 157 ft. The major appurtenances are the spray header system, an equipment hatch and two personnel air locks.

The spray header system is located on top of the containment and extends down to an elevation 243'-7". It contributes a total weight of 120,000 lb. Between elevation 93'-0" and elevation 139'-7", the containment has several penetrations and appurtenances which contribute a total weight of 80,000 lb. to the weight of the containment.

Details of the equipment hatch are shown in Fig. 1.3. The central line of the equipment hatch barrel is located at elevation 156'-0" and azimuth 150°. The equipment hatch barrel is a circular cylinder with an inner diameter of 22 ft, a length of 6 ft and a wall thickness of 3.75 in. The total weight of the equipment hatch assembly was assumed to be 120,000 lb. The containment shell plates are thickened to 3.5 in. around the penetration to compensate for the opening. Details of the reinforcing collar around the hatch barrel are shown in Fig. 1.3. The thicker plate is tapered to 1.75 in. over a transition zone of 10 in., which satisfies the ASME code [Ref. 1.7 paragraph NE3361].

Details of the upper and the lower air locks are illustrated in Fig. 1.4. The personnel air locks consist of a circular cylinder with inner diameter of 10 ft, wall thickness of 2.5 in. and length of 18 ft. The central line of the upper air lock is located at elevation 149'-0" and azimuth 225° while that of the lower air lock is located at elevation 118'-0" and azimuth 20°. The weight of each air lock was assumed to be 50,000 lb. The thickness of the reinforcing collar around both air locks is 3.5 in. tapered to 1.75 in. The width of the transition zone was assumed to be 10 in. The centroid of the lower air lock barrel coincides with the middle surface of the steel vessel. However, the centroid of the upper air lock was located outside the containment at a distance of 4 ft. from the vessel wall middle surface. There is an additional support provided outside the containment to reduce bending stresses in the sphere due to gravity loads.

1.4 Methodology

The methodology for the axisymmetric analysis is presented in Section 1.3 of Ref. 1.1. Utilizing the same axisymmetric model as in Ref. 1.1 and the BOSOR4 and BOSOR5 programs, objectives 1 and 3 outlined above were accomplished. The stress intensities for the load combinations specified in Section 3.8.2 of U.S. Nuclear Regulatory Commission Standard Review Plan (U.S. NRC SRP) [Ref. 1.2], were checked with respect to the allowable values for different service limits as per the American Society of Mechanical Engineers (ASME) Boiler and Pressure vessel code [Ref. 1.3]. The critical load combination, i.e., the combination with the largest compressive stress in the containment, was used for the buckling analysis. An axisymmetric sinusoidal imperfection was incorporated into the model. The material constitutive model was derived from the equations of the plasticity reduction factor as described in Ref. 1.1. The critical buckling load was obtained by minimizing the buckling load with respect to the imperfection wavelength.

The nonaxisymmetric stresses were incorporated into an axisymmetric buckling analysis by the worst meridian assumption, i.e., the stresses on the most highly stressed meridian was assumed to exist uniformly around the circumference. The main disadvantage of the axisymmetric analysis is its inadequacy to predict buckling due to localized loads such as those occurring near the equipment hatch and personnel locks. Hence, a three dimensional analysis of the containment was conducted.

Initially, a review of the ANSYS and the ABAQUS three dimensional codes was performed by investigating the ability of the packages to predict the buckling leads for various cases compared to closed form solutions. The packages were evaluated with regard to the choice of elements, analysis techniques, pre- and post-processing capabilities and run times. On the basis of the investigation, the ABAQUS finite element code was selected for the buckling analysis.

The ABAQUS finite element code was further validated with the BOSOR5 program by considering three test cases with spherical shells: uniform loading (external pressure), gradient loading (self weight) and concentrated load on a penetration similar to the equipment hatch. In addition to validating the ABAQUS program, the results were used to determine the mesh size and imperfection wavelength for the three dimensional finite element model for System 80+™.

The containment along with the major appurtenances such as the equipment hatch, personnel airlocks and the spray system was modelled using shell elements. The mass of the penetrations was included in the model. The modal responses due to seismic input of the first twenty modes were determined by a vibration analysis followed by a response spectrum analysis. The modal stress resultants were combined by the Square-Root-of-the-Sum-of-the-Squares (SRSS) ten percent method. Sets of equivalent static loads were developed that produced stress resultants to match the SRSS values in five specific regions. Pressure, thermal and dead loads were added and the buckling behavior of the containment was predicted.

1.5 Acceptance Criteria

The U.S. NRC SRP 3.8.2 [Ref. 1.2] stipulates that the design and analysis procedure for the steel containment structures be in compliance with ASME code [Ref. 1.4], augmented by U.S. NRC Regulatory Guide 1.57 [Ref. 1.5].

1.5.1 Section NE 3222.1

Section NE 3222.1 of the Code specifies the basic allowable compressive stress for the stability of structures as:

> "The maximum buckling stress values to be used for the evaluation of instability shall be either of the following:
>
> (a) One-third the value of critical buckling stress determined by one of the methods given below:
>
> (1) Rigorous analysis which considers the effects of gross and local buckling, geometric imperfections, nonlinearities, large deformations, and inertial forces (dynamic loads only).
>
> (2) Classical (linear) analysis reduced by margins which reflect the difference between theoretical and actual load capacities.
>
> (3) Tests of physical models under conditions of restraint and loading the same as those to which the configuration is expected to be subjected.
>
> (b) The value determined by the applicable rules of NE 3133."

The stability limits for various loading conditions, such as the Design Conditions and Service Limits A, B, C, and D, have the factors of safety listed in Table 1.1. Method (a) (1) will be used here.

1.5.2 ASME Code Case N-284

ASME Code Case N-284 [Ref. 1.6] provides well-defined stability criteria for determining the structural adequacy against buckling of shells with more complex geometries and loading conditions than those covered by Section NE 3133. The rules are based on linear elastic bifurcation buckling theory which has been reduced by knockdown factors to account for the effect of imperfections, boundary conditions, material nonlinearities and residual stresses. The stability limits for the various loading conditions correspond to the factors of safety shown in Table 1.1. The factors of safety are lower than those specified by NE 3222.2 of the Code, but are consistent with other ASME factors of safety for other failure criteria, e.g., yielding due to internal pressure [Ref. 1.7].

1.5.3 Regulatory Guide 1.57

The U.S. NRC Regulatory Guide 1.57 delineates the acceptable design limits and appropriate loading combinations associated with normal operation, postulated accidents and specified seismic events for the design of containment systems. The Regulatory Guide recognizes the design limits as specified in Code Section NE 3222. However, the Guide states that, if a detailed analysis is performed, e.g., Method (a)(1), Note 7 to the regulatory position applies. Note 7 explicitly states that:

> "If a detailed rigorous analysis of shells that contain the maximum allowable deviation from true theoretical form is performed for instability (buckling) due to loadings that induce compressive stresses, such analyses, considering inelastic behavior, should demonstrate that a factor of at least two exists, between the critical buckling stress and the applied stress."

The factor of safety of two against buckling is not associated with a specific Service Limit. However, Regulatory Guide 1.57 states that the loading combinations should encompass that

loading which produces the greatest potential for shell instability. Hence, this factor can be associated with Level C and D Service Limits, which usually produce the greatest compressive stress in the shell since they are associated with the Safe Shutdown Earthquake (SSE) event.

1.6 References

1.1 Greimann, L. et. al., "System 80+™ Containment - Structural Design Review," NUREG-CR/5957, April 1993.

1.2 U.S. NRC Standard Review Plan (SRP), Section 3.8.2, Rev. 1 - July 1981, pp. 3.8.2.4 and 3.8.3.11.

1.3 American Society of Mechanical Engineers, Boiler and Pressure Vessel Code, Section NE 3221 and Table NE-3221-1, 1989.

1.4 American Society of Mechanical Engineers, Boiler and Pressure Vessel Code, Section NE 3222, 1989.

1.5 U.S. Nuclear Regulatory Commission "Regulatory Guide 1.57, Design Limits and Loading Combinations for Metal Primary Reactor Containment Systems Components," NRC, Washington, June 1973.

1.6 American Society of Mechanical Engineers, Boiler and Pressure Vessel Code Case N-284, "Metal Containment Shell Buckling Design Methods," Supplement #2 to Nuclear Code Case Book, 1980.

1.7 ASME Boiler and Pressure Vessel Code Appendix III, paragraphs 2100 and 3100.

2. AXISYMMETRIC ANALYSIS OF SYSTEM 80+™ CONTAINMENT

2.1 Analysis Approach

The axisymmetric analysis of the System 80+™ containment is performed by using the BOSOR4 and BOSOR5 programs. The BOSOR Programs are finite difference codes for analysis of complex branched shells of revolution [Section A.3 of Ref. 2.1]. BOSOR4 can handle both axisymmetric and nonaxisymmetric stress and buckling analyses but is limited to linear material properties. The program can also perform vibration analysis. The BOSOR5 program is developed from the BOSOR4 program and is used for both axisymmetric and nonaxisymmetric buckling analysis with axisymmetric loads including nonlinear material behavior.

Seismic loading which is nonaxisymmetric are expressed by Fourier series. The analysis for seismic loads consists of a vibration analysis as a first step. The modal quantities are determined using the response spectrum method [Section 2.2.4 of Ref. 2.1]. The circumferential variation of modal stresses and stress resultants are expressed by Fourier series and the maximum response along any merdian can be obtained by using the Square-Root-of-the-Sum-of-Squares (SRSS) ten percent method of combining the modal responses [Section A.3.2 of Ref. 2.1].

When BOSOR4 or BOSOR5 is used for stress or buckling analysis, the circumferential variation of the stress resultants is not permitted. Hence, the worst meridian analysis approach is used for analysis of nonsymmetrically loaded shells [Refs. 2.2 and 2.3]. Sections 1330 and 1720 of Code Case N-284 recommends the assumption of uniform stress distribution around the circumference adopted in this approach [Ref. 2.4]. In order to identify the worst meridian for the buckling analysis several meridians must be examined and the worst meridian is identified as the one with the highest stress resultants. In BOSOR4, the analysis is completed by considering the worst meridian stress resultant to be distributed uniformly around the entire circumference. In BOSOR5 direct input of stress resultants is not permitted, and the worst merdian stress resultants must be converted into equivalent axisymmetric pressures for the buckling analysis [Appendix C of Ref. 2.1].

2.2 Stress Analysis

This section summarizes the stress intensities induced in the System 80+™ containment shell by the load combinations specified for Design Conditions and Levels A, B, C, and D as in the SRP 3.8.2 [Ref. 2.5]. The different loads on the structure are the dead load, accident and operating temperatures of 290°F and 110°F, internal pressure of 53 psi and external pressure of 2 psi. The stress intensities reported in Ref. 2.1 were revised to incorporate a change in the internal pressure (revised to 53 psi from 49 psi), elimination of Operating Basis Earthquake (OBE) condition and a revised response spectra for the Safe Shutdown Earthquake (SSE) condition (Fig. 2.1) (transmitted by personal communication from Dr. Syed Ali from NRC dated 5-24-93). The structural analysis of the containment shell was first performed for each individual load case utilizing the BOSOR4 program. The results were combined to calculate the stress intensities for the Design Conditions and Levels A, B, C, and D, which were compared to allowable stress intensities from the ASME Code [Ref. 2.6].

2.2.1 Axisymmetric Modelling of the System 80+™ Containment

The axisymmetric modelling of the System 80+™ containment is described in detail in Section 2.1 of Ref. 2.1.

2.2.2 Individual Load Cases

The maximum stresses induced in the structure due to application of dead load, external pressure of 2 psi and thermal loadings of 110°F and 290°F are discussed in Sections 2.2.1, 2.2.2 and 2.2.3 of Ref. 2.1. The modified uniform pressure loading for System 80+™ is an internal pressure of 53 psi.

The revised response spectra for SSE is illustrated in Fig. 2.1. Two horizontal (X or East and Y or North) and one vertical (Z or up) spectra are shown. The SRSS meridional and circumferential stress resultants, N_{1max} and N_{2max}, for East, Northeast, and North meridians, are shown in Fig. 2.2 and 2.3 respectively. The maximum values of the seismic stress resultants are about 21 percent below those of Fig. 2.9 and 2.10 in Ref. 2.1 because the revised spectral accelerations corresponding to the dominant horizontal modes are about that much lower than the previous values. The meridian with the highest stress resultants, or the worst meridian, was the East meridian.

2.2.3 Combination of Stresses

Section 1.3 of SRP 3.8.2 [Ref. 2.5] stipulates that the design loading combinations be in compliance with Subsection NE, Section III, Division 1 of the ASME Code [Ref. 2.6] and Regulatory Guide 1.57 [Ref. 2.7]. The pertinent load combinations are listed in Tables 2.1 to 2.5 for the Design Condition and Service Levels A, B, C, and D. Table 2.6 defines the nomenclature used in Tables 2.1 to 2.5. In addition, Tables 2.1 to 2.5 refer to the specific SRP 3.8.2 loading combination numbers.

Subsection NE of the ASME Code [Ref. 2.6, (Table NE3221.1)] has established allowable stress intensities for the Design Conditions and Service Levels A, B, C, and D as listed in Tables 2.1 to 2.5. Allowable stresses depend upon the stress classification, i.e., primary or secondary (see Table 2.6). The stress intensities were evaluated for each of the load combinations and the maximum stresses are listed in Tables 2.1 to 2.5.

All the evaluated stress intensity values were below the allowable limits.

2.3 Buckling Analysis

This section summarizes the revised buckling analysis results for the System 80+™ containment. The material constitutive model was derived from the equations of the plasticity reduction factor from Code Case N-284 [Ref. 2.4], following the approach described in Sec. A.3.6.2 of Ref. 2.1. The earlier results as reported in Fig. A.14 of Ref. 2.1 were revised to correct an error. The modified stress-strain curves for SA-537 class 2 steel, corresponding to temperatures of 110°F and 290°F, are shown in Figures 2.4 and 2.5. The analysis was performed to determine the buckling factors of safety for Service Levels A, C, and D. Service Level B was eliminated from analysis since the OBE condition has been eliminated.

2.3.1 Loading and Solution Process

The loading and solution process for the buckling analysis of the containment is summarized in Section 4.1 of Ref. 2.1. The factor of safety against buckling, λ, is a load multiplier which is equal to the ratio of the loads at which buckling occurs to the input loads.

2.3.2 Level C Service Limits

On the basis of the stress analysis results, the controlling load case for buckling (largest compressive stress) for Level C will be inadvertent actuation of the spray system (external pressure of 2 psi and temperature of 110°F) with the SSE spectra (combination (iii)(c)(1) of SRP 3.8.2; see Table 2.4). As Level C has a larger factor of safety requirement, it will control over Level D. The minimum predicted buckling load was determined by introducing geometric imperfections in addition to the material nonlinearities in the analysis. The imperfection is modelled as a sinusoidal wave. The imperfection wave length, L_K is expressed in terms of the radius, R and thickness of the shell, t as

$$L_K = K^*(Rt)^{1/2} \qquad (2.1)$$

where K is the imperfection wavelength parameter [see Sec. 3.3 of Ref. 2.1]. The imperfection sensitivity analysis is performed by varying K. A radial imperfection amplitude of 0.875 in. was used which corresponds to the Code specified maximum deviation of one shell thickness (1.75 in.) [see Sec. A.3.4 of Ref. 2.1 and Footnote 7 of Ref. 2.7]. The BOSOR5 buckling analysis yielded a minimum buckling load multiplier of 2.35 for an imperfection wavelength of 137.5 in. ($3.0.\sqrt{rt}$).

The above analysis was performed with the meridional stress resultants in compression and the circumferential stress resultants in tension. (As explained in Sec. 4.1 of Ref. 2.1, both the meridian and circumferential stresses cannot be in compression at the same time. This would be incompatible with stresses in the lowest modes.) The process was repeated assuming the circumferential stress resultants to be in compression and the meridional stress resultants in tension, giving a minimum buckling load multiplier of 5.1.

The minimum buckling factor of safety is 2.35 for Level C Service Limit. For this load case, the variation of the effective uniaxial strain at the extreme fiber at the elevation of 96.8 ft. is shown in Figure 2.6. Note that, the effective strain is well above the proportional limit (Figure 2.4). Hence, the buckling of the containment is not elastic because geometry imperfection have been included.

2.3.3 Level A Service Limits

Two load combinations constitute the Level A service limit (see Table 2.2). The first is load combination (iii)(a)(3) of SRP 3.8.2, associated with inadvertent actuation of the spray system (external pressure of 2 psi and a temperature of 110°F). For this loading combination a minimum value of the load multiplier was determined to be 10.5.

The second load case, which is associated with a loss of coolant accident (internal pressure of 53 psi and a temperature of 290°F) also corresponds to load combination (iii)(a)(3) of SRP 3.8.2. Locally high compressive stresses arise in the transition region due to the restraint provided by the cork as the temperature is increased. The containment reached its yield capacity in the upper reaches remote from the base at a load multiplier of 2.85. At this point, no buckling was detected in the compression zone. Internal pressure increased the resistance of the containment to buckling by inducing tensile stresses which counteracted the thermal compressive stresses. A requisite characteristic for buckling is the presence of a compressive zone which extends about a buckled wave. However, the compressive stresses in the transition zone are extremely localized and the thermal effects rapidly reduce to zero [see Fig. 2.3 of Ref. 2.1]. Tensile stresses in the upper portion of the shell predominate and cause overall failure of the containment before buckling occurs. The variation of maximum effective uniaxial strain at the extreme fiber at Elevation 243 ft. is shown in Fig. 2.7.

It should be noted that the cork embedded portion of the containment is modelled with springs that carry both tension and compression [Section 2.1 of Ref. 2.1]. This is satisfactory for outward buckling. Inward buckling of the containment would be restricted by the interior concrete and not by the cork in tension, as the model now exhibits. This is a limitation of the analysis. A more complete analysis of thermal buckling in the transition zone may be appropriate but is beyond the scope of this task.

2.3.4 Discussion

The factors of safety against buckling prescribed in Section NE3222.1 of the ASME Code are listed in Table 1.1. The calculated factor of safety for Level C is 2.35. This does not satisfy the criteria. The calculated factor of safety for buckling under Level A is at least 10.5. However, the containment would reach its yield capacity under internal pressure at a calculated load multiplier of 2.85. The predicted factors of safety satisfy the Code Case N-284 criteria. Regulatory Guide 1.57 is satisfied.

2.4 Seismic Limit Analysis

There is a small probability that the containment could experience seismic loading beyond SSE. The containment performance was evaluated by increasing the seismic loading beyond SSE with constant sustained loads such as dead weight.

2.4.1 Loading and Solution Process

The loading and solution process for the buckling analysis of the containment is summarized in Section 4.1 of Ref. 2.1. The buckling factor, Γ, is defined as the ratio between the SSE loads and the seismic loads which cause buckling. The dead load is also applied and held constant. No other loads are applied. Hence, the net load on the structure, L is the sum of factored SSE loads (i.e., SSE loads multiplied by the factor, Γ) and the dead load D equivalent to:

$$L = D + \Gamma\,(SSE) \qquad (2.2)$$

2.4.2 Buckling Analysis Results

The containment is initially loaded with SSE loading and the dead weight of the structure. Geometric imperfections are introduced into the analysis and an imperfection sensitivity analysis is performed by varying the imperfection wavelength parameter, K [Sec. 2.3.2 and Sec. 3.3 of Ref. 2.1]. The imperfection is modelled as a sinusoidal wave with a radial imperfection amplitude of 0.875 in. which corresponds to the Code specified maximum deviation of one shell thickness (1.75 in.) [Sec. A.3.4 of Ref. 2.1 and Footnote 7 of Ref. 2.7]. The material effective stress strain curve in Fig. 2.4 is used. The seismic loading was increased by the factor Γ, until buckling occurs at a load multiplier of 2.91 with an imperfection wavelength of 137.5 in. The variation of the effective uniaxial strain at the extreme fiber at the elevation of 96.8 ft. is shown in Fig. 2.8.

2.4.3 Summary

Buckling occurred when the SSE loading was increased by a factor Γ of 2.91.

2.5 References

2.1 L. Greimann, et. al., "System 80+™ Containment - Structural Design Review," NUREG CR-5957, prepared for NRC, Washington, June, 1992.

2.2 Bushnell. D., "Plastic buckling of Various Shells," Joint ASCE/ASME Mechanics conference, June 21-29, 1981, Boulder, CO.

2.3 Bushnell. D. and Smith, S., "Stress and Buckling of Nonuniformly Heated Cylindrical and Conical Shells," AIAA Journal, 9 (12), pp. 2314-2321, Dec. 1971.

2.4 American Society of Mechanical Engineer, Boiler and Pressure Vessel Code Case N-284," Metal Containment Shell Buckling Design Methods," Supplement #2 to Nuclear Code Case Book, 1980.

2.5 U.S. NRC Standard Review Plan (SRP) Section 3.8.2, Rev. 1 - July 1981, pp. 3.8.2.9 - 3.8.2.11.

2.6 American Society of Mechanical Engineers, Boiler and Pressure Vessel Code, Section NE3220, 1989.

2.7 U.S. NRC regulatory guide 1.57, "Design Limits and Loading Combinations for Metal Primary Reactor Containment System Components".

3. THREE DIMENSIONAL MODEL PARAMETERS

3.1 Software Selection

The ANSYS [Ref. 3.1] and ABAQUS [Ref. 3.2] general purpose finite element programs were reviewed and compared. The comparison was based on types of shell elements in the element library, analysis procedures for buckling problems, pre- and post-processing capabilities and hardware and software limitations. Analytical results were compared to theoretical results from classical shell theory and numerical results from BOSOR.

3.1.1 Types of Shell Elements

Flat and curved shell elements are available in ANSYS and ABAQUS. A flat shell element is the assembly of a plane membrane element and a plate bending element. The accuracy of flat elements is more sensitive to surface curvature [Ref. 3.2, 3.3]. Curved shell elements are based on classical shell theory [Ref. 3.3]. Since those elements can take on a general second order polynomial shape, they are well suited to model doubly curved surfaces. Triangular and quadratic shell elements are available. Quadratic shell elements can be four noded, eight noded or nine noded with six degrees of freedom per node. ABAQUS also has shell elements that utilize the reduced integration procedure in the element formulation. In those elements, in-plane rotational stiffness is eliminated and solution time is reduced. They provide accuracy identical to shell elements using six degrees of freedom per node [Ref. 3.1, 3.2].

3.1.2 Analysis Procedure

Before proceeding to consideration of various shell buckling analysis techniques, a conceptual description of the instability behavior of shells is appropriate (see [Ref. 3.4]). Figure 3.1 schematically illustrates the possible load-displacement behavior of a shell, e.g. a spherical shell under external pressure. Loading may progress along a fundamental path of the perfect structure OCP. The deformed shape remains essentially the same along this path with only the magnitude of the displacements increasing. Eventually, an instability occurs along this path, point P, at a point of maximum load. This point is variously referred to as the limit point buckling, λ_p, or snap

through or the plastic collapse load. For this behavior, the deflected shape at maximum load differs from the initial deflected shape only in magnitude.

For many shell configurations and loadings, an alternative equilibrium path is available. That is, a bifurcation point C exists at which two equilibrium shapes are possible. At this point, the shell will follow the path of the least energy, path CD. This behavior is termed bifurcation buckling. The post buckling path is called a secondary path. Deformations along this path differ completely from the prebifurcation path, e.g., non-symmetric buckling of an axially compressed cylinder in which wrinkles or lobes form around the circumference. Elastic buckling occurs if the shell is elastic at the bifurcation point, λ_c, i.e., point C is below the proportional limit. If C is above the proportional limit, inelastic (or plastic) buckling occurs.

If the shell has an initial nonsymmetric imperfection, it will not reach the bifurcation point. It will deform in the pattern of the initial imperfection without noticeably changing shape until it reaches a limit load identified as λ_L. The equilibrium path is designated as the fundamental path of the imperfect structure. No bifurcation point occurs. After this limit load, λ_L, is reached, the loading path becomes asymptotic to the post buckling path (Fig. 3.1).

The purpose of shell buckling analysis is to predict the load displacement behavior, i.e. path OCP or OCD in Fig. (3.1) for perfect shells or path OLF for imperfect shells. Buckling analysis procedures which include both material and geometric nonlinearities were reviewed in the ANSYS and the ABAQUS programs. Nonlinear buckling analyses in both codes employs a nonlinear static analysis with gradually increasing loads to the point at which the structure loses its stability. In this analysis procedure, the structure is loaded step-by-step and at every load increment the equilibrium equations are solved iteratively up till convergence. Singularities may occur somewhere along the equilibrium path, namely the critical points λ_p, λ_c, and λ_L. Hence, the stability analysis requires a method capable of detecting critical points and tracing the equilibrium path beyond the critical points.

In ANSYS (Ver. 4.4A) the nonlinear static analysis is a load-controlled solution based on Newton-Raphson technique. The fundamental path can be determined up to the critical point, λ_c or λ_p which ever is lower. In ABAQUS, the modified Riks method [Ref. 3.5, 3.6] is utilized. In

this method a constraint equation is added to the equilibrium equations to fix the length of the incremental load step in the load-deflection space. The applied load level becomes an additional variable. The modified Newton-Raphson method is applied to solve the system of equilibrium equations iteratively. The stability determinate and eigenvalues are checked during solution to determine if a bifurcation load has been reached. The resulting technique allows the limit points to be passed, improves convergence, and detects location of critical points, λ_p, λ_c, and λ_L, along the fundamental path. (Section 3.2.2.1 utilizes an arch as an example to further explain this process.)

3.1.3 Preprocessor and Postprocessor

The preprocessor defines model geometric, material properties, loading configuration and kinematic conditions. ANSYS has a powerful preprocessor which can be easily used in a batch mode or an interactive mode. Solid modeling is also available in ANSYS. On the other hand, the ABAQUS preprocessor is limited to only batch mode usage. It has limited node and element generation capabilities compared to the ANSYS preprocessor.

The postprocessor illustrates output results after the solution, such as displacements, reaction forces, stresses and strains. Both ANSYS and ABAQUS have powerful postprocessors that can print and/or plot analysis results.

Based on the previous discussion, ABAQUS was selected for the 3-dimensional analysis of System 80+™ Containment, primarily because it implements the modified Riks methods and can predict the post buckling path.

3.2 Solution Processes in ABAQUS

In the following section, the verification of ABAQUS software for buckling problems will be presented.

3.2.1 Eigenvalue Buckling Prediction

Classical eigenvalue buckling analysis is often used to estimate the critical (bifurcation) load of elastic, linear structures that carry loads primarily by membrane action.

The eigenvalue problem can be described as [Ref. 3.2, 3.3].

$$[[K_b] + \lambda_c [K_Q]]\{\Phi\} = 0 \qquad (3.1)$$

$[K_b]$ = elastic stiffness matrix of the structure.
$[K_Q]$ = initial stress and load stiffness matrix.
λ_c = load multiplier (eigenvalue).
$\{\Phi\}$ = buckling mode shape (eigenvector).

Two eigenvalue buckling problems for linear elastic structures were solved with ABAQUS and compared to theoretical closed form solutions.

3.2.1.1 Circular Cylinder Subjected to Axial Load

The critical buckling stress of a long shallow cylinder without geometric or material imperfections is given by [Ref. 3.7, 3.8].

$$\sigma_c = \frac{E}{\sqrt{3(1-\nu^2)}}\left(\frac{t}{r}\right) \qquad (3.2)$$

σ_c = critical buckling stress.
E = Young's modulus.
t = shell thickness.
ν = Poisson's ratio.
r = radius of cylinder.

The associated buckling mode can be either a chess board buckling pattern or an axisymmetric sine wave. The buckling mode wave length is [Ref. 3.7, 3.8].

$$L_w = 3.44\sqrt{rt} \qquad (3.3)$$

The finite element model used in the buckling analysis is illustrated in Fig. 3.2. A segment that subtends 30° at the center was modeled using S4R5 shell elements. S4R5 shell elements are isoparametric flat shell elements, four noded with five degrees of freedom per node [Ref. 3.1].

The lower edge of the model was simply supported, symmetry conditions were applied at the other three edges. The model was loaded with uniform axial load applied at the upper edge.

The theoretical critical stress obtained from Eq. (3.2) was 175,562 psi compared to a critical stress of 175,515 psi obtained from ABAQUS finite element model. The percentage difference was 0.03%. The buckled mode corresponding to the least eigen value is illustrated in Fig. 3.2. The buckled shape is axisymmetric with wave length 2.67 in. which compares to a value of 2.75 in. computed from Eq. (3.3).

3.2.1.2 Spherical Shell Subjected to Uniform External Pressure

The critical external buckling pressure of a complete sphere using the equilibrium method is [Ref. 3.7, 3.8]:

$$p_c = \frac{2Et}{r}\left[(m^2+n^2)^{-1} + \frac{(t/r)^2(m^2+n^2)}{12(1-\nu^2)}\right] \qquad (3.4)$$

m = no. of sine waves in hoop direction.
n = no. of sine waves in meridional direction.

The smallest p_c corresponds to the following condition:

$$m^2 + n^2 = 2\sqrt{3(1-\nu^2)}\, r/t \qquad (3.5)$$

For m equal to n, the buckled wave length is:

$$L_w = \frac{2\pi r}{m} = \frac{2\pi\sqrt{rt}}{(3(1-\nu^2))^{1/4}}$$

or, for ν equal 0.3

$$L_w = 4.89\sqrt{rt} \tag{3.6}$$

The finite element model used in the analysis is illustrated in Fig. (3.3). Only one-eighth of the sphere was modeled due to symmetry. The sphere was modeled using S8R5 which is an isoparametric curved shell elemen having eight nodes with five degrees of freedom per node. All nodes in the model are located along the principal spherical coordinate lines [Ref. 3.9]. That is, the nodal coordinates were computed as the intersection of the sphere and two planes passing through the global cartesian axis. Symmetry boundary conditions were applied along the three edges. The sphere was loaded with uniform external pressure.

The theoretical critical pressure computed from Eq. (3.4) and (3.5) was 74.78 psi compared to a critical pressure of 75.16 psi obtained from ABAQUS finite element model. The percentage difference was 0.5%. The buckled mode corresponding to the least eigenvalue is depicted in Fig. (3.3) with waves in both the meridional and hoop direction. The wave length was 180 in. compared to a value of 224 in. computed from Eq. (3.6).

The previous two examples verifies the eigenvalue procedure in ABAQUS software for linear elastic buckling of shells.

3.2.2 Nonlinear Buckling Analysis

As noted in Sec. 3.1.2, nonlinear buckling can be accomplished using a nonlinear static analysis in which equilibrium equations are solved in a point wise fashion to the load where the structure loses its stability.

Two problems were solved using ABAQUS to examine the capability of the code to trace the fundamental path and the post buckling path (see Fig. 3.1), to determine the critical points λ_c and λ_{cl}, and to obtain the buckled shape when geometric and material nonlinearities are included in the analysis. Results were verified by comparing to BOSOR results and to solutions in referenced literature.

3.2.2.1 Hinged Arch with External Pressures

The stability of a circular arch, uniformly loaded in the radial direction is lost at either a limit point, λ_L, or a bifurcation point, λ_c, depending on the arch dimensions and supporting condition. This property offers the opportunity to test nonlinear buckling numerical techniques adopted in ABAQUS.

The arch was modeled using three noded curved beam elements B32 [Ref. 3.2]. The results of the computations carried out will be briefly discussed. Four cases were solved to examine the ability to predict the fundamental path, post buckling path, critical points and prebifurcation deformed shape.

In all four cases the load-deflection curve was plotted using the nondimensional load parameter, ρ, [Ref. 3.5] and the nondimensional deflection parameter [Ref. 3.6], w

where:

$$\rho = \frac{pr^2 h}{EI} \tag{3.7}$$

$$w = w_o / h \tag{3.8}$$

in which

p = external pressure.

h = arch thickness.

E = Young's modulus.

r = radius of arch.

I = cross section moment of inertia about bending axis.

w_o = central deflection of the arch.

First, the fundamental path (Fig. 3.4) of the perfect arch was computed using the modified Riks methods. The solution was continued beyond the bifurcation point and the limit point. The

position of the critical points along the fundamental path was determined, as ABAQUS prompts the user that a negative eigenvalue has been encountered, that is, a bifurcation point has been reached. The load parameter, ρ_c, at the bifurcation point was 2.20 and that at the limit point, ρ_L, was 2.94. The solution continues on the fundamental path, hence the deformed shape remained symmetric and only the magnitude of the deflections increased.

At the bifurcation point, ρ_c, two equilibrium shapes are possible. One possible shape is the symmetric deformed shape of the perfect structure which corresponds to the fundamental path. It was computed in the previous step. The other shape can be computed by examining the stability condition near the bifurcation point. The nonlinear static analysis was restarted at a load parameter, ρ, equals to 1.80 preceding ρ_c. At this point, an eigenvalue solution (Eq. 3.1) with the present pre-buckling conditions was carried out. The bifurcation point (first eigenvalue) was computed as ρ_c equals to 2.15 and the first eigenmode (unsymmetric) was obtained (Fig. 3.4). The value of ρ_c obtained by this method compares with the value of 2.20 computed using the modified Riks technique alone.

The post buckling path was computed in the third step. An initial geometric imperfection of a small amplitude in conjunction with the two different imperfection shapes discussed below was applied to introduce nonsymmetries and force the arch to follow the fundamental path of the imperfect structure and approach the post buckling path rather than the fundamental path of the perfect structure. Note that, for this solution there is no bifurcation point, since the initial and final shape of the structure remains essentially the same, except for displacement magnitude. The solution follows a fundamental path for the imperfect structure and the maximum load is the limit load for the imperfect structure (see Sec. 3.1.2). With a very small imperfection amplitude, the limit load, ρ_L, for this solution is very close to the bifurcation load for the first analysis. Likewise, the path for this solution is the desired post buckling path.

Two imperfection shapes were selected. First, an imperfection shape similar to the first eigen mode (Fig. 3.4) was applied. The amplitude, a, of the imperfection was varied to examine its effect on the limit load. With a equals to 0.005 h, the limit load, ρ_L, was 2.08 which, indeed, is close to the bifurcation load, ρ_c, of 2.15 obtained by solving the eigenvalue problem. As the solution goes beyond the limit load, it continues to follow the fundamental path of the imperfect

respectively. This analysis revealed that the limit load is approximately inversely proportional to imperfection amplitude [Ref. 3.8]. Second, a single bulge imperfection centered at 10 degrees and with amplitude 0.025h was applied as shown in Fig. (3.4). The limit load was 2.08 as compared to 1.97 for the eigenmode imperfection with identical amplitude. Hence the eigenmode imperfection shape provided the least limit load for the same amplitude. This is consistent with Koiter theory [Ref. 3.8].

Another approach to computing the post buckling path is to apply a dummy load of a low magnitude that will introduce nonsymmetries into the problem. No geometric imperfections are applied. A dummy small horizontal load was applied and the problem was solved using the modified Riks method. The load-deflection curve is illustrated in Fig. 3.4. The limit load, ρ_L, was 2.09. The post buckling path of the perfect arch closely followed that obtained using an eigenmode imperfection amplitude equals to 0.005 h.

3.2.2.2 Imperfect Sphere with External Pressures

The stability of a spherical shell uniformly loaded with external pressure was investigated. The ABAQUS solution was verified with BOSOR5 results.

The complete sphere has a radius of 1200 in. and a wall thickness of 1.75 in. (same dimensions as System 80+™ containment). A modulus of elasticity of 29,000 ksi was used for the material. The material was assumed to be linearly elastic. An axisymmetric imperfection for the sphere was modeled as a sinusoidal wave, the imperfection peak to trough amplitude was 3.50 in. and the imperfection wave length was $3.92\sqrt{rt}$. The imperfection amplitude applied in this example is twice the allowable ASME value of 1.75 in.

The three dimensional model is the same as illustrated in Fig. 3.3. The equilibrium fundamental path from the ABAQUS solution is depicted in Fig. 3.5. The bifurcation load was computed as 12.76 psi compared to 12.15 psi obtained from BOSOR which is a 5% difference.

3.3. Three Dimensional Model of System 80+™

The finite element method offers an approximation to the exact solution. The difference between the exact solution and the approximate solution arises from the discritization of the continuous structure into subdivisions, (elements), implementation of shape functions to describe deformations and stresses within an element, and the computation of the stiffness matrix by numerical integration. The solution accuracy can be improved by decreasing the size of subdivisions, this is designated as h-refinement, and by increasing the order of the polynomial used to describe the behavior of each element which is known as p-refinement [Ref. 3.10].

3.3.1 Mesh Generation Procedure

A finite element model was constructed for a spherical shell similar to System 80+™ containment (Fig. 1.1) except without penetrations. Mesh sensitivity studies with h-refinement and p-refinement were conducted. Four mesh configurations A, B, C, and D were studied (Figs. 3.6 to 3.9, respectively). The size of the elements was progressively doubled from Mesh A to Mesh D. Mesh C is identical to Mesh B except in the embedded portion, where the size of the elements was halved in the meridional direction. Two elements were used for every mesh configuration, the S4R5 flat shell element which is four noded [Ref. 3.2] and the S8R5 curved shell element with midsize nodes and four corner nodes which uses a higher order polynomial. S4R5 and S8R5 shell elements have five degrees of freedom per node [Ref. 3.2]. These two elements were previously tested in buckling problems (Sec. 3.2.1.1 and 3.2.1.2).

One quarter of the spherical shell was modeled due to symmetry. Symmetry boundary conditions were applied at the two vertical edges whereas fixed boundary conditions were applied at the base. Table (3.1) summarizes the parameters of the four mesh configurations. The four meshes were compared with regard to the total number of elements, the size of the elements at the equator and at the base, and the element aspect ratio at the base.

Other mesh parameters such as total number of variables, wave front, root mean square (RMS) of wavefront, storage space per analysis and storage space per load increment, are presented in Table (3.1) for the four mesh configurations. From Table (3.1) we can conclude that the use of

midside nodes in the finite element model doubles the wave front whereas the number of variables increase four times and the storage space requirement increases eight times.

Two loading conditions were solved, external pressure and gravity loads. The pressure loading produces a uniform biaxial stress state whereas the stresses for gravity loading results in a vertical gradient of the stresses. The ABAQUS results obtained using the four meshes were compared to BOSOR results.

3.3.1.1 Sphere with External Pressure

The nonlinear buckling analysis of the spherical shell when subjected to external pressure was conducted using the four mesh configurations A, B, C and D. The containment vessel was assumed to have an axisymmetric sine wave imperfection of amplitude 0.875 in. and wave length of $3.92\sqrt{rt}$. The effective stress-strain curve used in the analysis is illustrated in Fig. 2.5. The shell was analyzed using BOSOR5 to compare to ABAQUS results. The axisymmetric model of the shell is similar to that described in Sec. 2.1 of [Ref. 3.4], except all shell segments had the same density. The critical pressure was 22.5 psi from BOSOR5. Figure 3.10 illustrates the buckled shape obtained from the BOSOR5 solution. The number of waves in the hoop direction associated with the minimum buckling pressure was 25 waves.

ABAQUS results obtained using the four mesh configurations (Sec. 3.3.1.1) are compared in Table 3.2 which lists the critical pressure from ABAQUS, the percentage difference with respect to the BOSOR solution and the run time per iteration. The run time per iteration is computed by dividing the CPU time per load step by the total number of iterations in that step. Figure 3.11 illustrates the buckled shape of Mesh C obtained using ABAQUS. The number of waves around the circumference was 28 waves.

Table 3.2 shows that, for S8R5 curved shell elements, the percentage error in the buckling load was significantly reduced when the size of the elements was halved from Mesh D to Mesh B. The run-time per iteration was increased as the number of variables in the model and the wave front were almost doubled. However, when Mesh B was refined to Mesh A, the reduction in the percentage of error was not significant whereas the run time per iteration increased five times.

Results obtained from Mesh C using S8R5 elements were better than those obtained from Mesh A using S4R5 flat shell element. This indicates that p-refinement was more efficient than h-refinement in improving the solution accuracy although the run time per iteration was increased slightly.

3.3.1.2 Sphere with Gravity Loads

The nonlinear buckling analysis of the spherical shell described above when subjected to gravity loads was conducted using the four mesh configurations A, B, C and D. This case has a gradient stress resultant in the vertical direction. The shell has the same imperfection configuration and constitutive relation described in Sec. 3.3.1.1.

The axisymmetric model in Sec. 3.3.1.1 was used in the BOSOR5 solution, which gave a load multiplier at the limit point of 14.0. The deformed shape of the BOSOR5 axisymmetric model is illustrated in Fig. 3.12. The deformed shape remained axisymmetric with no waves in the hoop direction.

ABAQUS and BOSOR5 results were compared in Table 3.3. Figure 3.13 illustrates the deformed shape of Mesh C obtained using ABAQUS. The deformed shape was also axisymmetric.

Table 3.3 shows that, for S8R5 shell element, the percentage error in the limit load was reduced when the size of the elements was halved from Mesh D to Mesh B. The most accurate solution was obtained by using Mesh C, since a finer mesh was utilized at the base of the shell to capture the steep stress gradients. There was no need to solve the problem using Mesh A, as the results obtained from Mesh C were sufficiently accurate.

Results obtained from Mesh C with S8R5 element were almost identical to Mesh A result with S4R5 element, however, the run time required per iteration was slightly greater for the latter. This reveals that using Mesh C with S8R5 element is more economic than using Mesh A with S4R5 element and provides acceptable accuracy.

Based on the two previous examples, Mesh C with S8R5 was considered sufficiently accurate with reasonable run time and storage requirements and was used as the basis for the containment analysis.

3.3.1.3 Sphere with Reinforced Opening at the Top

A three dimensional finite element model was generated for a spherical shell with a reinforced opening at the top. Figure 3.14 illustrates a sectional elevation of the shell. This is an axisymmetric problem and can be analyzed with BOSOR5. A similar finite element model will be used for the equipment hatch portion of the System 80+™ containment model. The opening has the same dimensions and reinforcing details as the equipment hatch. The hatch barrel is a circular cylinder of inner radius 132 in., wall thickness 3.75 in. and length 30.4 in. The three dimensional model is a sector of a sphere that subtends an angle 60° at the center. The sphere sector was assumed to have a sine wave axisymmetric imperfection of amplitude 0.875 in. and wave length of $3.0\sqrt{rt}$. The imperfection sine wave was started from the axis of the barrel.

The three dimensional model of the shell is depicted in Fig. 3.15. Only one-quarter of the shell was modeled due to symmetry. S8R5 curved shell elements were used in the model. The element and node configuration along the edges are compatible with the Mesh C configuration at the equator. Four rows of elements were used in the reinforced collar region. The elements size was limited to $0.4\sqrt{rt}$ in the meridional direction with an aspect ratio that varies from 1.3 at the hatch barrel to 2.8 at the thickness transition zone (see Fig. 3.14). One row of elements was used in the transition zone from the thick shell to the thin shell. The elements size is $0.12\sqrt{rt}$ in the meridional direction and $1.19\sqrt{rt}$ in the hoop direction. The rest of the spherical sector was divided into seven rows of elements in the meridional direction as shown in Fig. 3.15. The hatch barrel was modeled with six rows of elements in the hoop direction and three rows of elements in the axial direction. Symmetry boundary conditions were applied at the two vertical edges whereas fixed boundary conditions were applied at the lower edge. The model was loaded with an axisymmetric ring load applied on the upper edge of the hatch barrel. The material constitutive relation is shown in Fig. 2.5.

A nonlinear inelastic buckling analysis was conducted using the modified Riks methods implemented in ABAQUS and the results were compared to the BOSOR solution. The ring load was applied in increments and the vertical displacement of the hatch barrel was recorded for every converged solution. The solution was terminated as the limit load was reached. The load deflection curve (fundamental path) obtained from using ABAQUS and BOSOR are compared in Fig. 3.16. The collapse load obtained from ABAQUS was 5000 lb./in. compared to a value of 4852 lb./in. obtained from BOSOR (3.5% difference). The failure mode was excessive plastification of the transition zone. The deformed shape obtained from the ABAQUS solution is illustrated in Fig. 3.16. Since the finite element model in Fig. 3.17 showed reliable results, it will be used to model all penetrations in the System 80+™, i.e., the containment equipment hatch, the upper and lower personnel air locks.

3.3.1.4 Assembly of the Three Dimensional Model

Figure 3.17 illustrates the three dimensional finite element model of System 80+™ containment with all penetrations. The model was constructed basically using the Mesh C except that elements near all penetrations were replaced by the mesh configuration for the sphere with the reinforced opening at the top (Sec. 3.3.1.3). The equipment hatch barrel was modeled as a circular cylinder with inner radius of 11 ft. and wall thickness of 3.75 in. The length of the barrel in the model was 40.4 in with the outer edge of the barrel extended a distance of 22.0 in. (equivalent to $\sqrt{rt}$) from the shell wall. Not all of the barrel length was modeled as it does not contribute to the stiffness but it does contribute to the mass of the equipment hatch. The density of the barrel material was computed such that its total weight is 120,000 lb. (see Sec. 1.3).

The upper air lock barrel was modeled as a circular cylinder with inner diameter of 10 ft., wall thickness of 2.5 in. and length of 11.5 ft. The outer edge of the barrel is located at a distance of 8.1 ft. from the centroid of the containment vessel wall and is simply supported in the vertical direction (see Sec. 1.3). The length of the lower air lock barrel is 10.2 ft. with the outer edge located at 5.1 ft. from the centroid of the vessel wall. Note that for both air locks, the barrel length for the finite element model extended at least $\sqrt{rt}$ from the containment shell. The density of both barrels materials was computed so that they weigh 50,000 lb. each (see Sec. 1.3).

The mass of the spray header system was smeared from the top down to Elev. 247' - 7". Between Elev. 139' - 7" and 93' - 0", the containment is provided with several small penetrations that contribute 80,000 lb. to the weight of the containment. The mass of these appurtenances was smeared around the circumference between these elevations. The thickness of the shell at the embedded portion in concrete was taken as 1.75 in. rather than 2.0 in. (see Sec. 1.3) to account for corrosion. However, this additional thickness was not included in the analysis presented in this work.

3.4 Check Run

To verify the three dimensional model of System 80+™ containment described in Sec. 3.3.1.5 prior to the nonlinear buckling analysis, the model was loaded with uniform external pressure of 10 psi. A modulus of elasticity of 29,000 ksi was used for the material. The analysis was conducted using the small deflection theory and no imperfections were modeled. The meridional and hoop stress resultants obtained from the ABAQUS solution compared well to the classical theoretical value of 6000 lb./in. The contour lines for meridional and hoop stress resultants were examined and they were uniform over the containment except that high stress concentration regions were observed around the penetrations. The stress concentration factor in the vicinity of the equipment hatch barrel compared well to the theoretical value of four for a biaxial stress state. Contour lines of the nondirectional Von Mises stresses were examined at the three penetrations and found to be approximately axisymmetric.

3.5 Imperfection Size and Shape

An axisymmetric imperfection was incorporated into the three dimensional finite element model of System 80+™. The imperfection was modeled as a sinusoidal wave with radial amplitude of 0.875 in. and wave length of $3.0\sqrt{rt}$. The amplitude of imperfection corresponds to the Code specified maximum deviation of one shell thickness. The imperfection wave length was based on the imperfection sensitivity analysis described in Sec. 2.3.2.

3.6 Material Properties

The stress strain curve of the material used in the three dimensional finite element model is illustrated in Fig. 2.5.

The containment portion embedded in concrete has a cork type material along the outerside between Elev. 90' - 3" and 91' - 9" whereas the inner side is in direct contact with concrete in Fig. 1.4. The cork material thickness was assumed to be 2.0 in. with a subgrade modulus of 180 lb/in^3. The cork material was modeled using the SPRING1 element in ABAQUS [Ref. 3.2]. The springs were located outside the containment in the radial direction. The load deflection curve used to define the springs behavior is illustrated in Fig. 3.18. The springs were provided an arbitrarily high stiffness of 1800 lb./in^3 in tension side to model the containment contact with concrete along the inner surface. However, on the compression side, the stiffness of the springs is 180 lb/in^3 up to an axial displacement of 1.0 in. The stiffness then increases gradually as displacements increase. At a 2.0 in. displacement, the cork material is fully compressed and the stiffness of the springs becomes very large as depicted in Fig. 3.18.

3.7 References

3.1. Desalvo, G. J. and Gorman, R. W., "ANSYS User's Manual," Swanson Analysis Systems, 1989, Houston, PA.

3.2. Hibbitt, Karlson and Sorensen, Inc., "ABAQUS User's Manual," 1994.

3.3. Cook, R. D., Malkus, D. S. and Plesha, M. E., "Concepts and Applications of Finite Element Analysis," John Wiley and Sons, 3rd Edition, 1989.

3.4. NUREG CR-5957, L. Greimann, et al., "System 80+™ Containment Structural Design Review", prepared for NRC, Washington, May, 1993.

3.5. Riks, E., "An Incremental Approach to the Solution of Snapping and Buckling Problems," Journal of Solids and Structures, Vol. 15, pp. 529-551, 1978.

3.6. Crisfield, M. A., "A Fast Incremental/Iterative Solution Procedure that Handles "Snap Through," Computers and Structures, Vol. 13, pp. 55-62, 1980.

3.7. Kollar, L. and Dulacska, E., "Buckling of Shells for Engineers," John Wiley and Sons, 1984.

3.8. Timoshenko, S. P. and Gere, J. M., "Theory of Elastic Stability," McGraw Hill, 1982.

3.9. Hughes, T. J. R. and Hinton, E., "Finite Element Methods for Plate and Shell Structures," Vol. 1: Element Technology, Pineridge Press International, Swansea, U.K., 1986.

3.10. Zienkiewicz, O. C., "The Finite Element Method in Engineering Science," McGraw Hill, London, 1971.

4. THREE DIMENSIONAL ANALYSIS OF SYSTEM 80+™ CONTAINMENT

4.1 Approach

In this chapter the buckling analysis results for System 80+™ containment is presented. The objective is to compute the buckling factor of safety for Service Level C (Sec. 2.3.2) including local buckling due to concentrated loads at penetrations. The loading configuration consists of an external pressure of 2 psi, temperature of 110°F, SSE ground excitation, and gravity loads.

The containment is subjected to seismic loading that implies time varying stresses. Hence, the containment may exhibit such instability phenomena as parametric instability excitation or dynamic buckling in which the inertial forces from the seismic loading interact with the inertial forces associated with buckling motions . To obtain the buckling factor of safety an elaborate time history analyses which incorporates geometric and material nonlinearities should be performed. The structural response would be monitored as the load level is increased until excessive deformations occur. However, due to the lack of information such as the ground acceleration history, the time integration scheme will be replaced by a quasi-static buckling analysis. Buckling inertial forces will be neglected, as recommended in Section 1330 of Ref. 4.8. A set of equivalent static loads were obtained to regenerate the maximum SRSS stress resultants by two different approaches. In the first approach, the equivalent static loads were computed as inertia forces equal to the product of the lumped mass at the node and the maximum SRSS acceleration components. The equivalent static loads were added to the pressure, temperature and gravity loads to examine buckling along the equipment hatch meridian. In the second approach, the maximum SRSS stress resultants in a critical buckling region were decomposed into a linear combination of the modal stress resultants by the least squares method.

4.2 Response Spectrum Analysis

The response spectrum analysis procedure is generally applicable to the dynamic analysis of a complex structure with essentially linear response.

4.2.1 Modes of Vibration

For the vibration analysis, the global coordinate system was rotated about the Z-axis 210° counter clockwise to the prime coordinate system X', Y' and Z' directions (see Fig. 4.1) so that the local X' axis extends along the equipment hatch center line. The modal natural frequencies, participation factors and modes of vibration were extracted for the System 80+ containment in this transformed local coordinate system using the subspace iteration scheme [Ref. 4.4]. Note that the axis transformation was accomplished before the mode frequency analysis so that the maximum SRSS nodal accelerations will be computed in the local coordinate system, X', Y', Z' rather than the global coordinate system (the maximum SRSS nodal accelerations cannot be resolved from one coordinate system to another). The first twenty modes of vibration were extracted. Figures 4.2 to 4.11 illustrate the first ten modes of vibration. Results obtained from the modal frequency analysis are tabulated in Table 4.1, where the natural frequency (cycle/sec) and the participation factors in the X, Y and Z directions Γ_{ix}, Γ_{iy} and Γ_{iz}, respectively, for i equals one to twenty modes are shown. The fundamental mode is a cantilever mode in the X' direction (Fig. 4.2) whereas the second vibration mode is a cantilever mode in the Y' direction (Fig. 4.3). The third mode is basically vibration in the vertical Z' direction in addition to local vibration of the equipment hatch (Fig. 4.4) with the maximum displacement taking place in the transition zone between the reinforcing collar and the thinner plate. Modes 4, 5, 9, 10, 13 and 14 also represent local vibration of the equipment hatch as shown in the figures. Modes number 6, 7, 8, 9 and 14 are local vibrations of the upper personnel air lock. Modes number 6, 11, 12 and 14 are local vibrations of the lower personnel air lock. Modes 15 through 20 are local vibration modes of the spray header on top of the containment. Note that all local vibration modes have a frequency that corresponds to a significant value of spectral acceleration in the three spectra of the SSE earthquake (Fig. 2.1). These modes cannot be obtained from an axisymmetric analysis of the containment. The dominant modes in the containment response will be those that possess a significant spectral acceleration and significant participation factors.

4.2.2 Modal and Directional Combination

The modal response for each mode of vibration was computed for the three directions of the earthquake motion. The maximum response of the i mode (i = 1 to 20), say a stress resultant N_{ij}, due to the j (j = X, Y, Z) earthquake motion, can be determined as follows:

$$N_{ij} = N_i^{\phi} \Gamma_{ij} S_{ij} / \omega_i^2 \qquad (4.1)$$

where,

N_{ij} = Maximum stress resultant for mode i due to earthquake component in direction j

ω_i = Modal frequency for mode i

N_i^{ϕ} = Stress resultant corresponding to eigen mode i (Fig. 4.2 to 411)

Γ_{ij} = Participation factor of mode i in the j direction (Table 4.1)

S_{ij} = Spectral acceleration for mode i for earthquake component in direction j (Fig. 2.2)

One approach to estimate the maximum response is to combine modal responses utilizing the ten percent method to account for closely spaced modes [Ref. 4.5].

$$N_{max\,j} = \left\{ \sum N_{ij}^2 + 2 \sum \sum \left| N_{ij} N_{kj} \right| \right\}^{1/2} \qquad (4.2)$$

Modes of vibration are considered closely spaced if their frequencies differ by less than 10 percent. The maximum response of the structure N_{max} can be obtained by combining the response due to three earthquake directions by the square root of the sum of the squares [Ref. 4.1].

$$N_{max} = \left\{ \sum N_{max\,j}^2 \right\}^{1/2} \qquad (4.3)$$

4.2.3 Discussion of Results

Contours of the maximum SRSS membrane stress (Eq. 4.3) in the meridional direction $N_{1\,max}$ are shown in Figs. 4.12 and 4.13 and in the hoop direction $N_{2\,max}$ in Figs. 4.14 and 4.15. The contour plots show that high stress concentration regions were generated at all penetrations, in particular,

in the reinforcing collar region at the hatch barrel. Hence, the three penetration regions were recognized as potential buckling regions. These three are listed in Table 4.2 along with the peak values of $N_{1\ max}$ and $N_{2\ max}$. High stress regions were also recognized in the region near the concrete foundation (Table 4.2) where the peak meridional and hoop stress resultants took place at a circumferential angle θ of 260.63° (Fig. 1.1). High stress gradients at the reinforcing collar of the lower personnel air lock are near the base so that a possible buckling interaction might occur here (Table 4.2). For future reference, Table 4.2 also shows the maximum stress resultants at the base below the equipment hatch. Load cases are identified in Table 4.2 for future reference.

4.2.4. Maximum SRSS Stress Resultants at Support

Figure 4.16 illustrates that the value of $N_{1\ max}$ varied around the circumference at the base from a minimum value of 11300 lb/in at a circumferential angle θ of 121.88° to a maximum value of 15940 lb/in at θ equals to 260.63° (Table 4.2). The distribution of $N_{1\ max}$ approximates two sinewaves with the peak values at 76.88°, 166.88°, 260.63°and 350.63° rather than a uniform axisymmetric distribution of $N_{1\ max}$ obtained from the BOSOR model [Ref. 4.3]. As explained in Appendix A, this is a consequence of the ten percent rule and the two lowest modes, which are closely spaced. This phenomena of modal coupling at the support was not detected using the axisymmetric analysis with BOSOR because the two lowest modes aligned with the two horizontal excitations (see Appendix A). The peak $N_{1\ max}$ at the support obtained from the axisymmetric analysis was less than that obtained from the three dimensional analysis by 23% which will have a significant effect on the buckling factor of safety. The SRSS 10% method is considered to be conservative [Ref. 4.7]. The SRSS method without modal coupling gives an approximately uniform value of $N_{1\ max}$ of 11300 lb./in.

4.3 Equivalent Static Loads

4.3.1 Purpose

The maximum SRSS stress resultants obtained from the response spectrum analysis N_{max} (Fig. 4.12 to 4.15) cannot be directly input into the ABAQUS code to check buckling. As an alternative, they will be regenerated by applying a set of equivalent static loads on the containment. Each loading set is computed so that it generates a stress field that bounds the

maximum SRSS stress resultants at one critical buckling region (Table 4.2). At the same time, stress fields generated in other regions must not exceed the maximum SRSS stress resultants.

4.3.2 Approach #1

4.3.2.1 Methodology

In the first approach, the equivalent static loads were computed as inertia loads based on the maximum SRSS nodal accelerations. Chronologically, Load Case 6, buckling at the base in the equipment hatch meridian, (Table 4.2) was studied first. Every node in the model has three components of maximum accelerations $a_{max\ x'}$, $a_{max\ y'}$ and $a_{max\ z'}$, computed in the X', Y' and Z' directions, respectively, similar to Eq. 4.2. Figure 4.17 shows the variation of the maximum accelerations $a_{max\ x'}$ along a meridian passing through the equipment hatch central line. The figure indicates that $a_{max\ x'}$ reaches 3.17 g at the top, where g is the acceleration of gravity, with a peak value of about 7 g near the equipment hatch penetration. This is attributed to the large vibrations at this location in modes 1, 2, 3, 4, 5, 9, 10, 13 and 14. Figure 4.18, which shows the variation around the equator, illustrates that $a_{max\ x'}$ is nearly constant with an average value of about 1.5 g, and a peak of 7.6 g near the equipment hatch.

The nodal mass, m, was computed according to its contributory area. The equivalent static loads per node, $F_{x'}$, $F_{y'}$, and $F_{z'}$ were computed as

$$\begin{aligned} F_{x'} &= m\ a_{max\ x'} \\ F_{y'} &= m\ a_{max\ y'} \\ F_{z'} &= m\ a_{max\ z'} \end{aligned} \qquad (4.4)$$

The forces were applied by the 100/40/40 method [Ref. 4.1 and 4.2], i.e. 100% of $F_{x'}$ and 40% of $F_{y'}$ and $F_{z'}$. $F_{x'}$ was applied in the positive X' direction, $F_{y'}$ was in the negative Y' direction and $F_{z'}$ was in the negative Z' direction (i.e. vertically downwards) (see Fig. 4.1). The intention of this loading was to produce the maximum stress resultants near the base on the equipment hatch meridian (Load Case 6 in Table 4.2).

4.3.2.2 Discussion of SSE Stress Resultants

A preliminary static analysis of the shell was accomplished assuming elastic material behavior and small deflections to compare the stress resultants from the above loading to the SRSS stress resultants on the equipment hatch meridian. Contour plots of meridional stress resultants, N_1, are shown in Figs. 4.19 and 4.20, whereas Figs. 4.21 and 4.22 show the contours of the hoop stress resultants, N_2.

4.3.2.2.1 Stress Resultants at Containment Base

For SSE loading (Eq. 4.4), the containment exhibited a cantilever action where the extreme stress resultants N_1 took place at support. The value of N_1 was calculated to be -10645 lb/in. at the support below the equipment hatch, which was less than the corresponding value of N_{1max} (Table 4.2) by 12%. The maximum hoop stresses N_2 along the equipment hatch meridian was 16130 lb/in. at an elevation of 90.62 ft. which was less than the corresponding value of N_{2max} (Table 4.2) by 23%. Hence the stress field obtained from Approach #1 had a different shape than that produced by the response spectrum analysis and it did not bound the maximum stress resultants at the support.

4.3.2.2.2 Stress Resultants near Equipment Hatch

The inertial forces in Eq. 4.4 cause tensile stresses in the vicinity of the equipment hatch, which can be explained as follows. Consider a portion of a spherical shell with a reinforced opening from the side similar to the equipment hatch penetration (Fig. 4.23) subjected to an axisymmetric ring load with value of P, that corresponds to the inertia loads of the equipment hatch. The ring load, P, per unit length was computed using

$$P = m_h \, a_{max\,x'} / 2 \, \pi \, r_b \qquad (4.5)$$

where,

m_h = Total mass of the equipment hatch, 120,000/g lb. sec^2/in.

$a_{max\,x'}$ = Average acceleration of the barrel in the X' direction, 6.75 g (Fig. 4.22)

r_b = Radius of the equipment hatch barrel, 11 ft.

The meridional stress resultants, N_l, are computed using the classical membrane theory of shells [Ref. 4.6].

$$N_l = P r_b / r \sin\phi \qquad (4.6)$$

where,

r = Radius at which N_l is computed

ϕ = Angle subtended at the center

The stress resultants due to P are tensile and plotted in Fig. 4.24.

The meridional stress resultants for a sphere without a penetration were obtained by reversing the sign of the stress resultants at the 30° meridian in Fig. 4.20. They are also plotted in Fig. 4.24. When these two stress resultants are superimposed, as in Fig. 4.24, net tensile stresses are obtained near the penetration. This is similar to the results obtained from the three dimensional model (see Fig. 4.19). Hence, the locally high inertial forces cause locally high tensile stress resultants.

The contour plots of the meridional and hoop stress resultants, Fig. 4.19, 4.20, 4.21 and 4.22, show that high stress concentration regions were developed at all penetrations because of inertia loads (see Fig. 4.17 and 4.18). For the loading discussed here, the meridional stress resultants N_l were all tensile at the equipment hatch penetration (see Sec. 4.3.2.2.3) with an average stress concentration factor of about 4.5. The maximum tensile N_l of 8220 lb/in. took place at the reinforcing collar beside the hatch barrel and is considerably less than the corresponding value of $N_{l\max}$ (Table 4.2).

Utilizing Approach #1, buckling in the vicinity of the equipment hatch could have been examined by applying F_x in the negative X' direction. For the above paragraphs, this would not bound the maximum stress resultants values. By examining Fig. 4.24, one can see that the maximum stress resultants would be obtained by applying all F_x in the positive X' direction except those associated with the equipment hatch barrel (P force) which would be applied in the negative X' direction. In other words, the maximum stress resultants are not obtained by applying all inertial forces in the same direction. Hence, Approach #1 is not satisfactory.

4.3.2.3 Nonlinear Buckling Analysis

Even though it is not satisfactory, the containment was loaded with the equivalent static loads by Approach #1 (Sec. 4.3.2.1) together with an external pressure of 2 psi, rise in temperature of 40° F and gravity loads. The nonlinear buckling analysis was conducted using the modified Riks method [Ref. 4.4] where all the loads are applied proportionally in increments and the nonlinear system of equilibrium equations were solved iteratively up to convergence. The fundamental path (see arch discussion in Sec. 3.2.2.1) obtained from the nonlinear analysis is illustrated in Figs. 4.25 and 4.26. In Fig. 4.25 the load proportionality factor, λ, was plotted versus the lateral deflection in the X' direction at the top of the containment whereas λ was plotted versus radial displacements at the base (θ equals to 183.75°) in Fig. 4.26.

The load factor at which the containment lost its stability, λ_c, was 2.404 when excessive displacements took place at the base (see Fig. 4.26) and the nonlinear analysis indicated the first negative eigenvalue of the structure stiffness matrix. Buckling took place at the support at θ equals to 183.75° as shown in Fig. 4.27.

4.3.3 Approach #2

4.3.3.1 Methodology

In Approach #2 the maximum SRSS stress resultants in a selected region on the containment were regenerated by applying a set of equivalent static loads using the modal decomposition method. Five critical buckling regions were selected, Load Cases 1 to 5 in Table 4.2. Five sets of equivalent static loads were generated to examine buckling in every region separately. Potential buckling regions are illustrated in Fig. 4.28.

4.3.3.2 Theoretical Background

The modal decomposition method is based on expressing the maximum SRSS stress resultants in a selected region as a linear combination of the modal stress resultants, $N_i\Phi$, as follows:

$$\{N_{i_{max}}\} = [N_i^{\phi}]\{\psi\} \tag{4.7}$$

The values of $\{\psi\}$ can be interpreted as the combination of the individual modes that superimpose to produce the maximum SRSS seismic response. The $\{\psi\}$ values are determined by the least squares approach that minimizes the square of the error between the values $N_{i_{max}}$ and the regression equation. Next, the modal inertial forces at each node are computed for each mode i as

$$F_i^{\phi} = m\omega_i^2 \phi_i \tag{4.8}$$

where,

F_i^{ϕ} = Modal inertia load at each node for mode i.

ϕ_i = Displacement at node in mode i.

The set of equivalent static loads, F, at each node were computed as a linear combination of the modal inertia loads using the least squares coefficient as follows:

$$F = \sum F_i^{\phi} \Psi_i \tag{4.9}$$

where the sum is for all contributing modes. As a check, the equivalent static loads, F, were applied to the containment and the resulting stress resultants were compared to the maximum stress resultants in the selected region. The stress resultants in other critical regions were also checked to ensure that they were less than the maximum SRSS stress resultants in those regions.

4.3.4 Load Case 1

The buckling strength of the containment was examined at the support where the maximum $N_{i_{max}}$ occurred (at the 260.63° meridian). The set of equivalent static loads were determined by the modal decomposition method (Sec. 4.3.3.2) using the first twenty modes. The stress field was examined and high stress concentration regions that exceeded the maximum SRSS values were recognized at penetrations. Hence, only the first three modes were selected in the regression analysis, as they possess the major contribution to $N_{i_{max}}$ at the support at θ equals to 260.63°.

The least squares coefficients, ψ_1, ψ_2 and ψ_3, were 1.2608, 1.2508 and 0.0640 for mode one, two and three, respectively. The stress field from these equivalent static loads enveloped the SRSS stress resultants in the critical region (see Fig. 4.29) at the support and was less than N_{1max} in the other four critical regions.

The buckling analysis was conducted (Sec. 4.3.2.1.4) and the load factor was plotted versus radial displacement at an Elev. 90.62 ft and θ equals to 260.63°, (see Fig. 4.30). The containment lost stability at a load level of 1.91 when excessive displacements took place near the containment base as shown in Fig. 4.31.

4.3.5 Load Case 2

A possible buckling interaction can occur between local stresses at the support and the lower air lock for Load Case 2. The vibration modes included in this case were modes 1, 2, 3, 6, 11, 12 and 14. The stress field generated by the equivalent static loads was in good agreement in the region and the maximum response was not exceeded elsewhere in the containment. Figure 4.32 shows a comparison of the regenerated stress resultants, N_1 and the maximum seismic response, N_{1max}.

The buckling analysis was accomplished as described in Sec. 4.3.2.1.4. The load multiplier was plotted versus the maximum radial displacement at an Elev. 97.5 ft. and θ equals to 340°, (see Fig. 4.33). The load multiplier at which the shell lost its stability was 1.914 which was slightly greater than the critical load factor for Load Case 1 because the peak value of $N_{1\,max}$ was less than that of Load Case 1 by only 0.9%. The deformed shape of the containment at λ_L is illustrated in Fig. 4.34. Buckling interaction effects were not significant.

4.3.6 Load Case 3

Local buckling due to concentrated loads at the equipment hatch penetration was investigated in this load case. A set of equivalent static loads was computed using the modal decomposition method with the first twenty modes of vibration. The least squares coefficients exhibited unreasonable contributions of the high frequency modes where local vibrations occurred at the top

of the containment. As an alternative, only modes 1, 2, 3, 4, 5, 9, 10, 13 and 14 were incorporated as they contribute significantly in this region. The resulting stress field compared well to the maximum SRSS stress resultants. However, far from the equipment hatch, the stress resultants significantly exceeded N_{1max}, which may result in an under estimation of the buckling strength. As a result, the modal decomposition procedure could not be used to examine local buckling behavior at the equipment hatch. A simply axisymmetric ring load on the edge of the hatch barrel was used as the equivalent static load (Fig. 4.31). It was applied parallel to the barrel axis in the negative X' direction with a magnitude such that the stress resultants enveloped the N_{1max} and N_{2max} at the equipment hatch reinforcing collar. The stress field obtained with the ring load is compared to the maximum seismic response of the containment in Figs. 4.36 in the first row of elements in the reinforcement collar. The equivalent static stress resultants bound the peak values of N_{1max}. At the same time N_{1max} are not exceeded elsewhere in the containment.

The equivalent static ring load was added to the external pressure, temperature, and gravity loads and the buckling analysis was conducted as presented in Sec. 4.3.2.1.4. The load factor at buckling was 2.46. The radial deflection of the equipment hatch barrel was plotted versus the load factor in Fig. 4.37 where excessive deflections took place after the critical load factor λ_L was exceeded. The deformed shape of the containment at λ_L is illustrated in Fig. 4.38.

4.3.7 Load Case 4

Local buckling at the upper air lock penetration was examined in this load case. An equivalent static axisymmetric load was applied on the penetration barrel (see Fig. 4.31) to regenerate the peak meridional stress resultants $N_{1\,max}$ which took place at the hatch reinforcing collar. The stress fields generated by the equivalent axisymmetric load and the maximum seismic response are illustrated in Fig. 4.39 for the first row of elements in the reinforcement collar. The equivalent static stress resultants bounded the peak values of $N_{1\,max}$ and did not exceed it anywhere else in the containment.

The equivalent static ring load together with the external pressure, temperature and gravity loads were applied proportionally in a nonlinear buckling analysis seeking the critical load multiplier. The containment had not buckled at a load factor of 2.96, hence it was recognized that this was as

not the governing load case and the analysis was terminated. The radial deflection of the upper air lock barrel was plotted versus the load factor in Fig. 4.40. The deformed shape at the upper air lock at λ equals to 2.96 is illustrated in Fig. 4.41. This analysis revealed that the reinforcement around the upper air lock provided an adequate strength to prevent local buckling due to concentrated loads.

4.3.8 Load Case 5

Local buckling due to concentrated loads at the lower air lock was investigated in this load case. An equivalent static ring load was applied on the penetration barrel to regenerate the peak seismic meridional stress resultants $N_{1\,max}$ in this potential buckling region (see Table 4.2). The stress field generated by the equivalent ring load enveloped $N_{1\,max}$ in the first row of elements in the reinforcing collar as shown in Fig. 4.42. On the other hand, the maximum stress resultants $N_{1\,max}$ were not exceeded anywhere in the containment. The nonlinear buckling analysis was conducted by applying the equivalent static ring load on the lower air lock barrel together with the external pressure, temperature and gravity loads (see Sec. 4.3.2.1.4). The radial deflection of the lower air lock barrel was plotted versus the load multiplier in Fig. 4.43. The containment lost its stability at a load factor The nonlinear buckling analysis was conducted by applying the equivalent static ring load on the lower air lock together with the external pressure, temperature and gravity loads (see Sec. 4.3.2.1.4). The containment did not lose stability until a load factor of 2.52, consequently this was not the governing load case and the analysis was terminated. The radial deflection of the lower air lock barrel was plotted versus the load multiplier in Fig. 4.43. The deformed shape of the lower air lock at λ equals to 2.52 is illustrated in Fig. 4.44. This analysis indicates that the reinforcing collar of the lower air lock provides an adequate strength against local buckling due to concentrated loads. The deformed shape of the containment at λ_L is depicted in Fig. 4.44.

4.4 Discussion of Results

In this chapter the buckling strength of the System 80+ containment was evaluated. Five critical buckling locations were recognized (Table 4.2). The critical load factor, λ_L, was determined for each load case. The minimum value of, λ_L, was 1.91 for which buckling occurred at the base at θ equals to 260.63° (Load Case 1). Reinforcement at all penetrations enhanced the containment

resistance against local buckling even though high meridional stress resultants were generated near penetrations. The factor of safety for Level C Service Limit obtained from the three dimensional analysis satisfies the requirements of the Code Case N-284, but it does not fulfill the margin of safety of the ASME code. The analysis is conservative, primarily because the SRSS 10% method is conservative.

4.5 References

4.1 Newmark, N. M. and Hall, W. J., "Earthquake Spectra and Design," Vol. 3, Earthquake Engineering Research Institute, 1982.

4.2 Newmark, N. M. et al., "Development of Criteria for Seismic Review of Selected Nuclear Power Plants," NUREG-CR/0098, May, 1978.

4.3 Greimann, L. et al., "System 80+™ Containment Structural Design Review," NUREG-CR/5957, May 1993.

4.4 Hibbitt, Karlson and Sorenson, Inc., "ABAQUS User's Manual," 1994.

4.5 Manuals and Reports on Engineering Practice No, 58, Structural Analysis and Design of Nuclear Plant Facilities, American Society of Civil Engineers, 1980.

4.6 Kelkar, V. S. and Sewell, R. T., "Analysis and Design of Shell Structures," Prentice-Hall, Inc., 1987.

4.7 Coats, D. W. et al., "Recommended Revisions to Nuclear Regulatory Commission Seismic Design Criteria," NUREG-CR/1161, June 1980.

4.8. American Society of Mechanical Engineer, Boiler and Pressure Vessel Code Case N-284," Metal Containment Shell Buckling Design Methods," Supplement #2 to Nuclear Code Case Book, 1980.

5. SUMMARY AND CONCLUSIONS

5.1 Summary

The objective of the present work is to check the adequacy of the System 80+™ containment against local and global buckling.

The System 80+™ containment is a free standing spherical steel shell with 100 ft inner radius and 1.75 inches wall thickness. It is embedded in a concrete base with a flexible transition region. The steel is Type SA537 - Class 2. The major penetrations are the equipment hatch and two personnel air locks.

The axisymmetric stress/buckling analysis of the System 80+™ containment was performed with BOSOR4 and BOSOR5 finite difference programs. The stresses due to the individual loads (dead loads, internal and external pressures and temperatures) were computed using the stress analysis option in BOSOR4. The seismic loads were determined using response spectra for the Safe Shutdown Earthquake. The seismic analysis consisted of a response spectrum analysis utilizing the square root of the sum of the squares with the ten percent method. The stress intensities for the load combinations specified in Section 3.8.2 of U.S. Nuclear Regulatory Commission Standard Review Plan were checked with respect to the allowable values for different service limits and were found to be below the allowable limits. The load combination with the largest compressive stress was utilized in the buckling analysis. An imperfection sensitivity analysis was conducted to find the worst imperfection. The imperfection amplitude was selected to meet with the ASME code requirements. The material nonlinearities were incorporated using a constitutive relationship derived from the equations for the plasticity reduction factor in Code Case N-284. The factor of safety for Service Level C was found to be 2.35. A buckling analysis under seismic loading beyond SSE was also performed. Dead load was first applied and held constant. The seismic loading was increased until buckling occurred at a load multiplier of 2.91.

The three dimensional buckling analysis was conducted with ABAQUS software. Results for elastic buckling and inelastic buckling problems from ABAQUS were verified with the classical theory of elasticity stability and BOSOR. A three dimensional model of the System 80+™ containment including all penetrations was generated. The mass of the containment spray header

system and electrical penetrations were included in the three dimensional model. The finite element mesh was selected based on a mesh sensitivity study that incorporates p- refinement and h- refinement. The transition region at the base was modeled as springs with nonlinear load deflection behavior. An axisymmetric imperfection was incorporated into the model.

The modal response due to the seismic loading for the first twenty modes of vibration were obtained and assembled through a response spectrum analysis. The modal stress resultants were combined using the ten percent method. Sets of equivalent static loads were computed to regenerate the maximum SRSS stress resultants at five potential buckling regions.

Pressure, temperature and gravity loads were added to the equivalent static loads and the buckling behavior was predicted for the five loading cases. The smallest buckling safety factor was found to be 1.91 for the first load case with buckling occurring at the support. This factor of safety was less than that obtained from the BOSOR analysis, as the axisymmetric analysis did not account for closely spaced modes (see Appendix A). The safety factors against local buckling at the equipment hatch, upper air lock and lower air lock were larger than 1.91. The factor of safety of 1.91 meets the requirements of the Code Case N284, whereas it is inadequate for the ASME requirements (NE 3222). The buckling factors of safety at the penetrations satisfied both the ASME code and Code Case N284. The analysis is considered conservative because the SRSS 10% method is overly conservative for shell type of structures.

5.2 Conclusions

On the basis of the analyses presented herein, the following can be concluded:

1. Based on the stress analysis with the revised seismic response spectra and an axisymmetric stress analysis, all stress intensities were below the allowable limit as specified in Section NE3221 of the code.

2. The predicted buckling factor of safety for Service Level C was 2.35 using the axisymmetric analysis.

3. From the axisymmetric analysis, the buckling factor of safety under seismic loading and dead load only is 2.91.

4. The minimum buckling factor of safety obtained from the three dimensional analysis was 1.91 for Service Level C with buckling near the base. The safety factor of 1.91 meets the requirements of the Code Case N-284, whereas it does not satisfy NE 3222 of the ASME code. The analysis is overly conservative for at least two reasons: (1) Equivalent static loads to represent the dynamic seismic loads neglect the interaction between inertial forces and buckling forces, and (2) the SRSS 10% method over estimates the effects of closely spaced modes (Appendix A), especially for shell type of structures.

5. The local buckling strength at the penetrations is adequate.

5.3. Recommendations

Time integration analysis that incorporates geometric and material nonlinearities is recommended where inertia loads interact with other loads to estimate the response of the containment in the time domain.

APPENDIX A
STRESS RESULTANTS AT THE SUPPORT USING TEN PERCENT METHOD

A.1 Description of the Problem

Consider a spherical shell similar to the System 80+™ containment geometric configuration except without penetrations. The shell is subjected to horizontal ground excitation that has two equal components along the global X and Y directions as shown in Fig. A.1. The following discussion describes how SRSS meridional stress resultants are obtained at the base.

A.2 Modal Frequency Analysis

Consider only the first two horizontal modes, which are cantilever beam modes in two orthogonal directions X' and Y'. Since the shell is axisymmetric (no penetrations), the direction X' of the fundamental mode is arbitrary and can be assumed at an angle α from the global X direction as shown in Fig. A.1. The natural frequencies of the first two modes are identical and equal to f, the participation factors for X and Y earthquakes, Γ_x and Γ_y, respectively, are shown in Table A.1.

A.3 Modal Stress Resultants at Base

The distribution of the meridional stress resultants at the base in the first and second modes N_1^{ϕ} and N_2^{ϕ}, respectively, are illustrated in Fig. A.2 and given by

$$N_1^{\phi} = a \cos(\theta-\alpha)$$
$$N_2^{\phi} = a \sin(\theta-\alpha) \qquad (A.1)$$

where a is the peak value of the modal stress resultants N_1^{ϕ} and N_2^{ϕ}.

A.4 Response Spectrum Analysis

A.4.1 Modal Combination

The peak response in the first two modes due to the horizontal excitation in the X direction can be computed using the design spectra method [Ref. A.1] as:

$$N_{1x} = N_1^{\phi}\,\Gamma_{1x}\,S_{1x} = a\cos(\alpha)\cos(\theta-\alpha)\,S_{1x} \qquad (A.2)$$
$$N_{2x} = N_2^{\phi}\,\Gamma_{2x}\,S_{2x} = a\sin(\alpha)\sin(\theta-\alpha)\,S_{2x}$$

The modal combination is accomplished by the ten percent method [Eq. 4.2] rule. Since the two modes have the same frequency, they are closely spaced modes and the spectral displacements S_{1x} and S_{2x} are the same and equal to S_x. Therefore, the peak response for the X earthquake is:

$$N_{max\,x} = \{\, N_{1x}^2 + N_{2x}^2 + 2\,|\,N_{1x}\,N_{2x}\,|\,\}^{1/2} \qquad (4.2)$$

$$= a\,S_x\,\{\,\cos^2\alpha\cos^2(\theta-\alpha) + \sin^2\alpha\sin^2(\theta-\alpha)$$
$$+ 2\,|\,\cos\alpha\sin\alpha\cos(\theta-\alpha)\sin(\theta-\alpha)\,|\,\}^{1/2} \qquad (A.3)$$

Similarly the peak responses in the two modes due to the excitation in the Y direction can be computed:

$$N_{1y} = N_1^{\phi}\,\Gamma_{1y}\,S_y = a\cos(\alpha)\cos(\theta-\alpha)\,S_y \qquad (A.4)$$
$$N_{2y} = N_2^{\phi}\,\Gamma_{2y}\,S_y = a\sin(\alpha)\sin(\theta-\alpha)\,S_y$$

Since the two modes have identical frequencies then:

$$N_{max\,y} = a\,S_y\,\{\sin^2\alpha\cos^2(\theta-\alpha) + \cos^2\alpha\sin^2(\theta-\alpha)$$
$$+ 2\,|\,\cos\alpha\cos(\theta-\alpha)\sin\alpha\sin(\theta-\alpha)\,|\,\}^{1/2} \qquad (A.5)$$

A.4.2 Directional Combination

The maximum seismic response N_{max} can be estimated by assembling the peak response due to each horizontal excitation using the SRSS method [Eq. 4.3]. Since the two horizontal excitations

are identical the value of the spectral displacements S_x and S_y will be the same and the maximum response is:

$$N_{max} = a\,S\,\{\,1 + 4\,|\,\cos\alpha\,\cos(\theta-\alpha)\,\sin\alpha\,\sin(\theta-\alpha)\,|\,\}^{1/2} \qquad (A.6)$$

Eq. A.6 shows that N_{max} at the base will be dependent on the angle α. Figure A.3 illustrates the distribution of N_{1max} which takes the shape of two sinewaves. The peak values of N_{max} occur at circumferential angles θ of $\alpha+n\pi/4$ (n=1,3,5,7) where maximum modal coupling occurs. However, at $\alpha+n\pi/4$ (n=0,2,4,6) no modal coupling took place due to modal orthogonality (see Fig. A.2). The distribution of N_{max} obtained by the ten percent rule (Fig. A.3) is similar to the distribution of N_{max} at the support for the System 80+™ containment (Fig. 4.16).

A.4.3 Maximum Response by the SRSS Method

The maximum response computed by the SRSS method is,

$$N_{max} = \{N_{max\,x}^2 + N_{max\,y}^2\}^{1/2} = a\,S \qquad (A.7)$$

The distribution of N_{max} at Sec S-S (Eq. A.7) obtained from the SRSS method is constant and independent of the angle α.

Comparing Eq. A.7 and A.6, the effect of the modal coupling is introduced by the term $(4\,|\,\cos\alpha\,\cos(\theta-\alpha)\,\sin\alpha\,\sin(\theta-\alpha)\,|\,)$. Figure A.3 compares N_{max} at the base by the ten percent rule (Eq. A.6) to that obtained by SRSS method (Eq. A.7).

If the earthquake components are applied along the modal directions X' and Y', i.e. angle α is zero, the modal coupling term in Eq. A.6 will be zero, and the SRSS ten percent method will give the same distribution of N_{max}. This was the case in the axisymmetric analysis [Ref. A.4], in which modal coupling according to the ten percent method was not incorporated.

A.5 References

A.1 Paz, M., "Structural Dynamics, Theory and Computation," Van Nostrand Reinhold, Third Edition, 1991.

A.2 American Society of Civil Engineers, Manuals and Reports on Engineering Practice No. 58, Structural Analysis and Design of Nuclear Plant Facilities, 1980.

A.3 Newmark, N. M. and Hall, W. J., "Earthquake Spectra and Design," Earthquake Engineering Research Institute, March 1982.

A.4 L. Greimann, et al., "System 80+™ Containment Structural Design Review," NUREG CR-5957 prepared for NRC, Washington, May 1993.

Table 1.1 Factors of Safety for ASME Service Limits

Service Limits	Factor of Safety		
	NE-3222.2	NUREG 1.57*	Case N-284
Design Conditions	3.0	-	2.00
Level A & B	3.0	-	2.00
Level C	2.5	2	1.67
Level D	2.0	2	1.33

*Does not explicitly identify the service limit except as being associated with the loading causing the largest compressive stress.

Table 2.1 Design Conditions (Table 2.2 in Ref. 2, revised 7-7-93)

SRP Reference Number	Description*	Design Allowable Stress Intensity Limit			Maximum Calculated Stress Intensity	
		Type*	Limit	Value (psi)	Value (psi)	Elev.
(ii)	D+L+P_a+T_a+R_a (P_a=-2 psi, T_a=110°F)	P_m	1.0 S_{mc}	22,000	2,154	94.1
(ii)	D+L+P_a+T_a+R_a (P_a=53 psi, T_a=290°F)	P_m	1.0 S_{mc}	22,000	19,197	98.2

*Definition of variables in the column is given in Table 2.6.

Table 2.2 Level A Service Limits (Table 2.3 in Ref. 2, revised 7-7-93)

SRP Reference Number	Description*	Design Allowable Stress Intensity Limit			Maximum Calculated Stress Intensity	
		Type*	Limit	Value (psi)	Value (psi)	Elev.
(iii)(a)(1)	$D+L+P_o+T_o+R_o$ (P_o=0, T_o=110°F)	P_m	1.0 S_{mc}	22,000	2,160	94.1
(iii)(a)(1)	$D+L+P_o+T_o+R_o$ (P_o=0, T_o=110°F)	P_L+P_b+Q	3.0 S_{ml}	80,100	10,852	86.3
(iii)(a)(2)	Not applicable					
(iii)(a)(3)	$D+L+P_a+T_a+R_a$ (P_a=-2, T_a=110°F)	P_m	1.0 S_{mc}	22,000	2,154	94.1
(iii)(a)(3)	$D+L+P_a+T_a+R_a$ (P_a=-2, T_a=110°F)	P_L+P_b+Q	3.0 S_{ml}	80,100	10,170	86.3
(iii)(a)(3)	$D+L+P_a+T_a+R_a$ (P_a=53, T_a=290°F)	P_m	1.0 S_{mc}	22,000	19,197	98.2
(iii)(a)(3)	$D+L+P_a+T_a+R_a$ (P_a=53, T_a=290°F)	P_L+P_b+Q	3.0 S_{ml}	80,100	78,786	86.3

*Definition of variables in this column is given in Table 2.6

Table 2.3. Level B Service Limits (Table 2.4 in Ref. 2 no longer applicable)

Table 2.4 Level C Service Limits (Table 2.5 in Ref. 2, revised 7-7-93)

SRP Reference Number	Description*	Design Allowable Stress Intensity Limit (psi)			Maximum Calculated Stress Intensity	
		Type*	Limit	Value (psi)	Value (psi)	Elev.
(iii)(c)(1)	D+L+P_a+T_a+R_a+E′ (P_a=-2,T_a=110°F,E′=SSE)	P_m	1.0 S_y	59,500	18,759	92.7
(iii)(c)(1)	D+L+P_a+T_a+R_a+E′ (P_a=53,T_a=290°F,E′=SSE)	P_m	1.0 S_y	52,480	29,961	94.1
(iii)(c)(2)	D+L+P_o+T_o+R_o+E′ (P_o=0,T_o=110°F,E′=SSE)	P_m	1.0S_y	59,500	18,732	92.7
(iii)(c)(3)	Not applicable					

*Definition of variables in this column is given in Table 2.6.

Table 2.5 Level D Service Limits (Table 2.6 in Ref. 2, revised 7-7-93)

SRP Reference Number	Description*	Design Allowable Stress Intensity Limit			Maximum Calculated Stress Intensity	
		Type*	Limit	Value (psi)	Value (psi)	Elev.
(iii)(d)(1)	$D+L+P_a+T_a+R_a+Y_r+Y_j+Y_m+E'$ (P_a=-2,T_a=110°F,E'=SSE)	P_m	S_f	47,600	18,759	92.7
(iii)(d)(1)	$D+L+P_a+T_a+R_a+Y_r+Y_j+Y_m+E'$ (P_a=53,T_a=290°F,E'=SSE)	P_m	S_f	47,600	29,961	94.1
(iii)(d)(2)	Not applicable					

*Definition of variables in this column is given in Table 2.6.

Table 2.6 Nomenclature

P	Stress Intensity (difference between the algebraically largest and smallest principal stresses, twice the maximum shear stress).
P_m	General primary membrane stress intensity. Average stress across an entire section of a vessel. Not self limiting. Gross deformation occurs if this stress exceeds yield. An example is general membrane stress in a cylinder or sphere with internal pressure. Temperature stresses are not included. Therefore, the temperature increment is set equal to zero in Tables 2.2 to 2.6 in those cases for which P_m is checked. These stresses are checked at the shell middle surface.
Q	Secondary stress intensity. Self-limiting. An example is the stresses due to the bending stress resultants M_1, M_2, M_{12} for pressure or seismic loading. All thermal stresses are secondary. Hence, for those cases in Table 2.2 to 2.6 for which primary plus secondary stresses are checked, the temperature is at the operating or accident level. These stresses are checked at the shell surface.
P_L	Local primary membrane stress intensity. A stressed region may be considered local if the distance over which the membrane stress intensity exceeds 1.1 S_{mc} does not extend in meridional direction more than $(rt)^{1/2}$. Typically self-limiting like a secondary stress but redistribution takes place only after large deformations. An example is the local membrane stress near a gross structural discontinuity such as shell intersections at the springline or at a penetration. Membrane stresses near the base of the containment may be considered in this category.
P_b	Primary bending stress intensity. Same as P_m except bending stress. An example is the center of a flat plate with lateral pressures).
S_y	Yield stress, ASME Table I.2.0: 60,000 psi @ T=0°F; 52,480 psi @ T=290°F; 59,500 psi @ T=110°F.
S_{mc}	Allowable stress intensity, ASME Table I-10.0: 22,000 psi.
S_{ml}	Allowable stress intensity, ASME Table I-1.0: 26,700 psi.
S_f	Allowable stress intensity, 85% of the allowable membrane stress intensity specified in Appendix F: 47,600 psi.
D	Dead loads.
L	Live loads including all loads resulting from platform flexibility and deformation, and crane loading if applicable, equal to zero for this containment.
T_o	Thermal effects and loads during startup, normal operating or shutdown conditions, based on the most critical transient or steady-state condition.

Table 2.6 Nomenclature (continued)	
R_o	Pipe reactions during startup, normal operating or shutdown conditions, based on the most critical transient or steady-state condition, equal to zero for this containment.
P_o	External pressure loads resulting from pressure variation either inside or outside containment.
E	Loads generated by the operating basis earthquake including sloshing effects, if applicable.
E′	Loads generated by the safe shutdown earthquake including sloshing effects, if applicable.
P_a	Pressure load generated by the postulated pipe break accident including P_o, pool swell and subsequent hydrodynamic loads. For this containment, accidental spray actuation is included in this category.
T_a	Thermal loads under thermal conditions generated by the postulated pipe break accident including T_o, pool swell, and subsequent hydrodynamic reaction loads. For this containment, accidental spray actuation is included in this category.
R_a	Pipe reactions under thermal conditions generated by the postulated pipe break accident including R_o, pool swell, and subsequent hydrodynamic reaction loads, equal to zero for this containment.
P_s	All pressure loads which are caused by the actuation of safety relief valve discharge including pool swell and subsequent hydrodynamic loads, equal to zero for this containment.
T_s	All thermal loads which are generated by the actuation of safety relief valve discharge including pool swell and subsequent hydrodynamic thermal loads, equal to zero for this containment.

Table 3.1 Four Mesh Parameters

Parameter		A	B	C	D
No. of elements		2216	580	700	191
Element size at equator		0.89 $\sqrt{rt}$	1.77 $\sqrt{rt}$	1.77 $\sqrt{rt}$	3.56 $\sqrt{rt}$
Element size at support		0.46 $\sqrt{rt}$	0.92 $\sqrt{rt}$	0.46 $\sqrt{rt}$	1.38 $\sqrt{rt}$
Aspect ratio at support		1.45	1.45	2.9	1.76
No. of variables	S4R5	13806	3744	4194	1308
	S8R5	54198	14442	16206	4902
Wave front	S4R5	306	162	162	90
	S8R5	618	330	330	186
R.M.S. wavefront	S4R5	278	145	147	80
	S8R5	563	297	301	166
Storage/ analysis*	S4R5	48.29	6.2	7.31	1.27
	S8R5	326.9	51.95	59.4	9.13
Storage/ increment*	S4R5	6.9	1.8	2.03	0.6
	S8R5	25.5	6.7	7.53	2.22

*Units are in megabytes.

Table 3.2 Sphere with External Pressure

Mesh	S8R5			S4R5		
	λ_c (psi)	% error	time/it. (sec.)	λ_c (psi)	% error	time/it. (sec.)
A	22.1	1.6%	79.13	26.6	18%	12.86
B	23.6	4.9%	16.25	42.5	89%	1.4
C	23.8	5.8%	16.29	44.3	97%	1.47
D	26.4	17.3%	2.46	59.0	162%	0.18

Table 3.3 Sphere with Gravity Loads

Mesh	S8R5			S4R5		
	λ_L	% error	time/it. (sec.)	λ_L	% error	time/it. (sec.)
A	-	-	-	14.18	1.3%	14.63
B	13.69	2.2%	13.00	15.9	13.6%	0.72
C	13.75	1.80%	13.51	14.76	5.4%	1.12
D	14.5	3.60%	12.0	18.87	35%	0.17

Table 4.1 Results of Modal Frequency Analysis

Mode	**Frequency cycle/sec.**	Γ_X	Γ_Y	Γ_Z
1	4.890	1.0376	0.6777	0.0216
2	4.9298	0.6811	1.0442	0.0044
3	10.227	0.1412	0.0965	4.0196
4	10.961	0.0536	0.0962	0.0208
5	11.308	0.4503	0.2542	3.8932
6	12.738	0.0726	0.0273	0.8692
7	12.783	0.1762	0.1843	0.8594
8	13.416	0.1914	0.2188	0.1781
9	13.541	0.2192	0.1091	1.1722
10	14.691	0.2438	0.1439	0.1502
11	14.776	0.0132	0.0092	0.0020
12	14.785	0.0169	0.0131	0.0118
13	14.863	0.0809	0.1268	0.0013
14	15.382	0.0084	0.0014	0.0005
15	16.949	0.0003	0.0015	0.0009
16	17.057	0.0199	0.0057	0.0001
17	17.057	0.0107	0.0073	0.0004
18	17.114	0.0019	0.0104	0.0016
19	17.186	0.0077	0.0161	0.0008
20	17.262	0.0491	0.0120	0.0006

Table 4.2 Peak Values of $N_{1\,max}$ and $N_{2\,max}$ Due to SSE

Potential Buckling Region	$N_{1\,max}$		$N_{2\,max}$		Load Case
	lb/in	Elev. (ft)	lb/in	Elev. (ft)	
Equipment hatch (collar)	22940	148.94	35195	145.30	3
Upper air lock (collar)	16890	152.08	36490	143.51	4
Lower air lock (collar)	19080	117.42	29170	112.95	5
Base (θ=260.63°)	15940	90.62	21070	96.11	1
Base below Lower air lock	15450	90.62	20220	96.11	2
Base below Equipment hatch	11920	90.62	15850	96.11	6

Table A.1 Natural Frequencies and Participation Factors

Mode #	**Frequency**	Γ_x	Γ_y
1	f	$\cos \alpha$	$\sin \alpha$
2	f	$\sin \alpha$	$\cos \alpha$

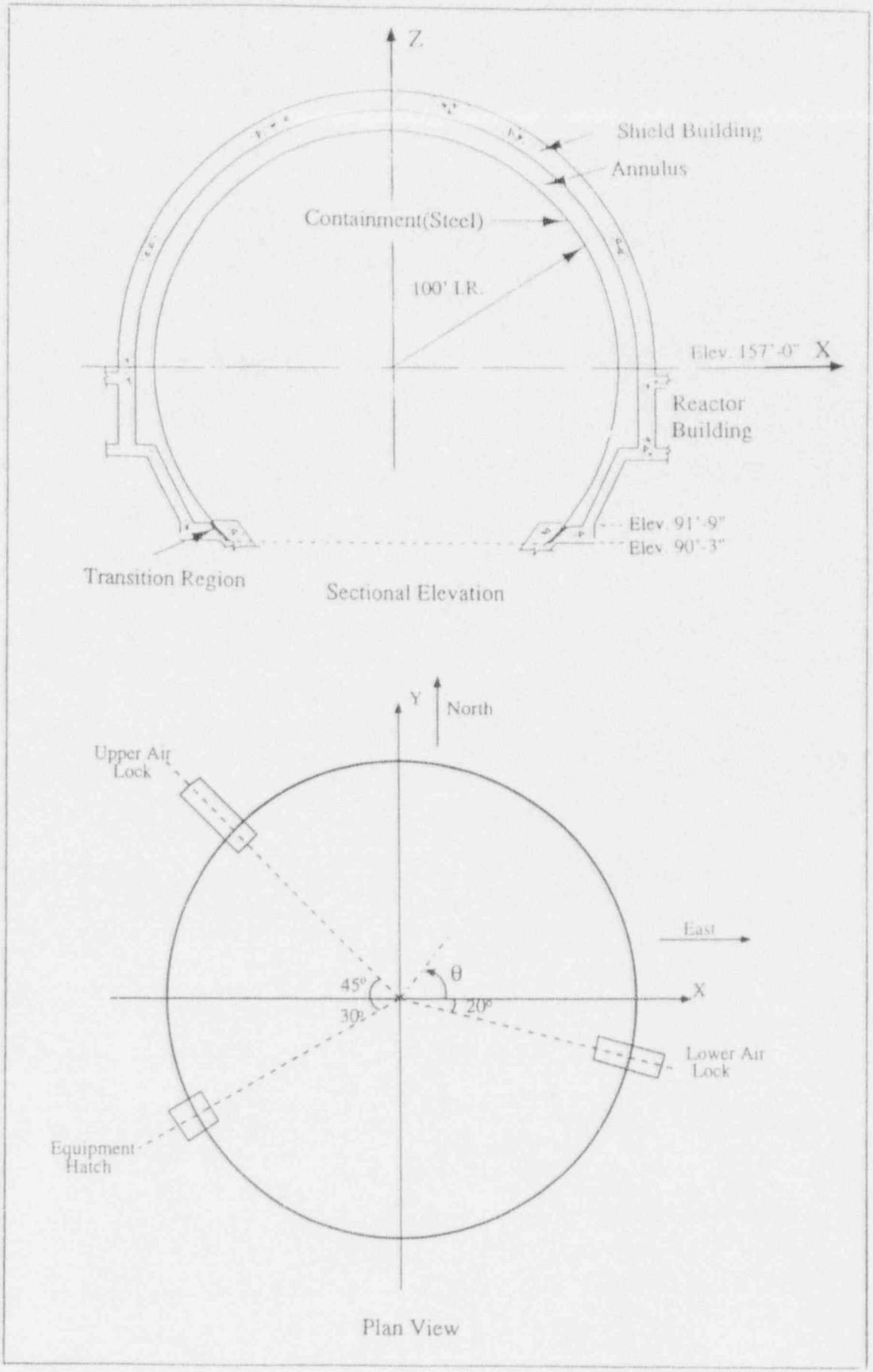

Fig 1.1 System 80+ Containment

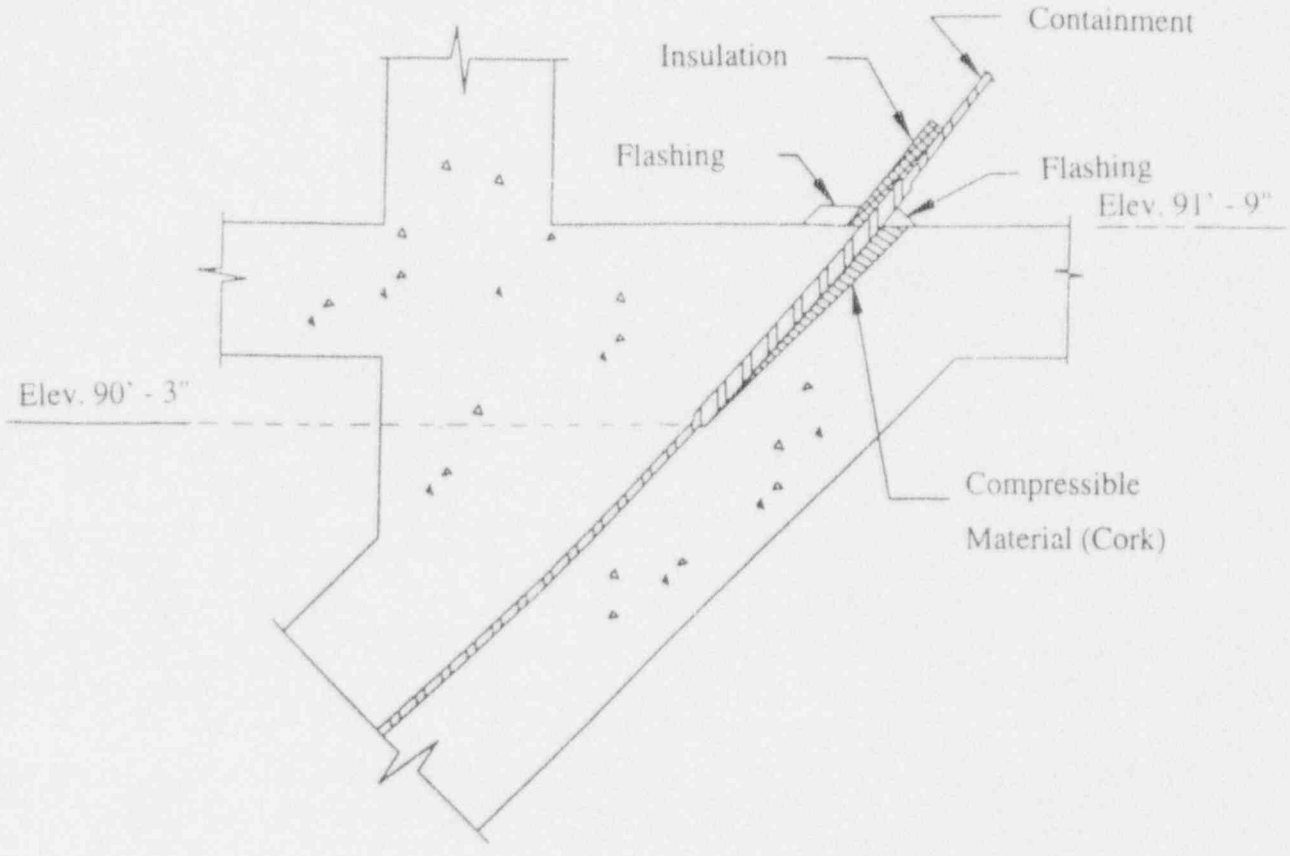

Fig 1.2 Details of Embedment in Concrete Foundation

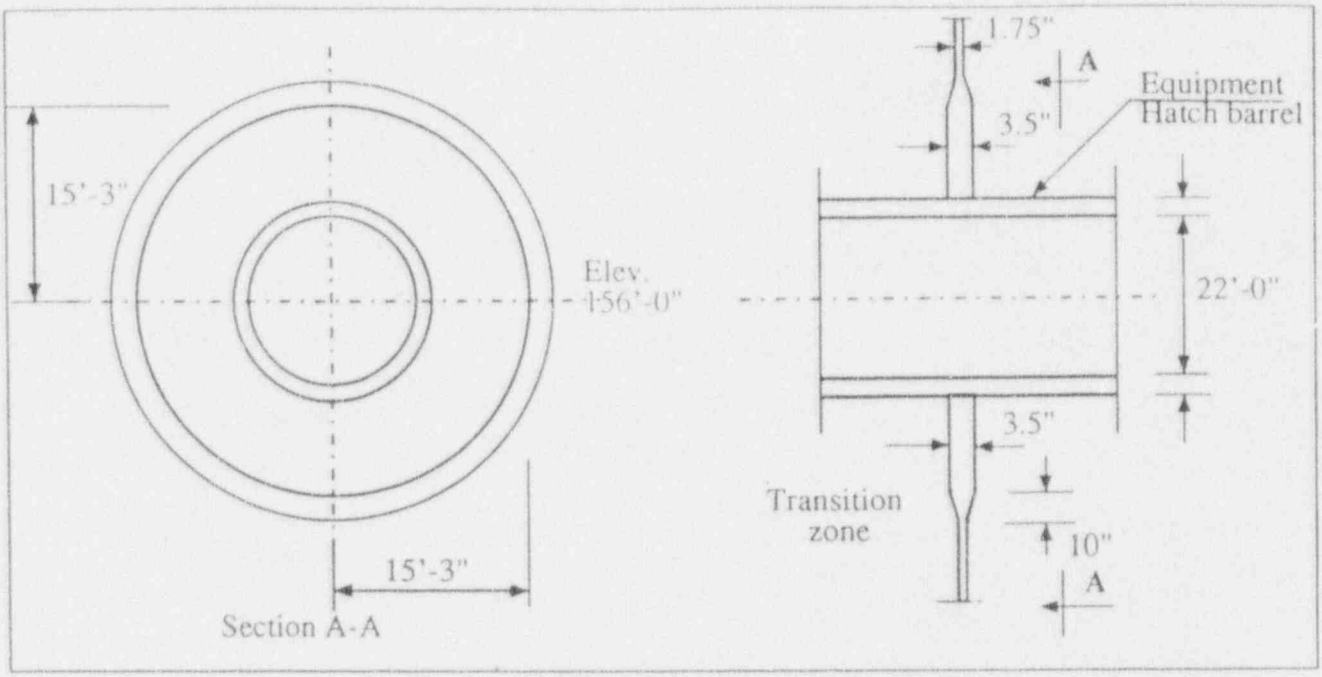

Fig 1.3 Details of the Equipment Hatch

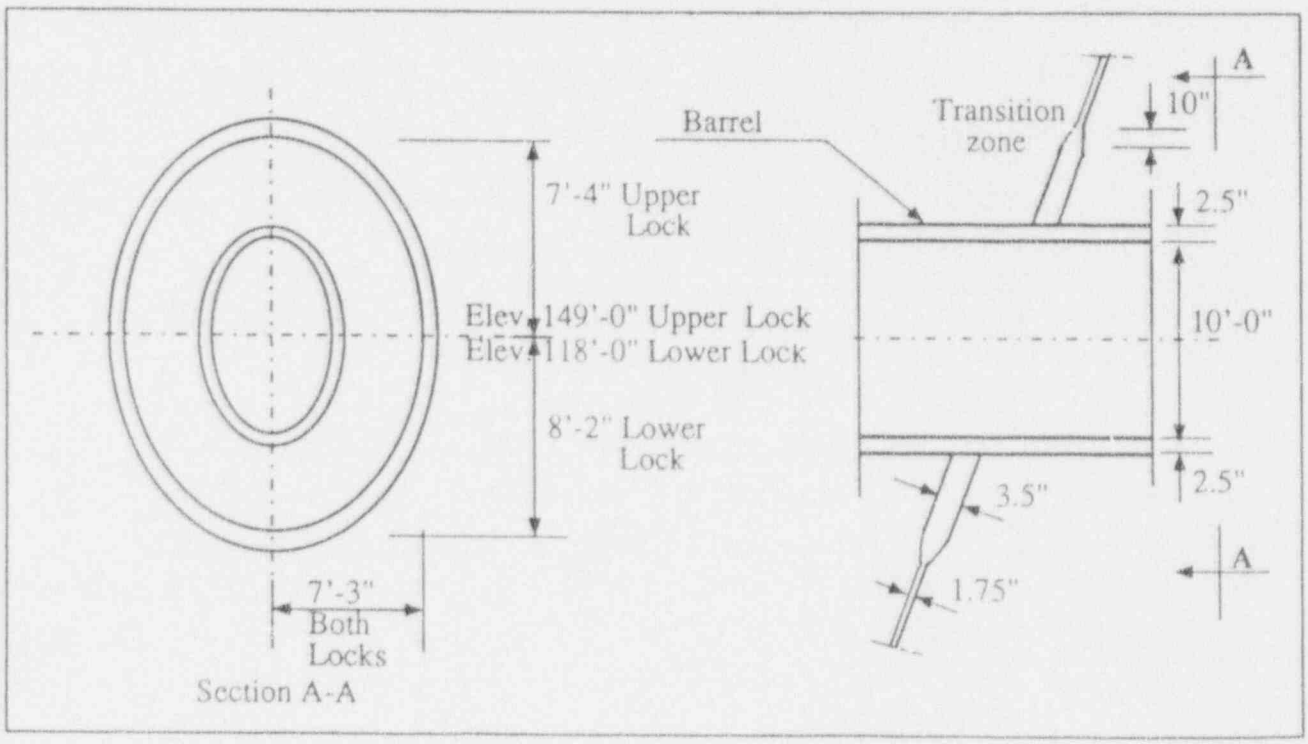

Fig 1.4 Details of Personnel Air Locks

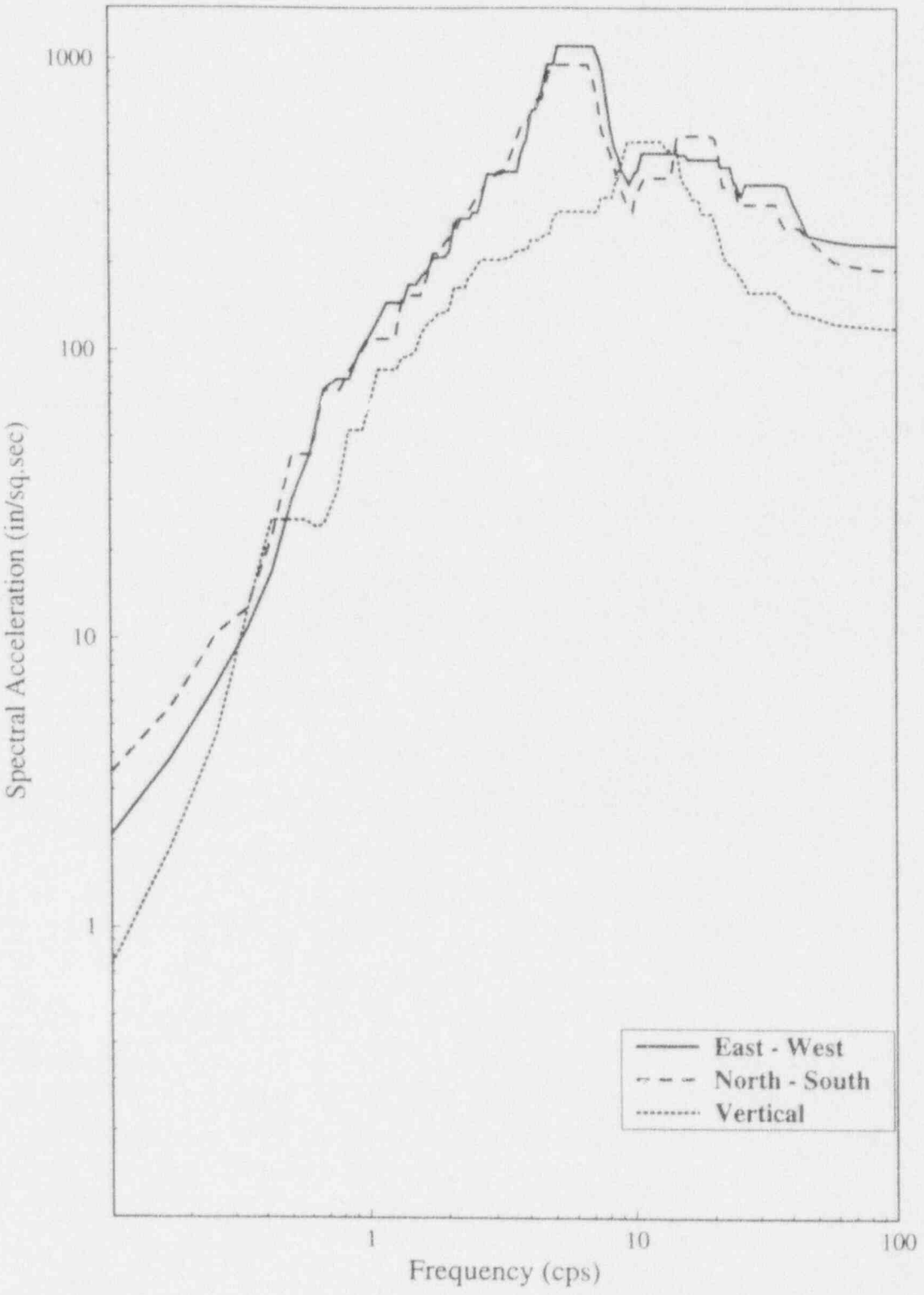

Fig 2.1 New Response Spectra for Safe Shutdown Earthquake (Revised 7-7-93)

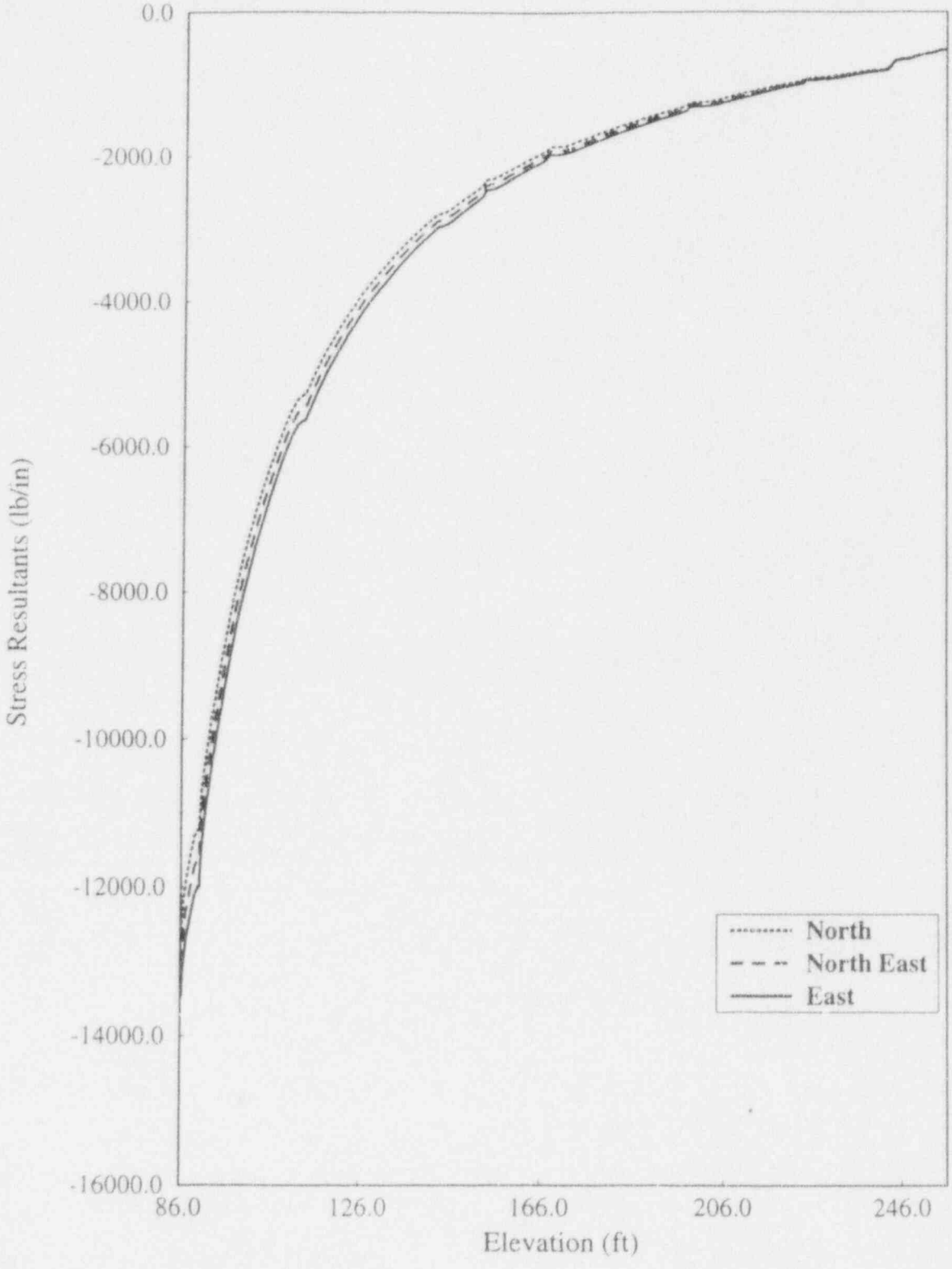

Fig 2.2 Comparison of SRSS Meridional Stress Resultants at East, Northwest and North Meridians.

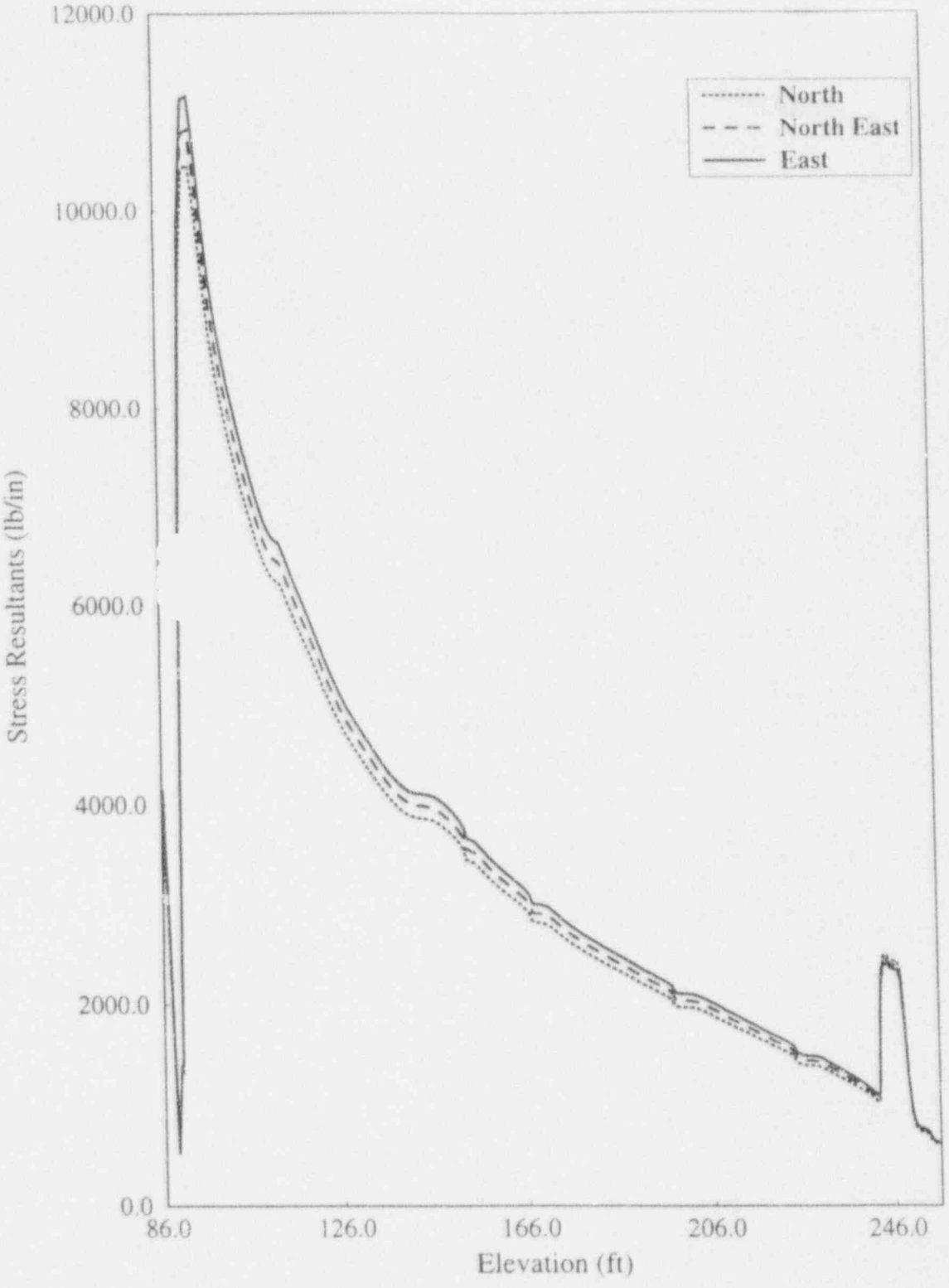

Fig 2.3 Comparison of SRSS Circumferential Stress Resultants at East, Northwest and North Meridians.

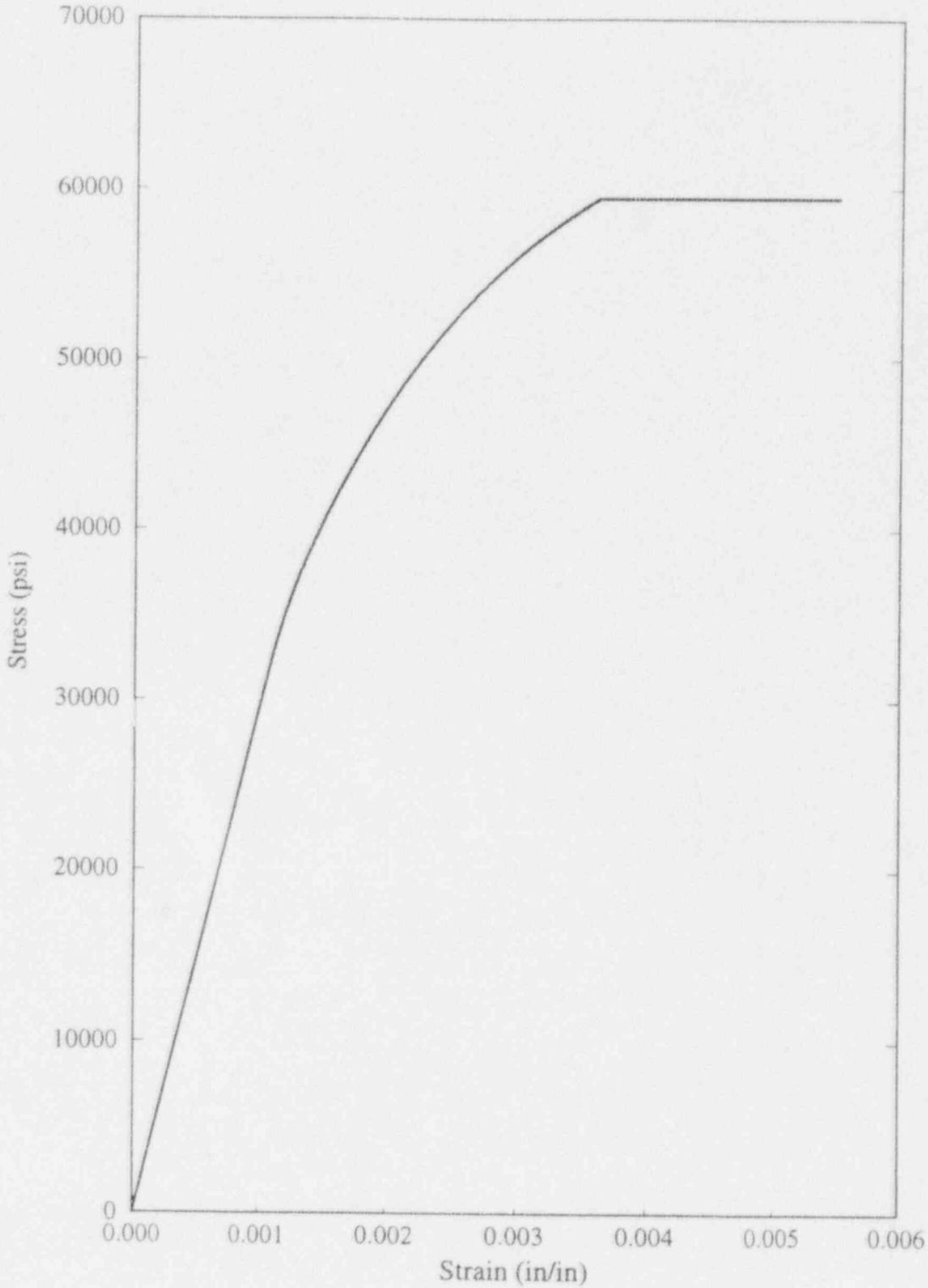

Fig 2.4 Stress - Strain Curve Corresponding to a Temperature of 110°F.

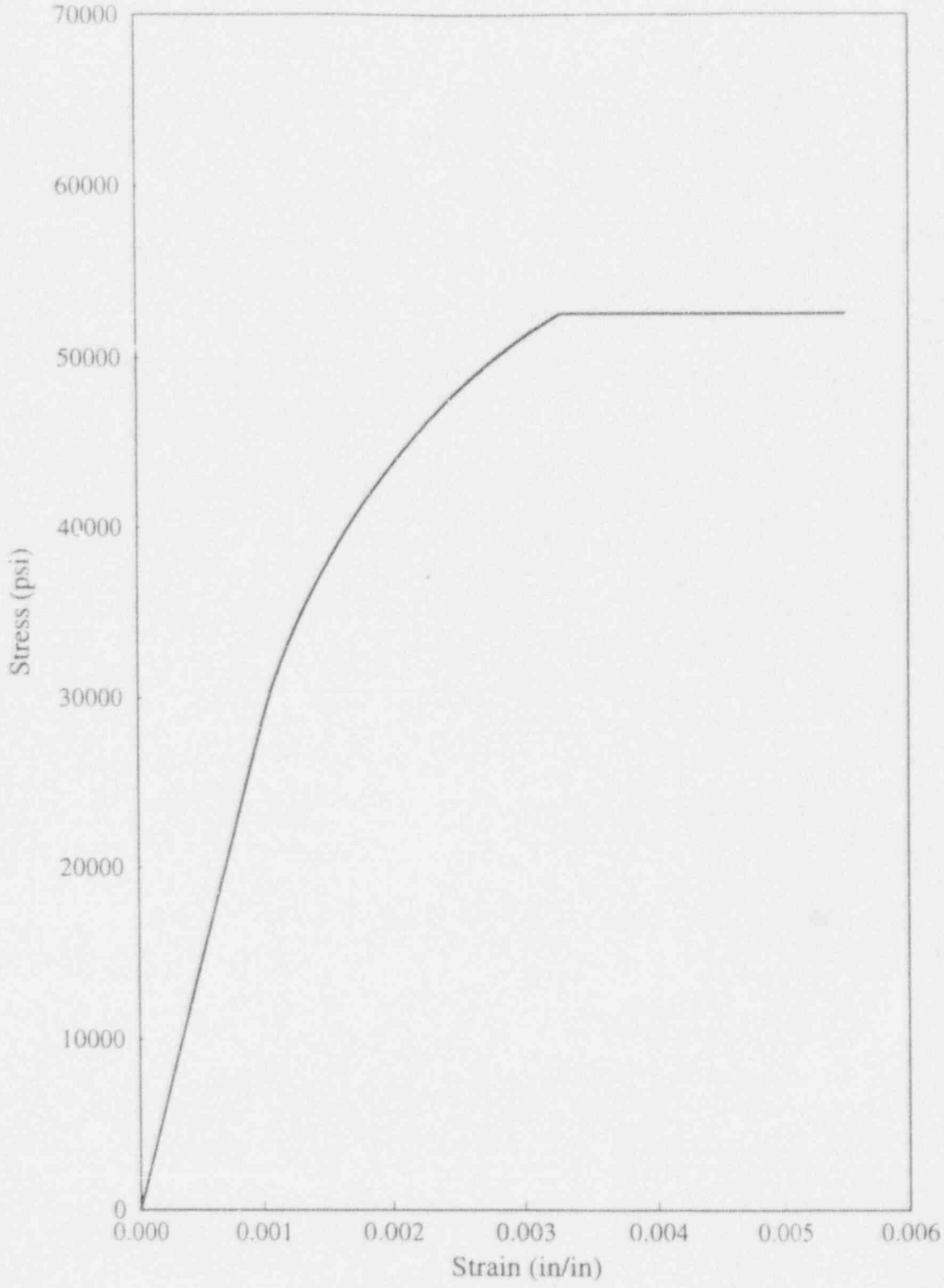

Fig 2.5 Stress - Strain Curve Corresponding to a Temperature of 290°F.

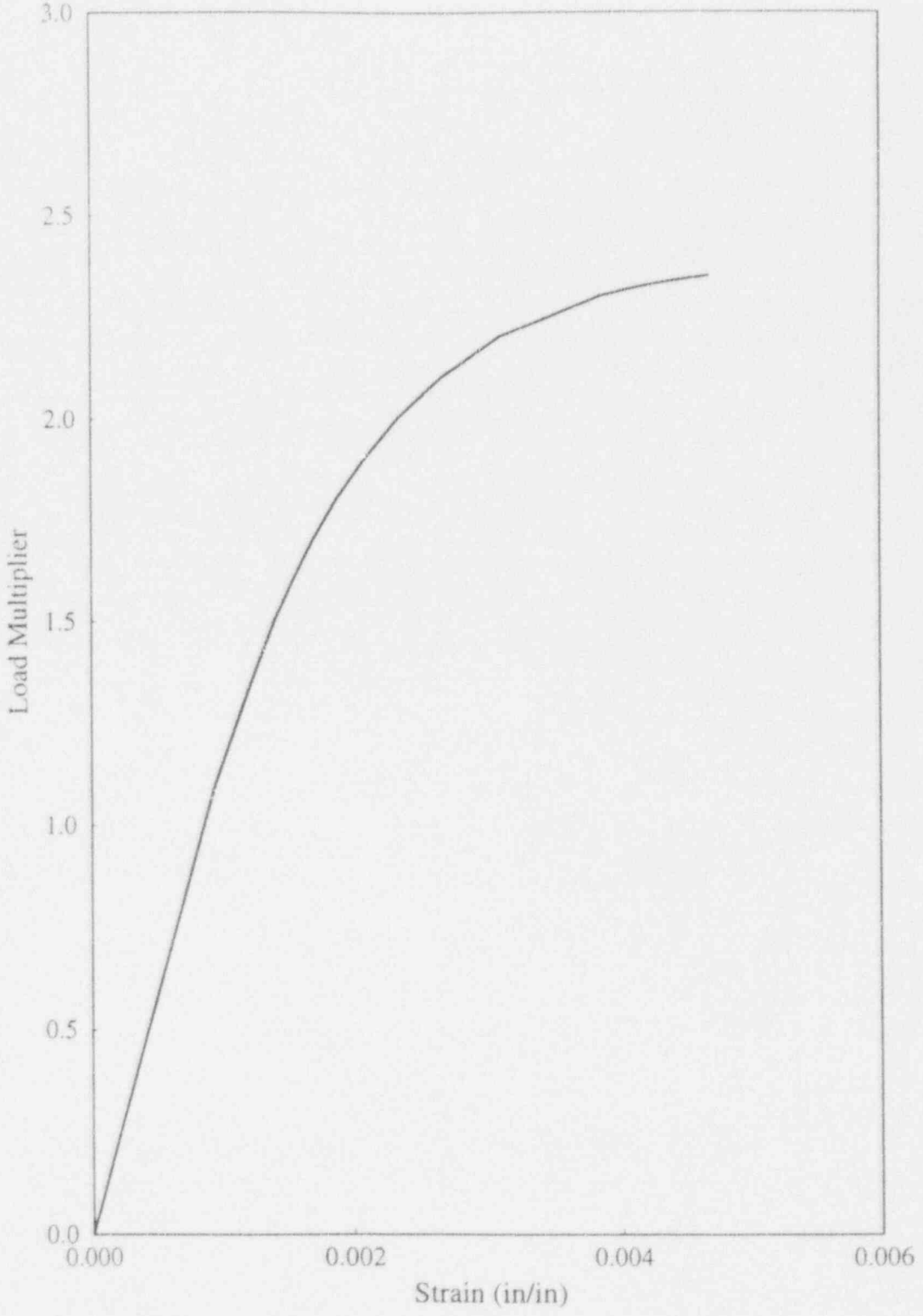

Fig 2.6 Effective Uniaxial Strain at Inner Surface at Elevation 96.8 ft. (Level C Service Limit).

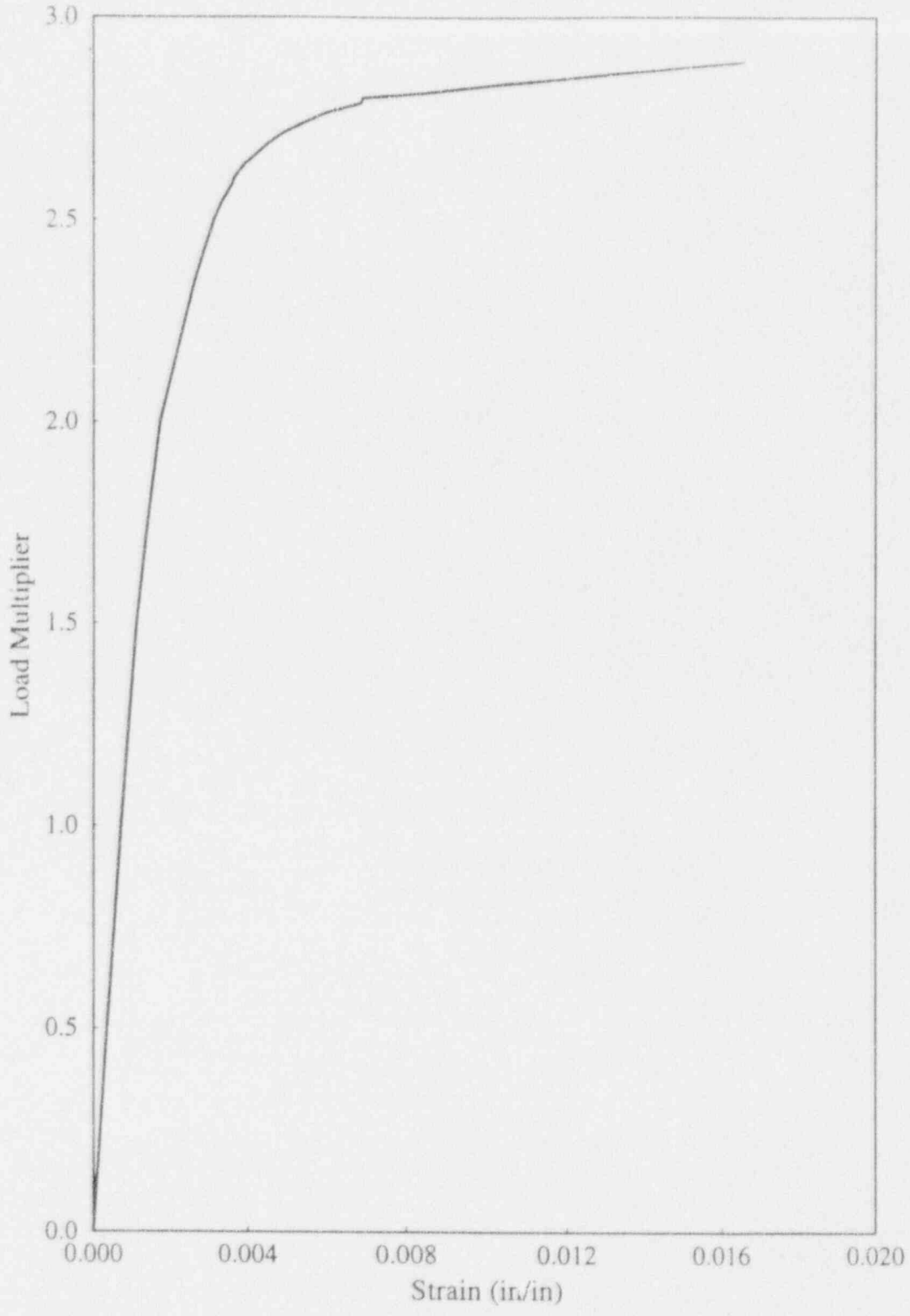

Fig 2.7 Effective Uniaxial Strain at Outer Surface at Elevation 243 ft. (Level A Service Limit).

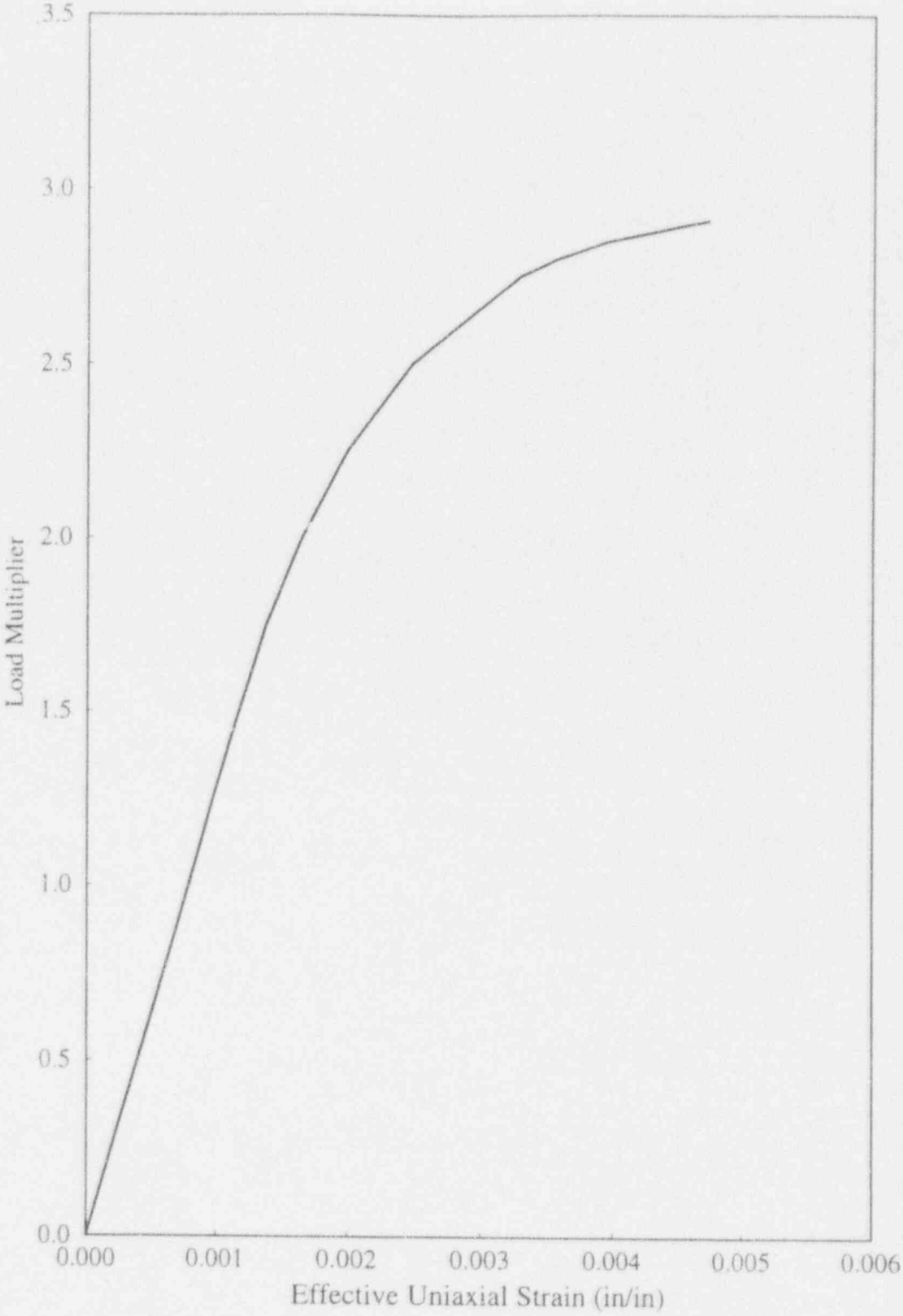

Fig 2.8 Effective Uniaxial Strain at Outer Surface at Elevation 96.8 ft.

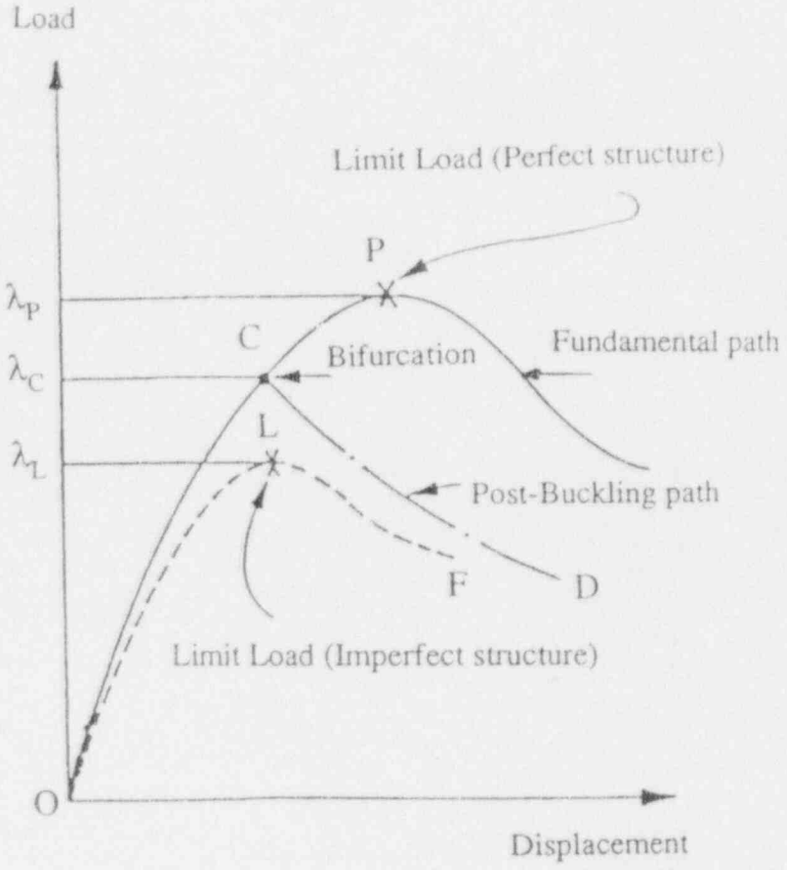

Fig 3.1 Fundamental and Post Buckling Load Displacement Paths

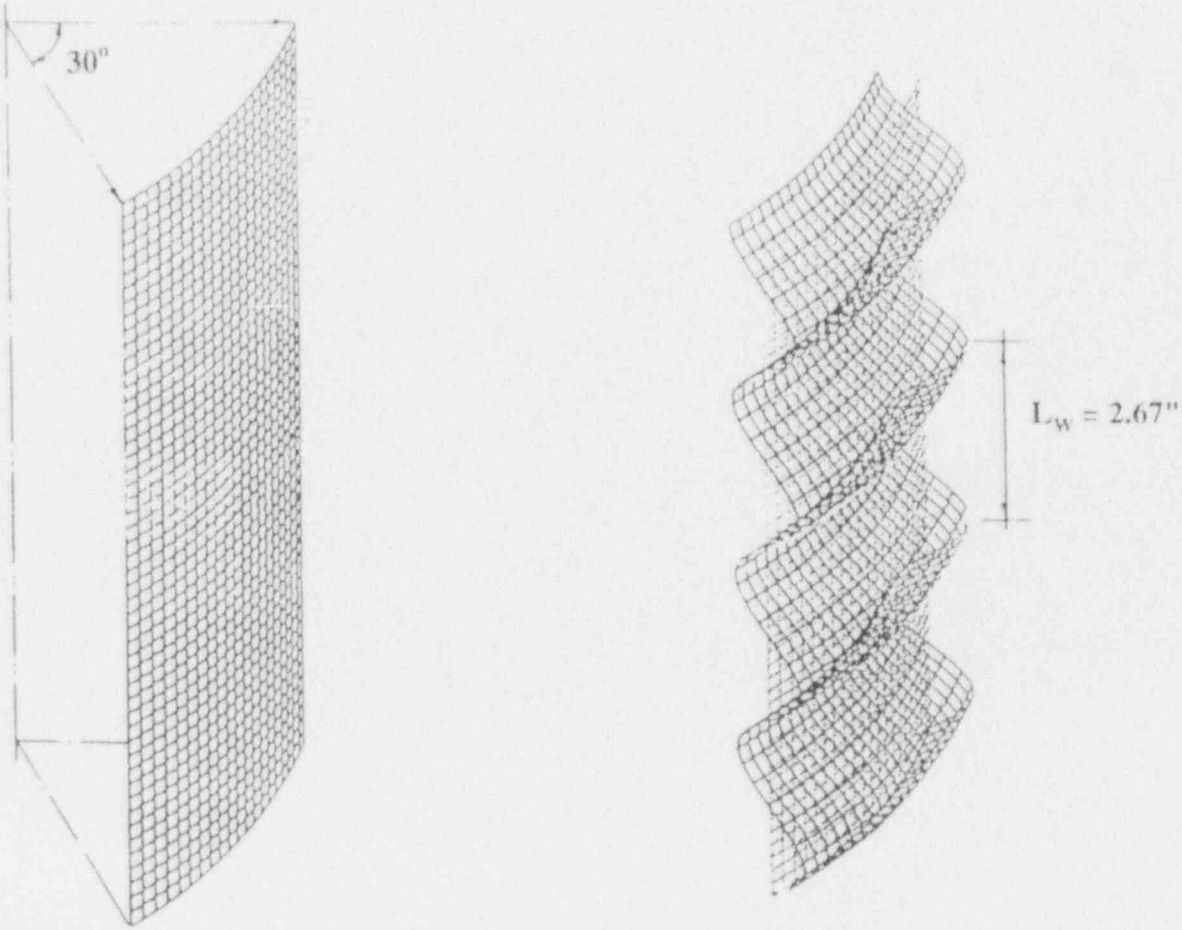

(a) Undeformed Shape (b) Deformed Shape

Fig 3.2 Circular Cylinder Under Axial Load
(Radius = 8 in. , Thickness = 0.08 in.)

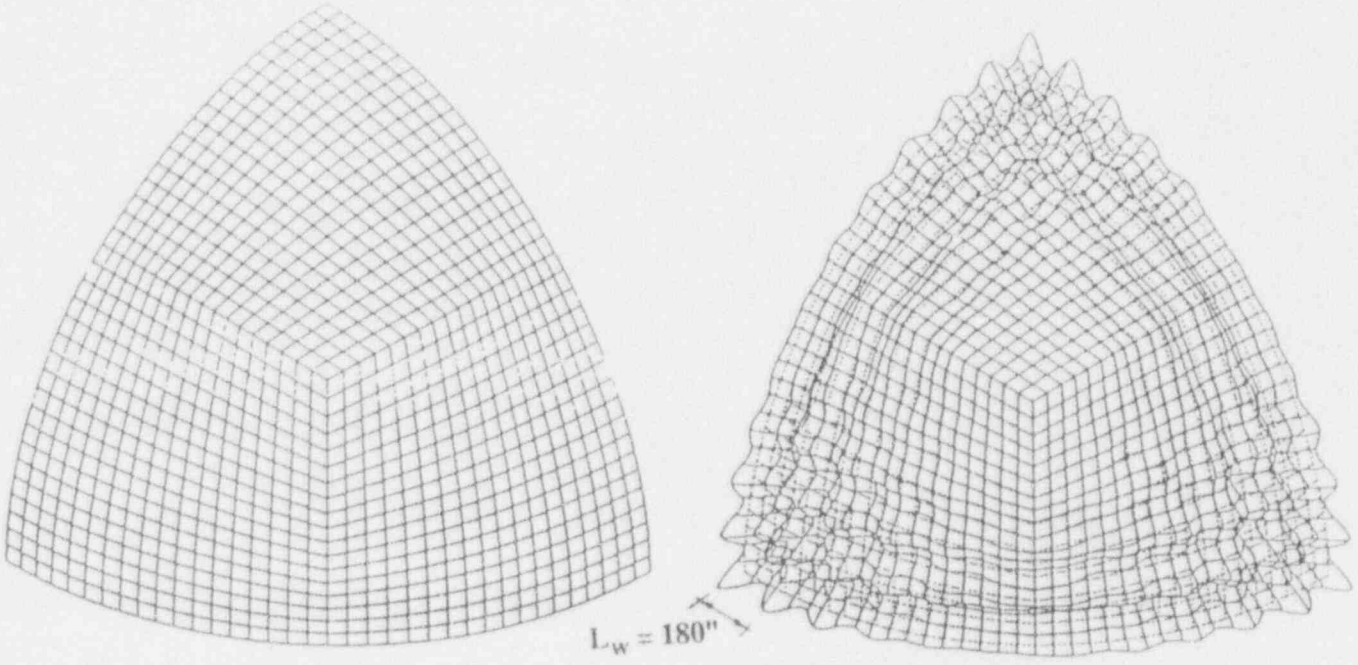

(a) Undeformed Shape (b) Deformed Shape

Fig 3.3 Spherical Shell Under Uniform External Pressure
(Radius = 1200 in. , Thickness = 1.75 in.)

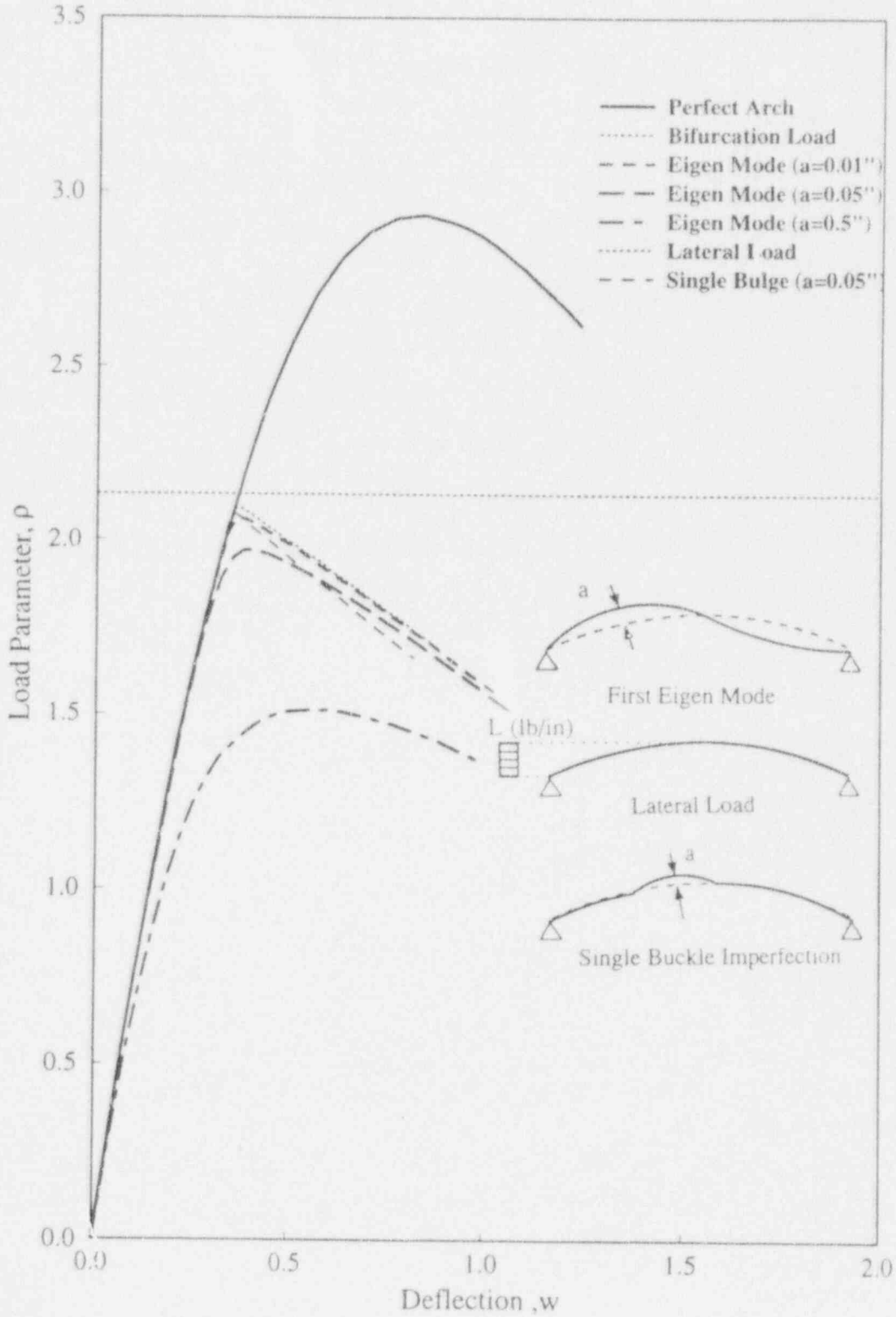

Fig 3.4 Load Deflection Curves of a Two Hinged Arch

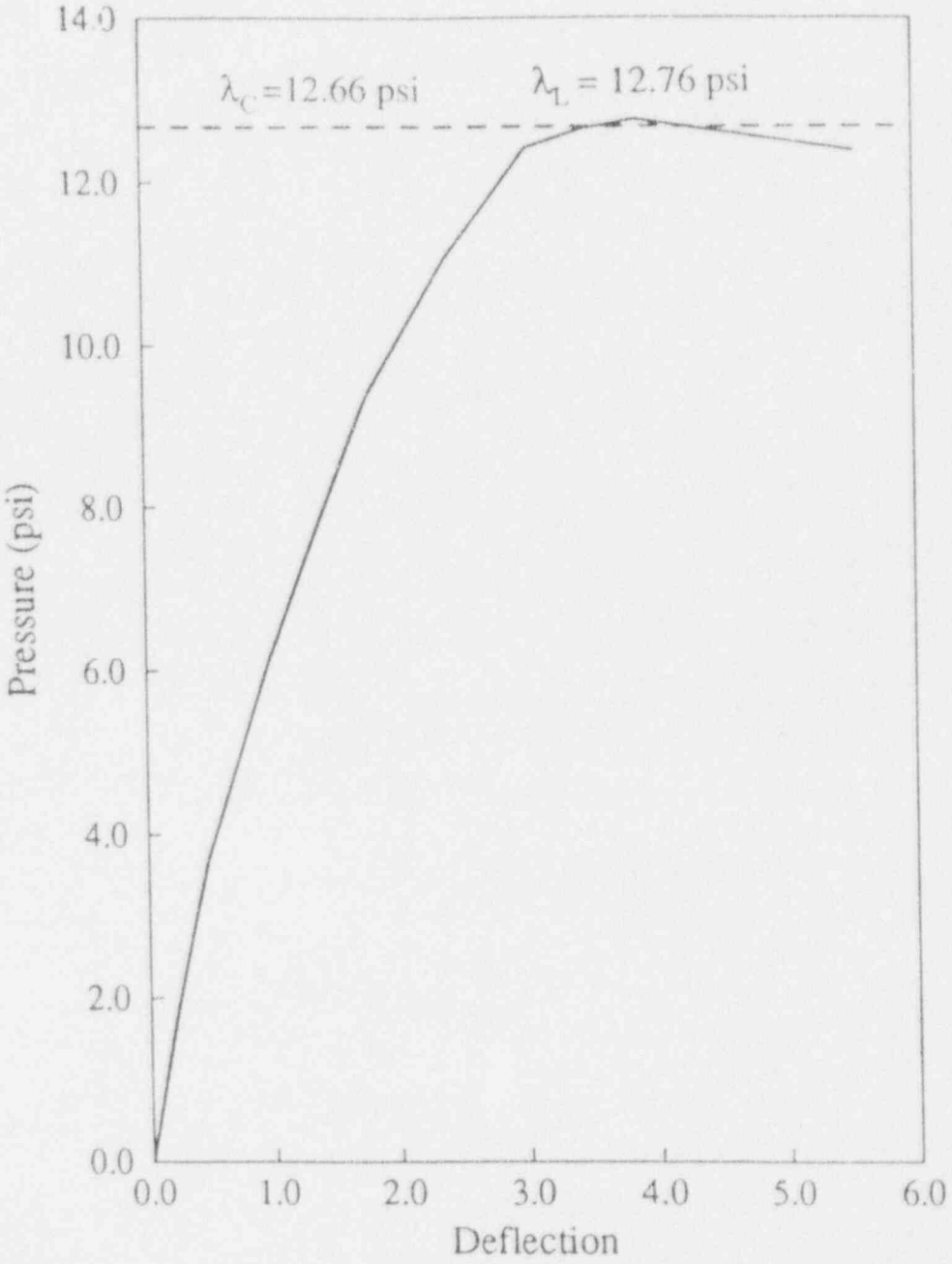

Fig 3.5 Load Deflection Curve of Spherical Shell With an Axisymmetric Imperfection.
(Radius = 1200 in. , Thickness = 1.75 in.)

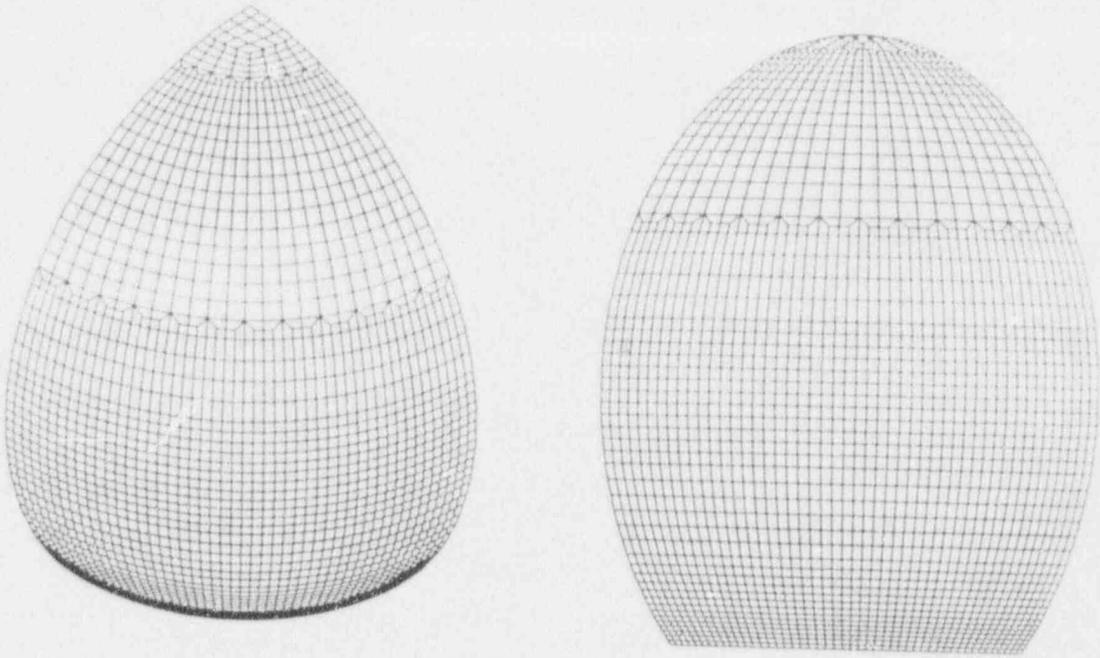

Fig 3.6 Mesh A Configuration

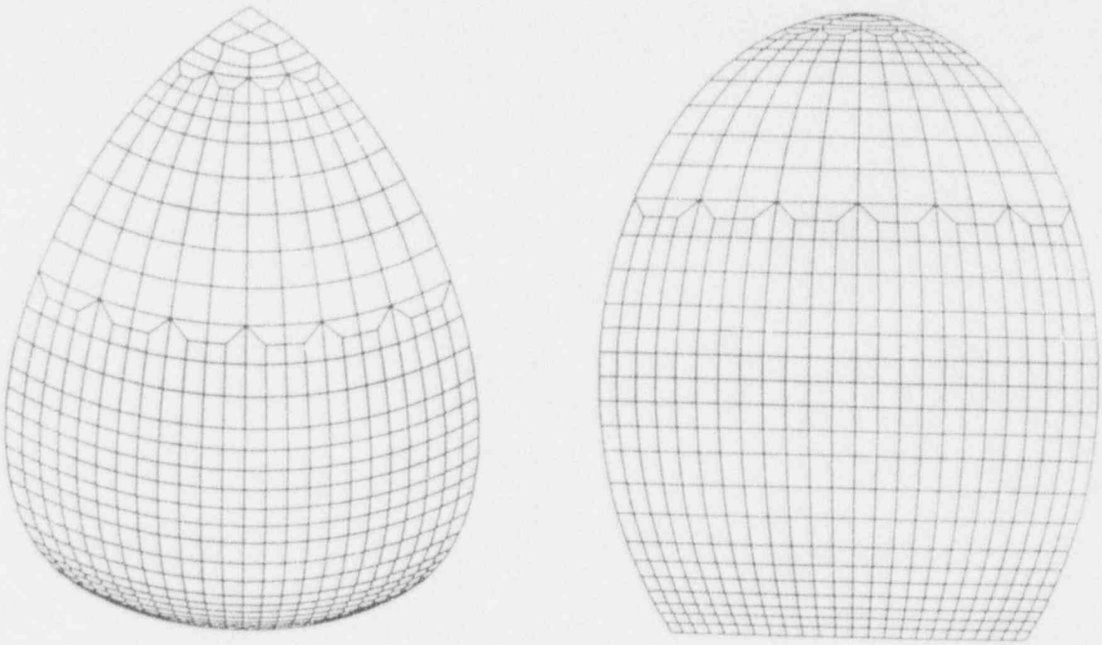

Fig 3.7 Mesh B Configuration

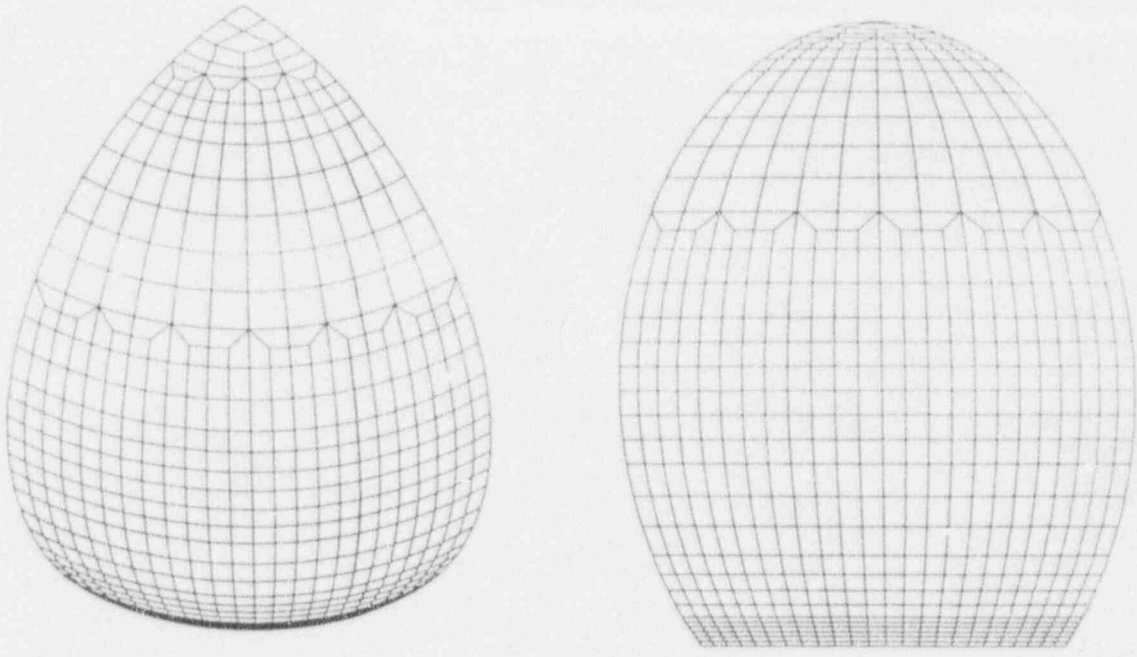

Fig 3.8 Mesh C Configuration

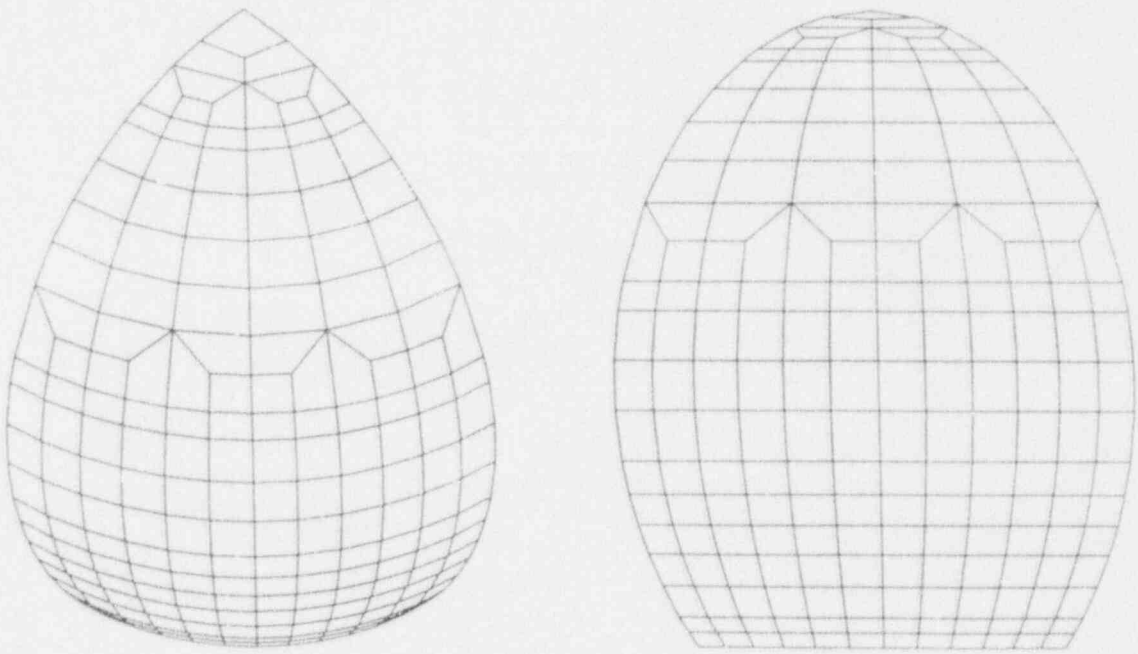

Fig 3.9 Mesh D Configuration

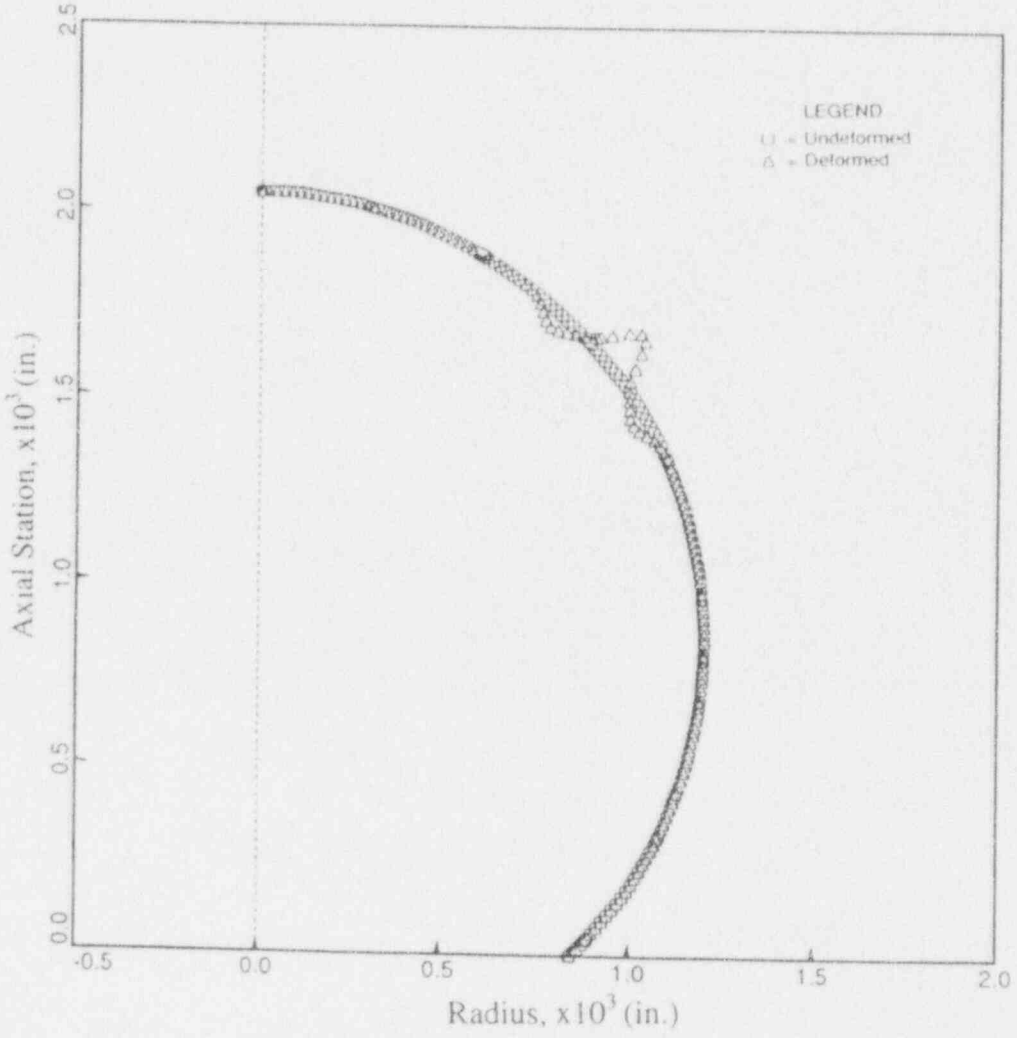

Fig 3.10 Deformed Shape of Sphere with External Pressure (BOSOR Solution)

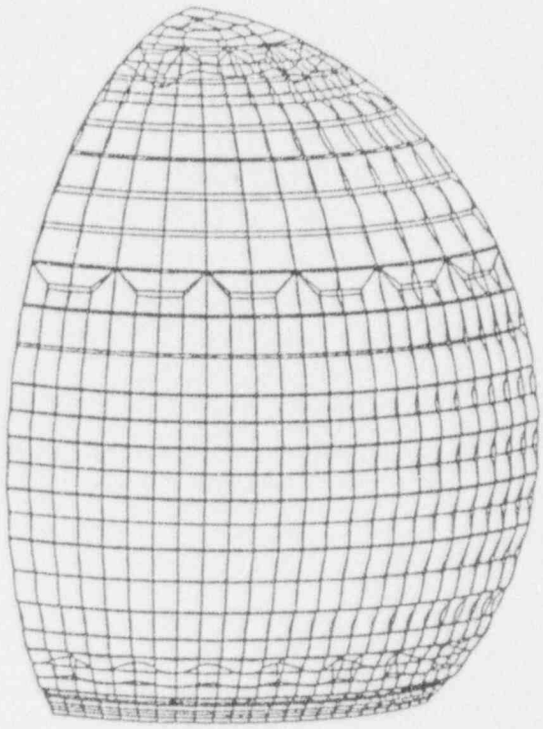

Fig 3.11 Deformed Shape of Sphere with External Pressure (Mesh C)

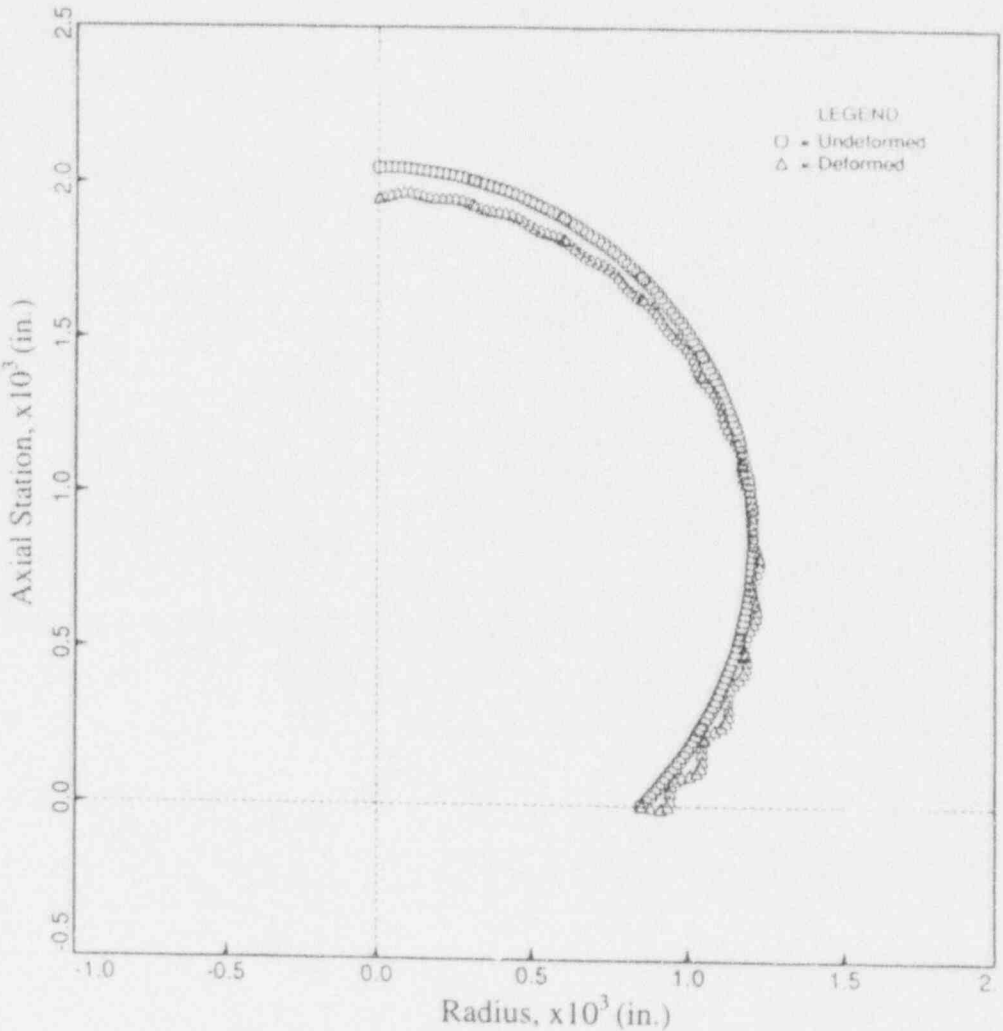

Fig 3.12 Deformed Shape of Sphere with Gravity Loads (BOSOR Solution)

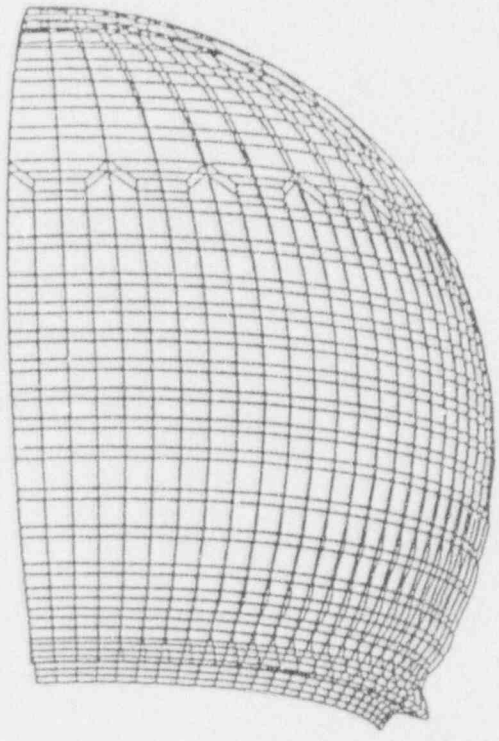

Fig 3.13 Deformed Shape of Sphere with Gravity Loads (Mesh C)

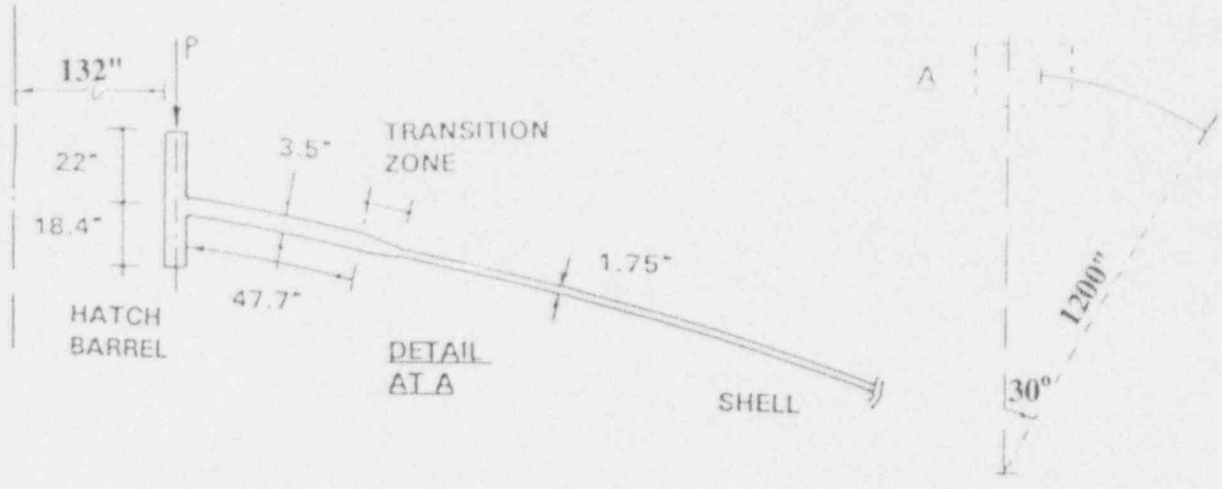

Fig 3.14 Reinforced Opening with Ring Load

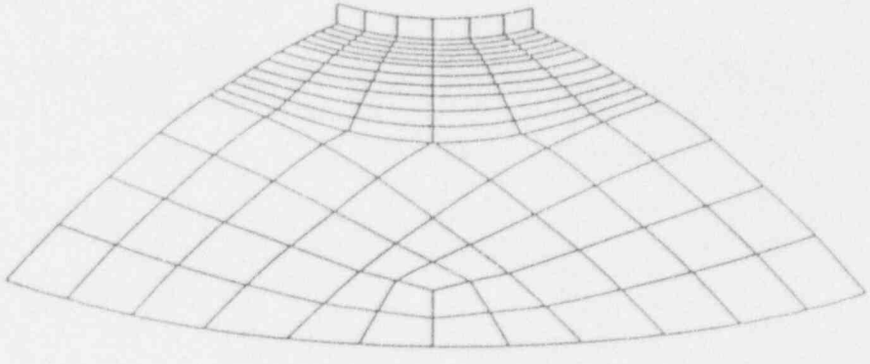

Fig 3.15 Finite Element Model of Sphere ' h Reinforced Opening at the Top

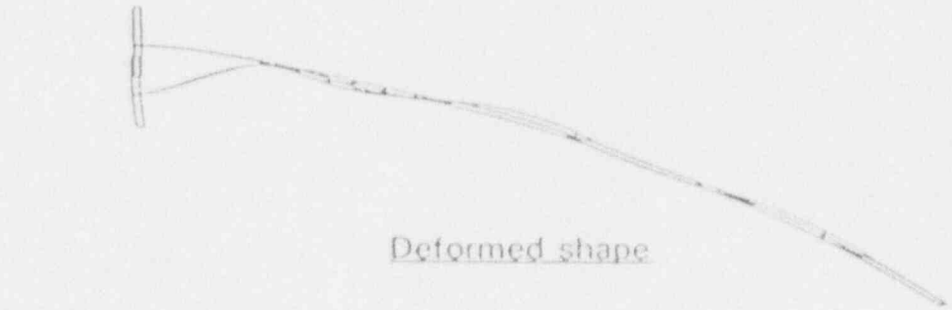

Deformed shape

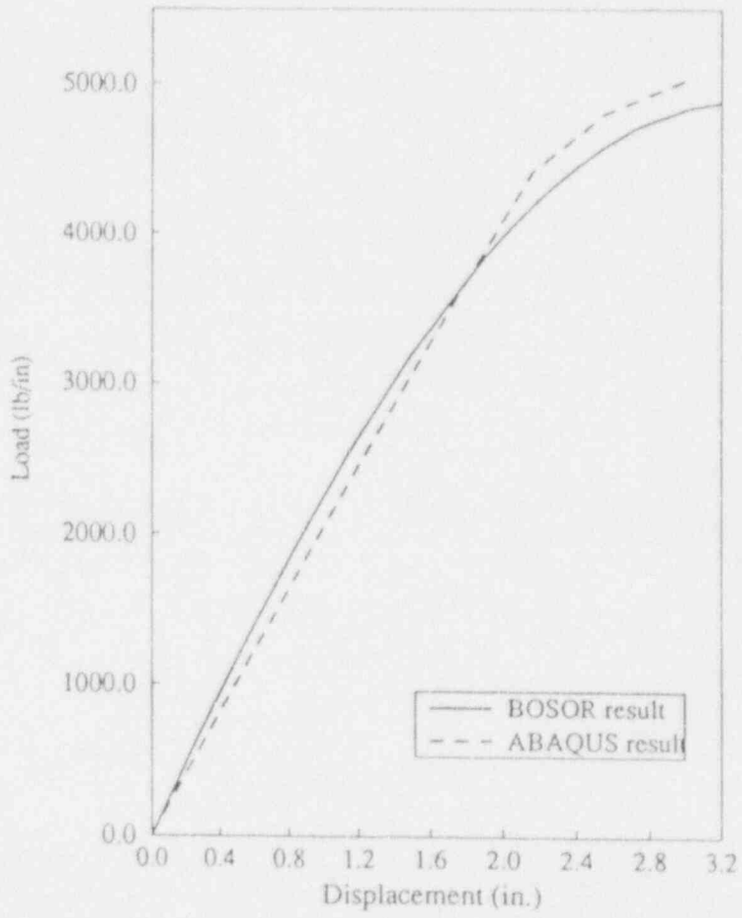

Fig 3.16 Comparison of ABAQUS and BOSOR Results

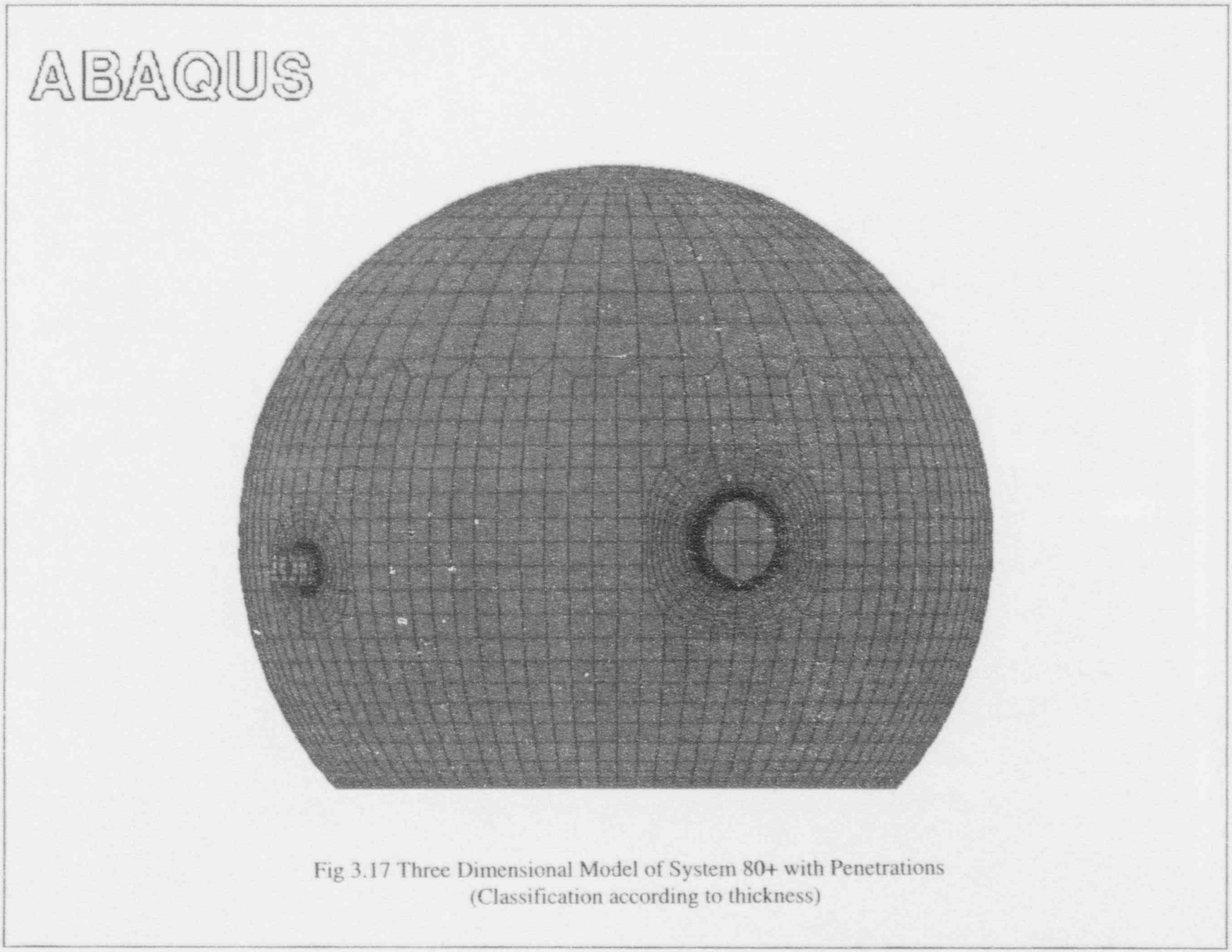

Fig 3.17 Three Dimensional Model of System 80+ with Penetrations
(Classification according to thickness)

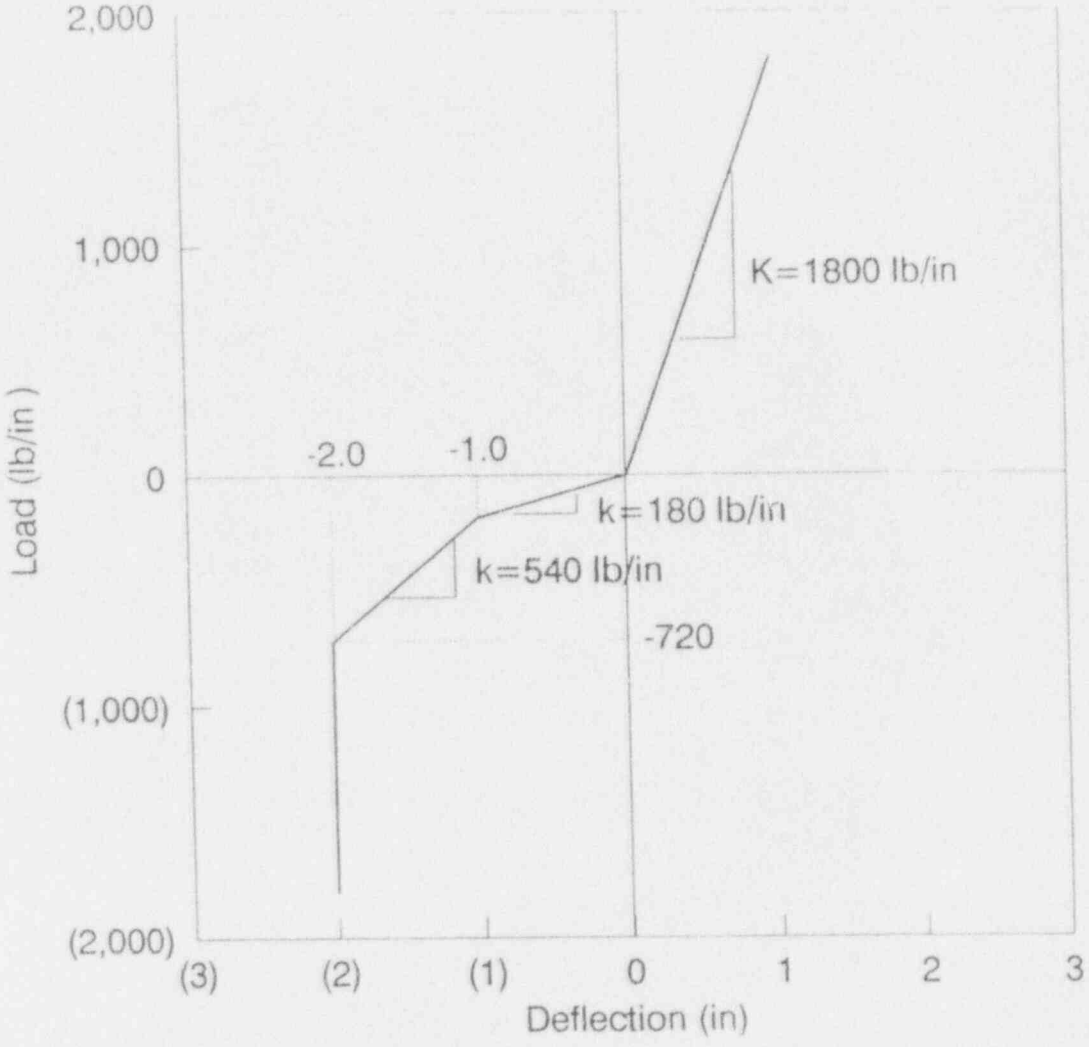

Fig 3.18 Load Deflection Curve of Springs Representing Compressible Materials

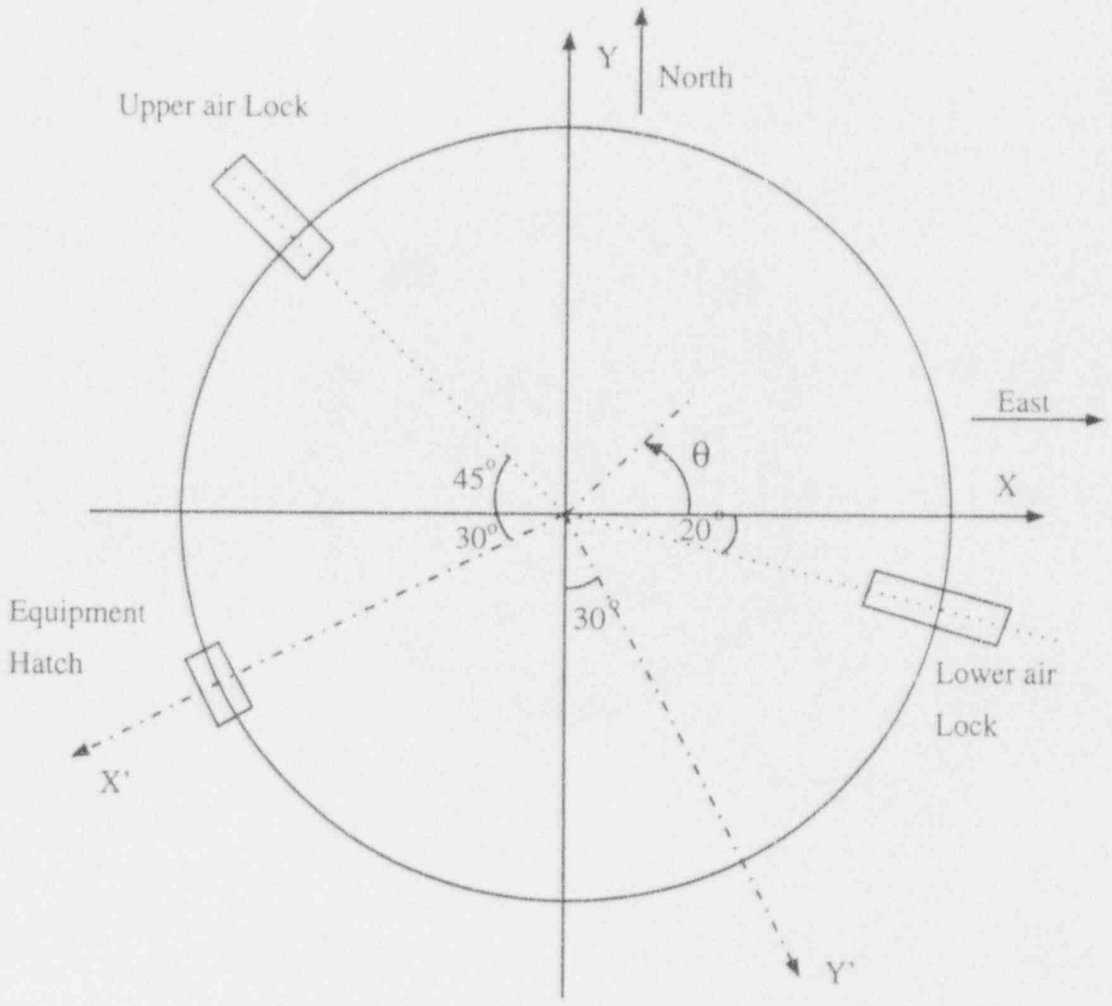

Fig. 4.1 Plan View of System 80+ Containment

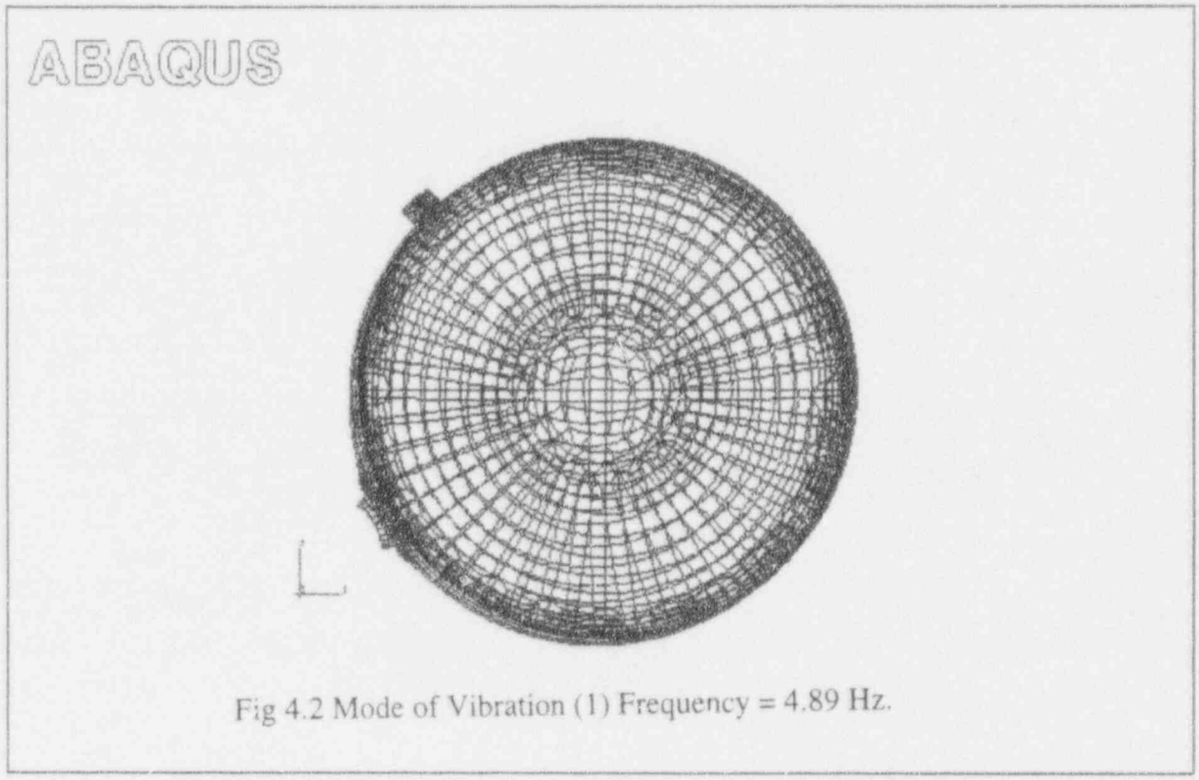

Fig 4.2 Mode of Vibration (1) Frequency = 4.89 Hz.

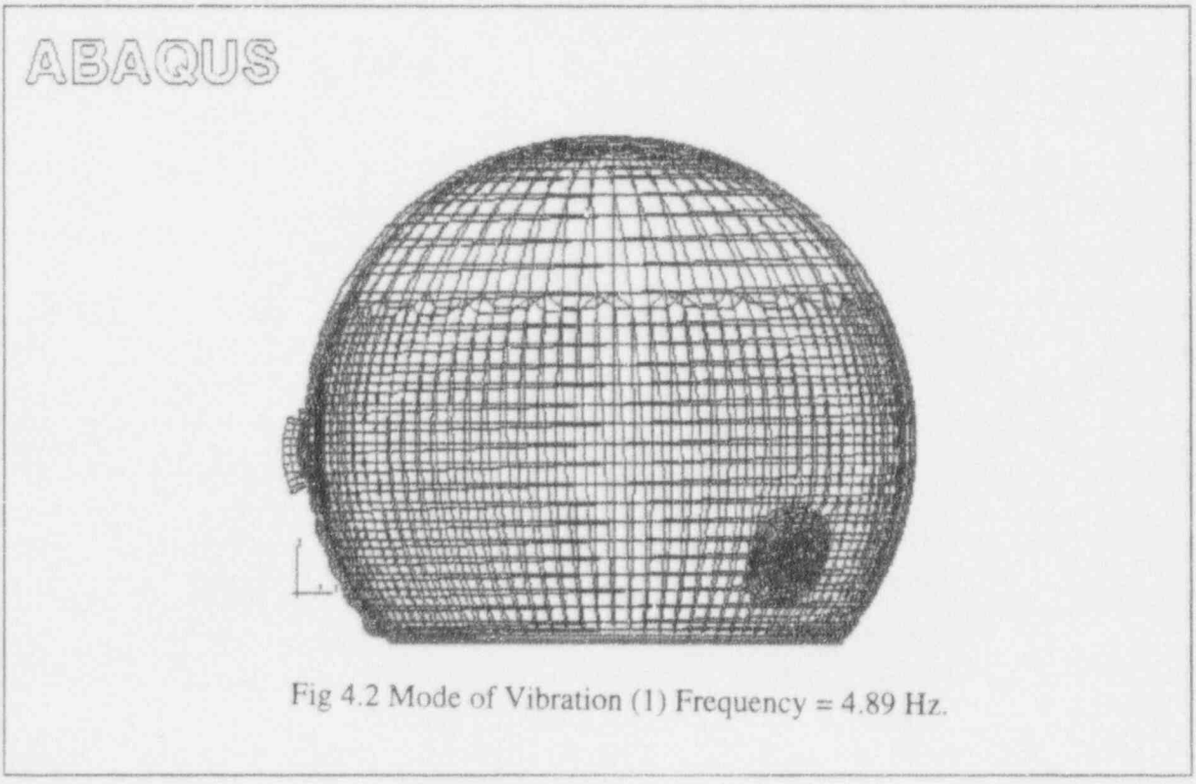

Fig 4.2 Mode of Vibration (1) Frequency = 4.89 Hz.

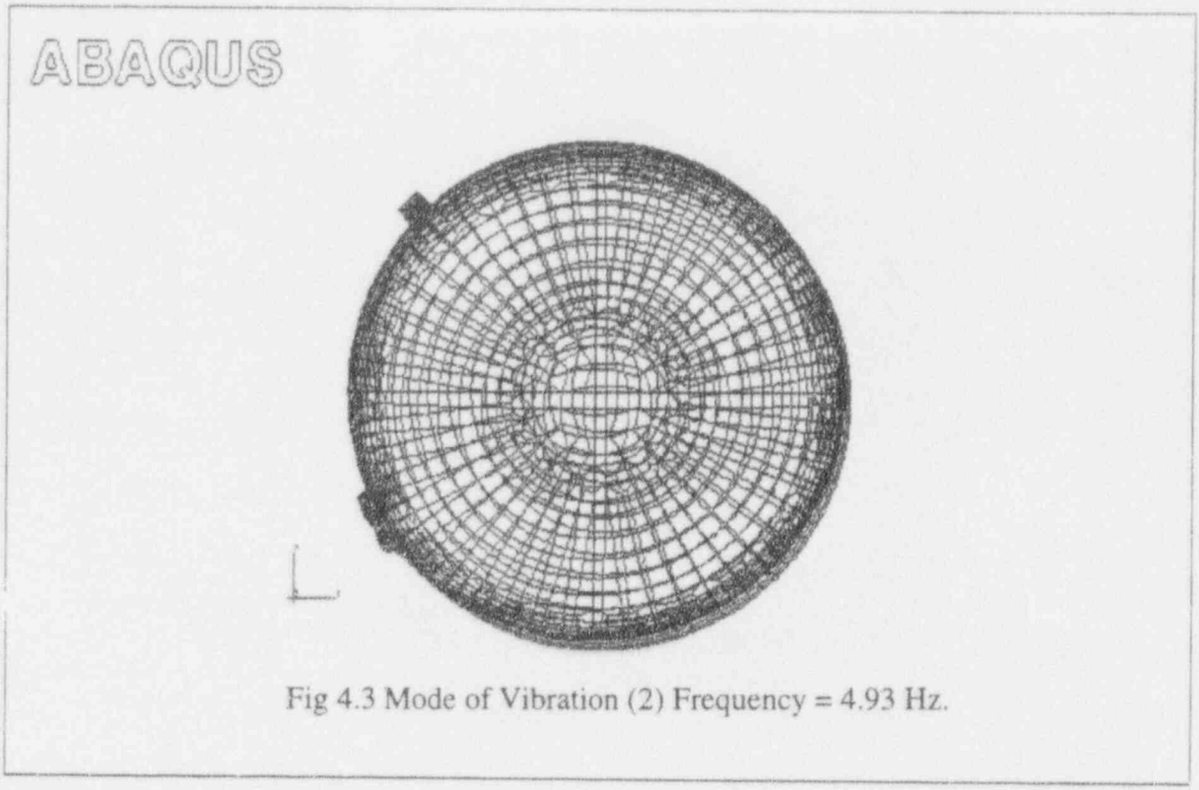

Fig 4.3 Mode of Vibration (2) Frequency = 4.93 Hz.

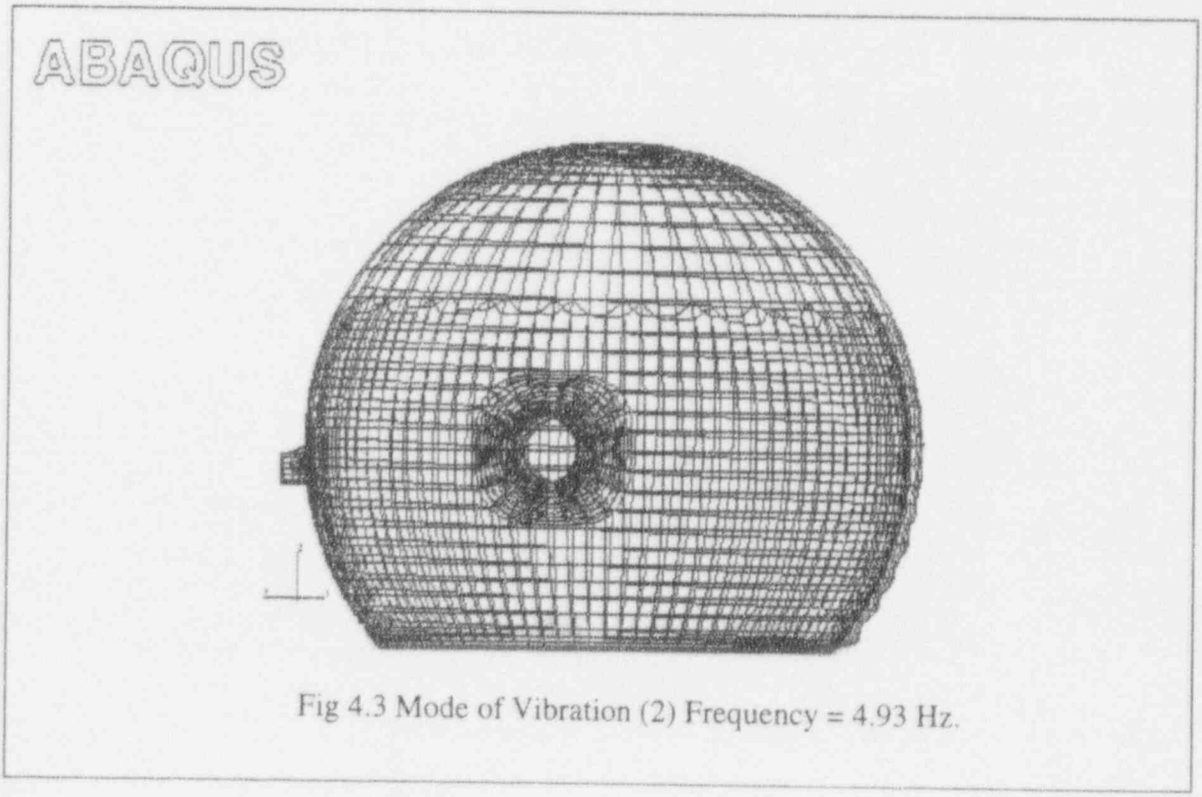

Fig 4.3 Mode of Vibration (2) Frequency = 4.93 Hz.

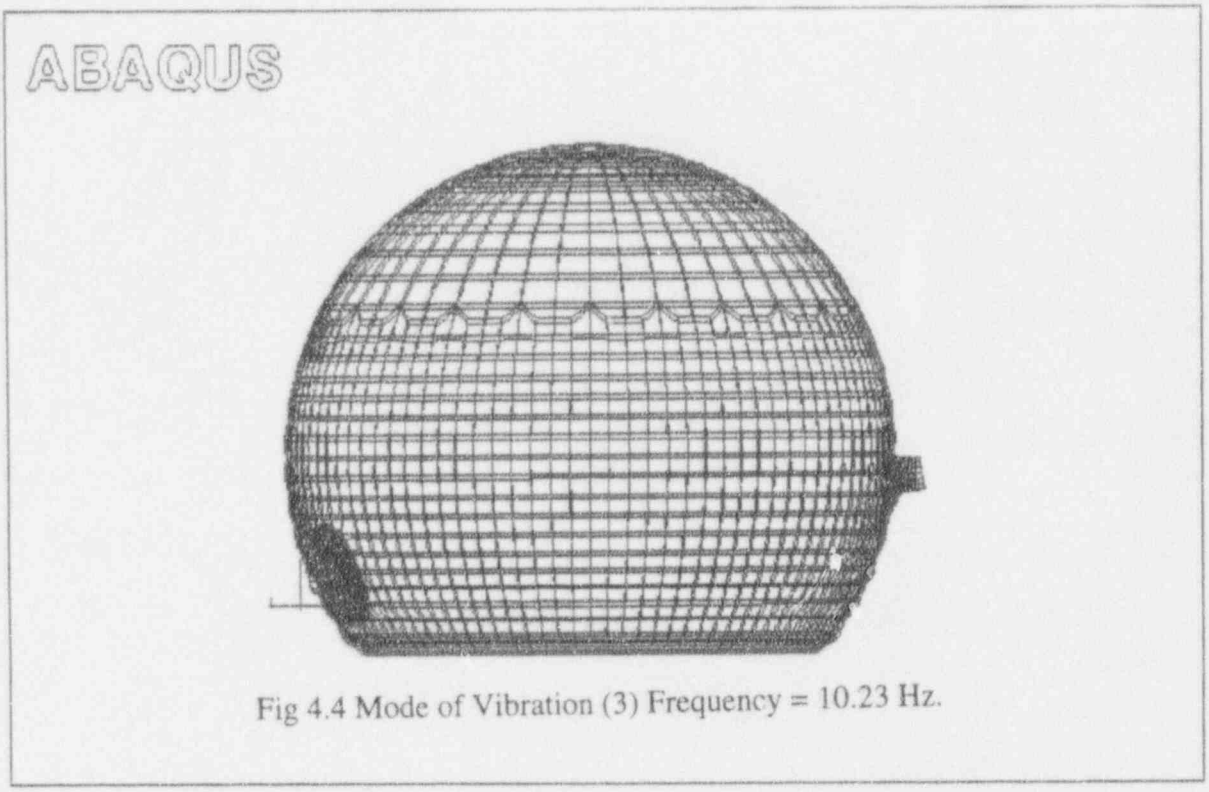

Fig 4.4 Mode of Vibration (3) Frequency = 10.23 Hz.

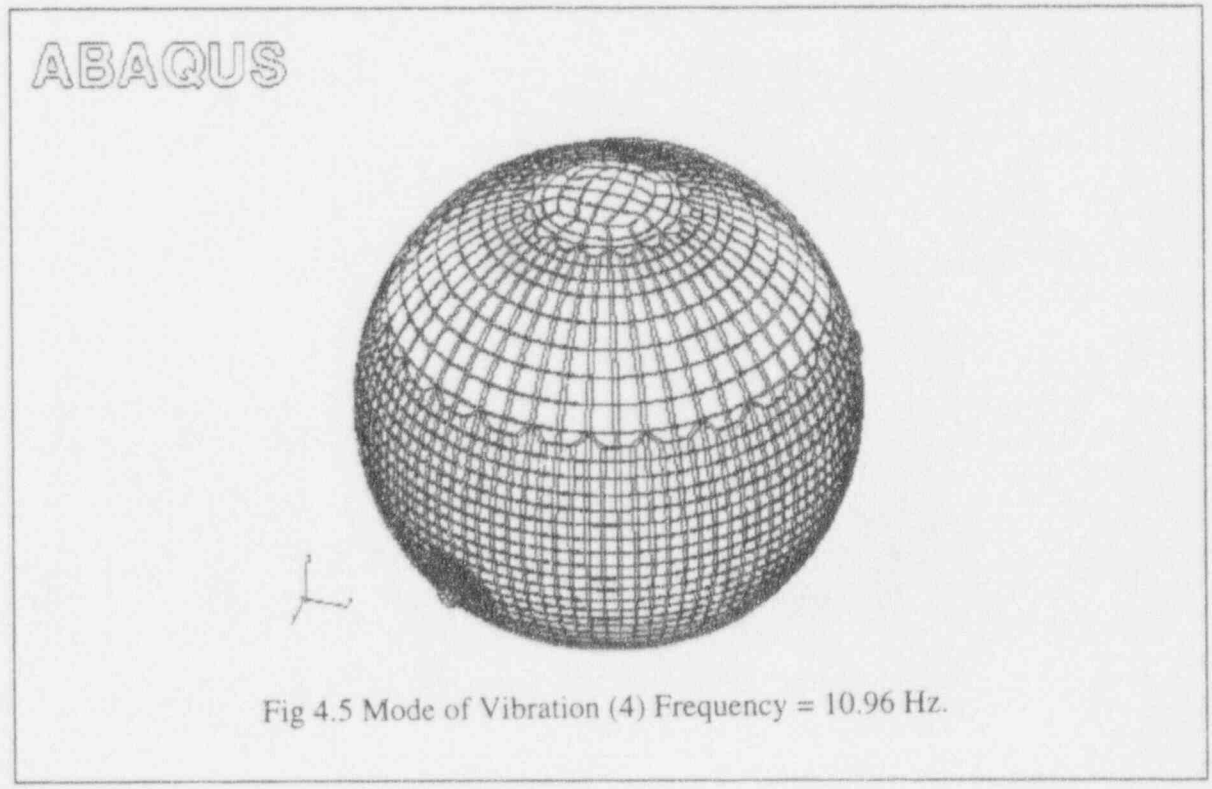

Fig 4.5 Mode of Vibration (4) Frequency = 10.96 Hz.

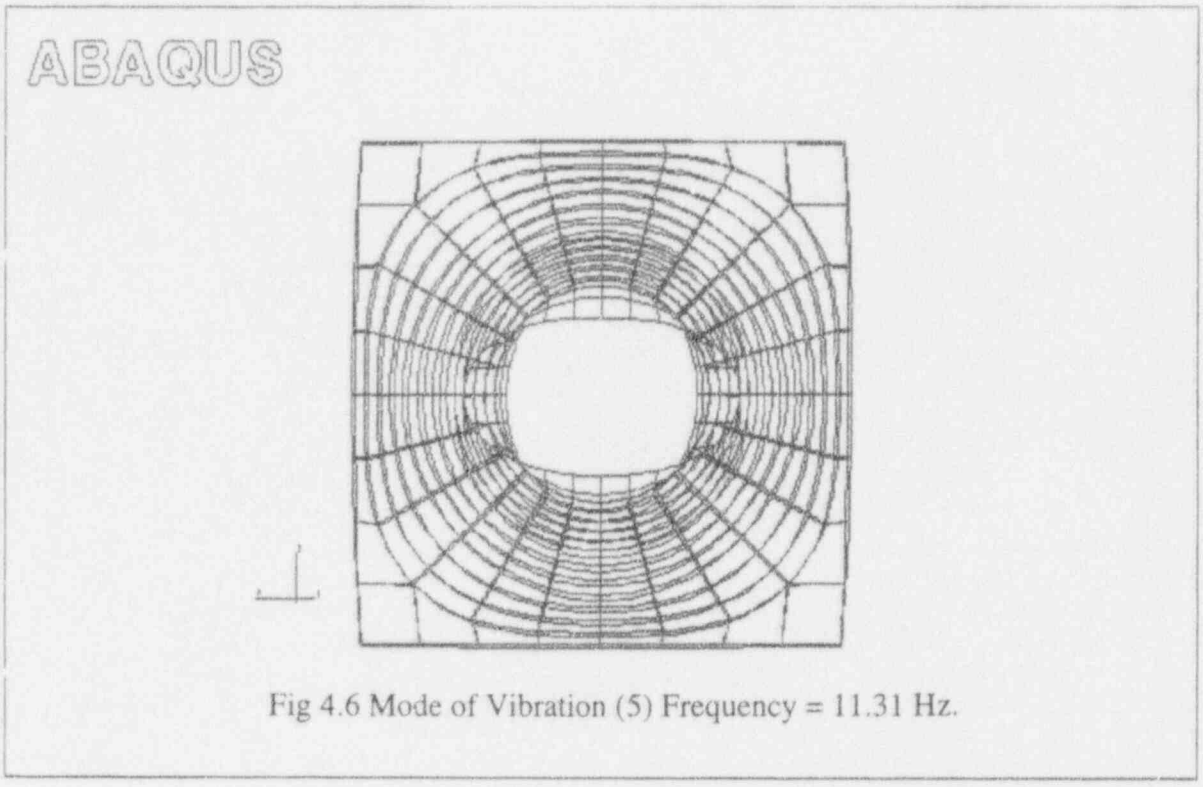

Fig 4.6 Mode of Vibration (5) Frequency = 11.31 Hz.

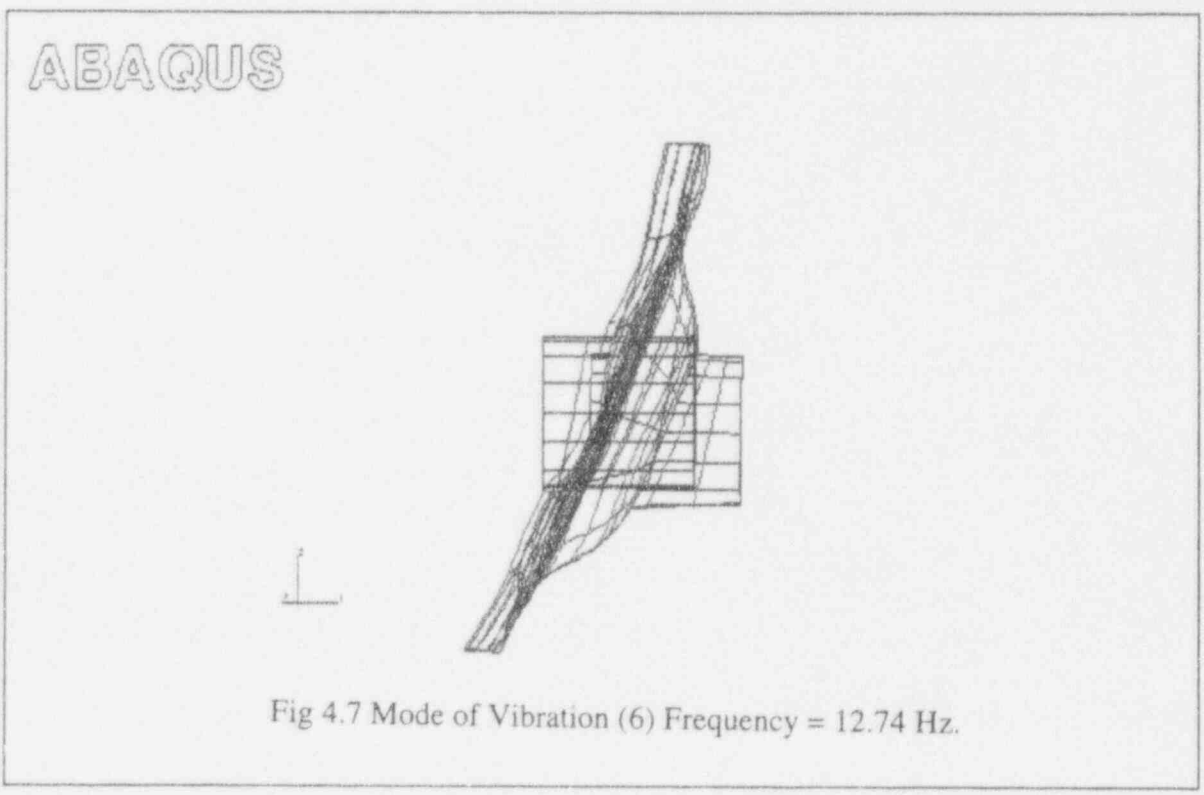

Fig 4.7 Mode of Vibration (6) Frequency = 12.74 Hz.

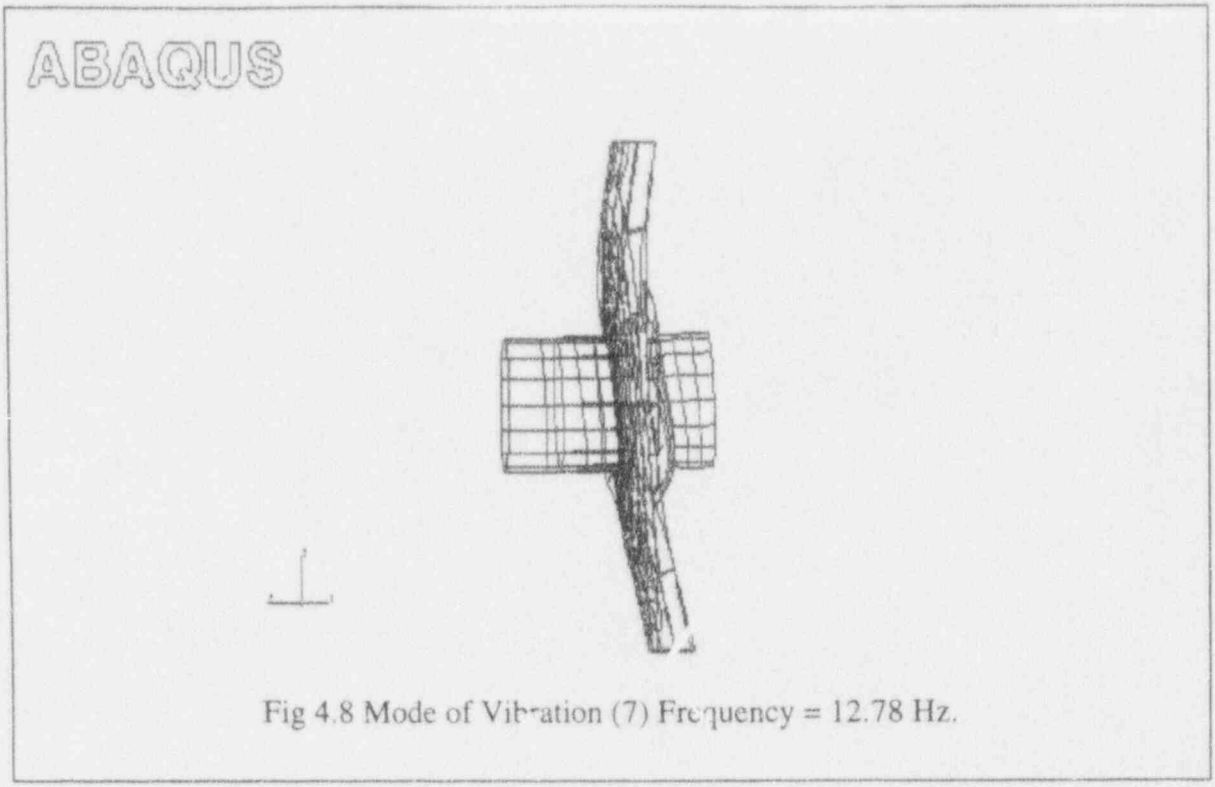

Fig 4.8 Mode of Vibration (7) Frequency = 12.78 Hz.

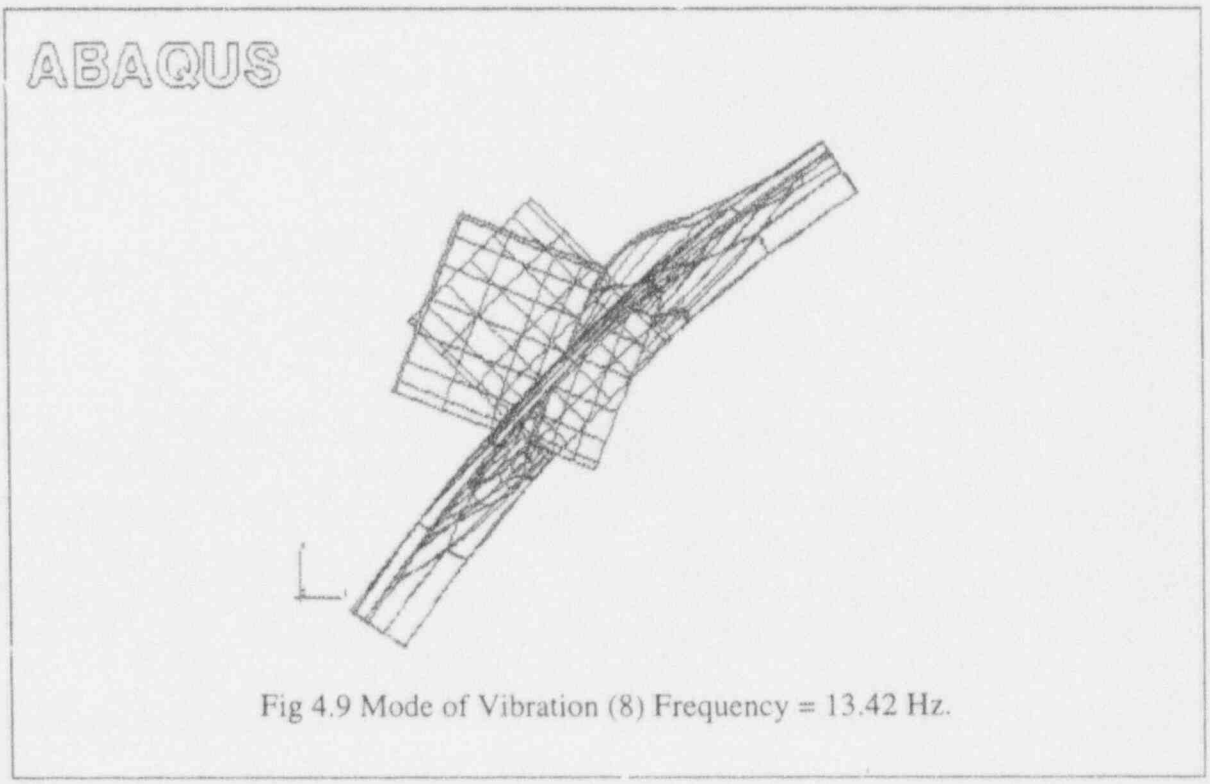

Fig 4.9 Mode of Vibration (8) Frequency = 13.42 Hz.

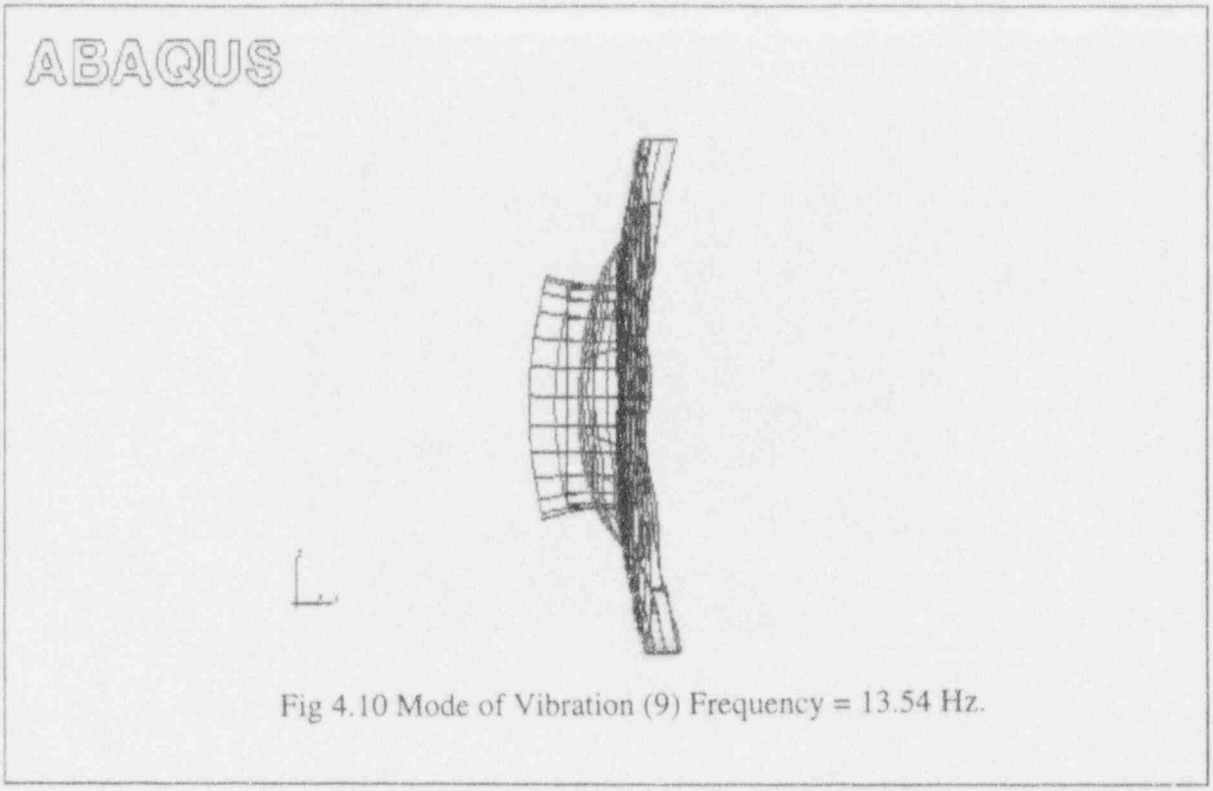

Fig 4.10 Mode of Vibration (9) Frequency = 13.54 Hz.

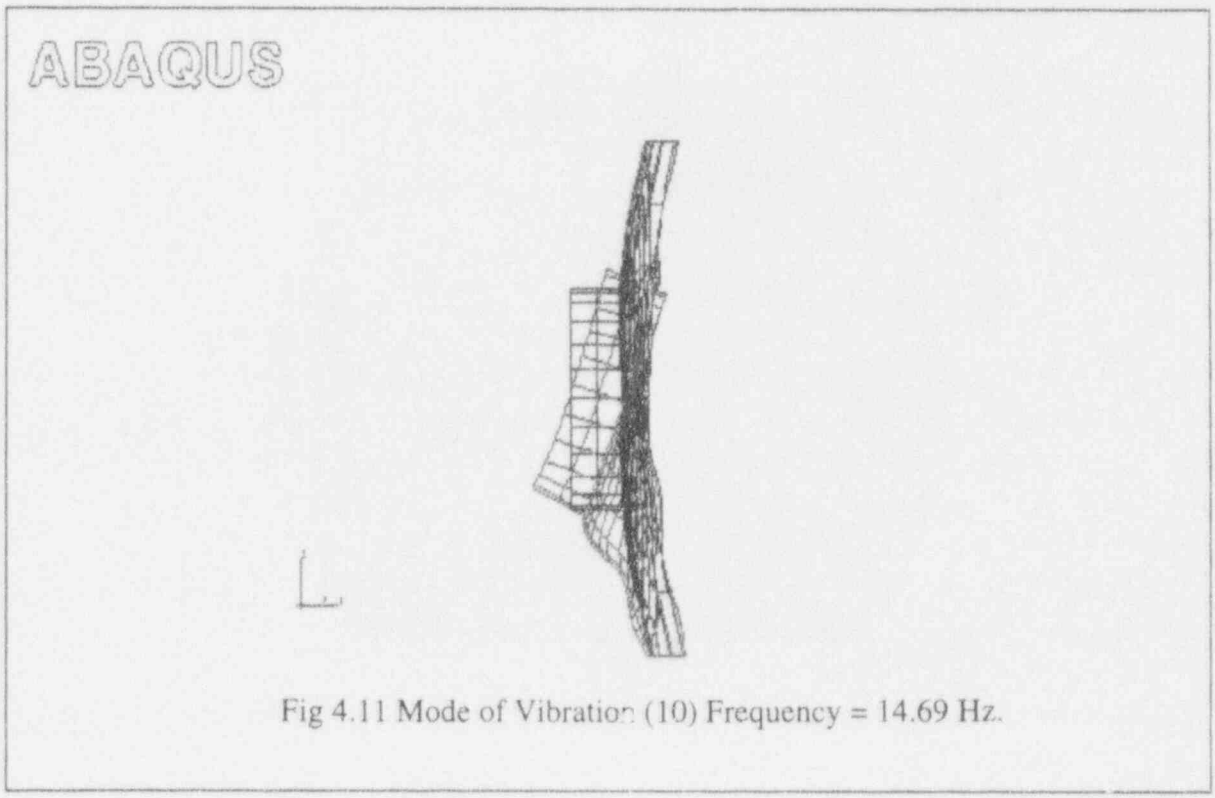

Fig 4.11 Mode of Vibration (10) Frequency = 14.69 Hz.

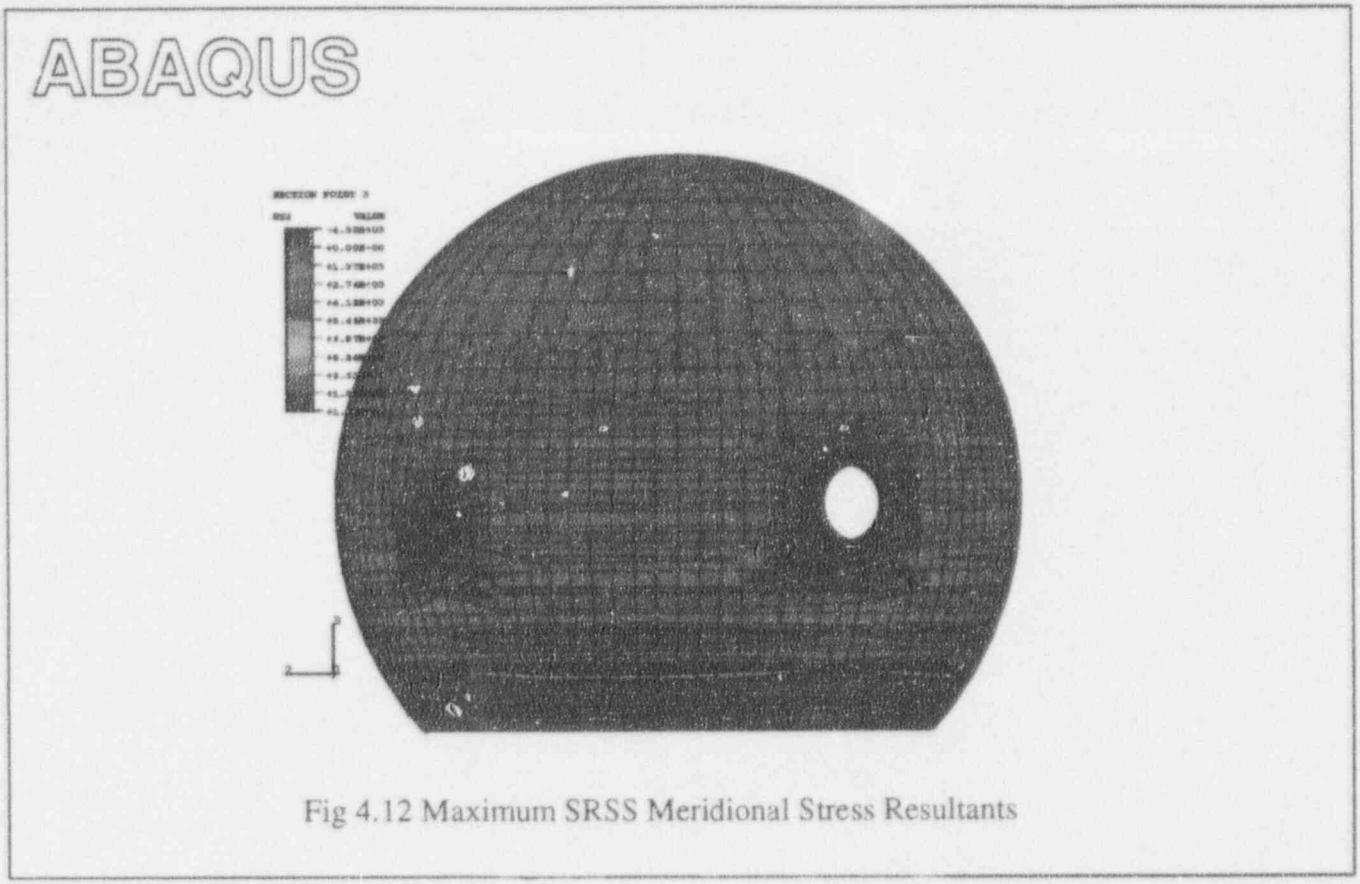

Fig 4.12 Maximum SRSS Meridional Stress Resultants

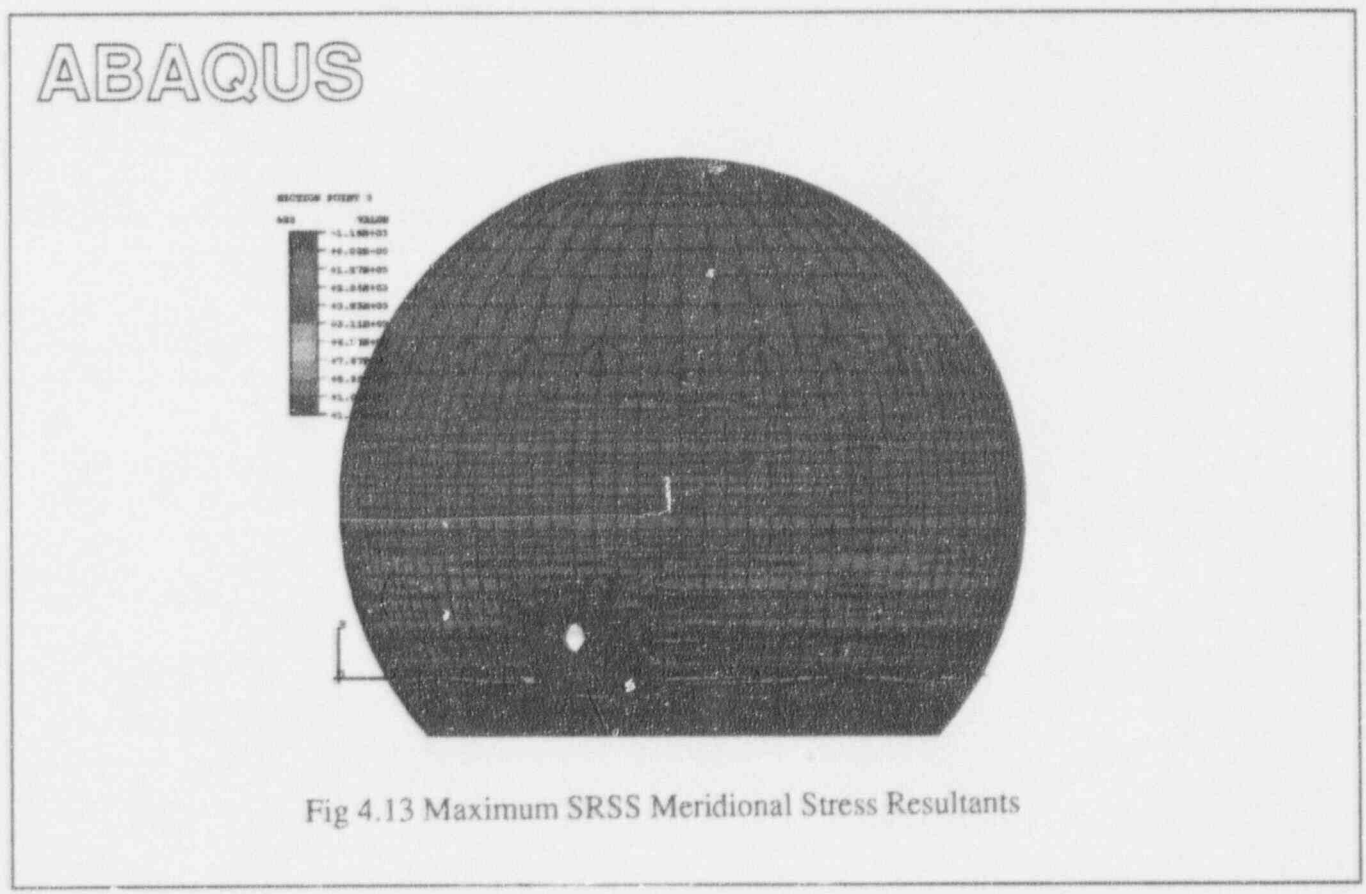

Fig 4.13 Maximum SRSS Meridional Stress Resultants

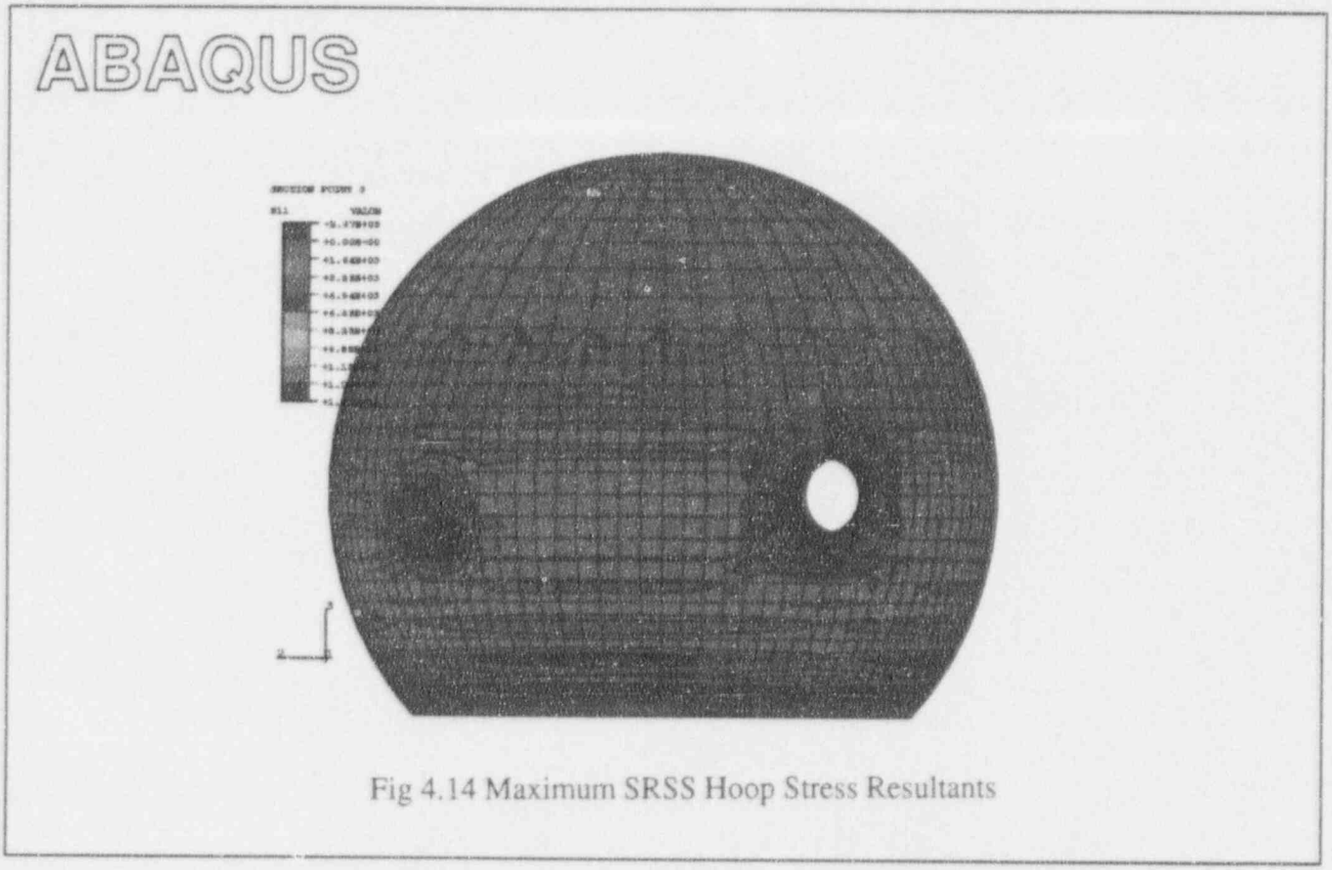

Fig 4.14 Maximum SRSS Hoop Stress Resultants

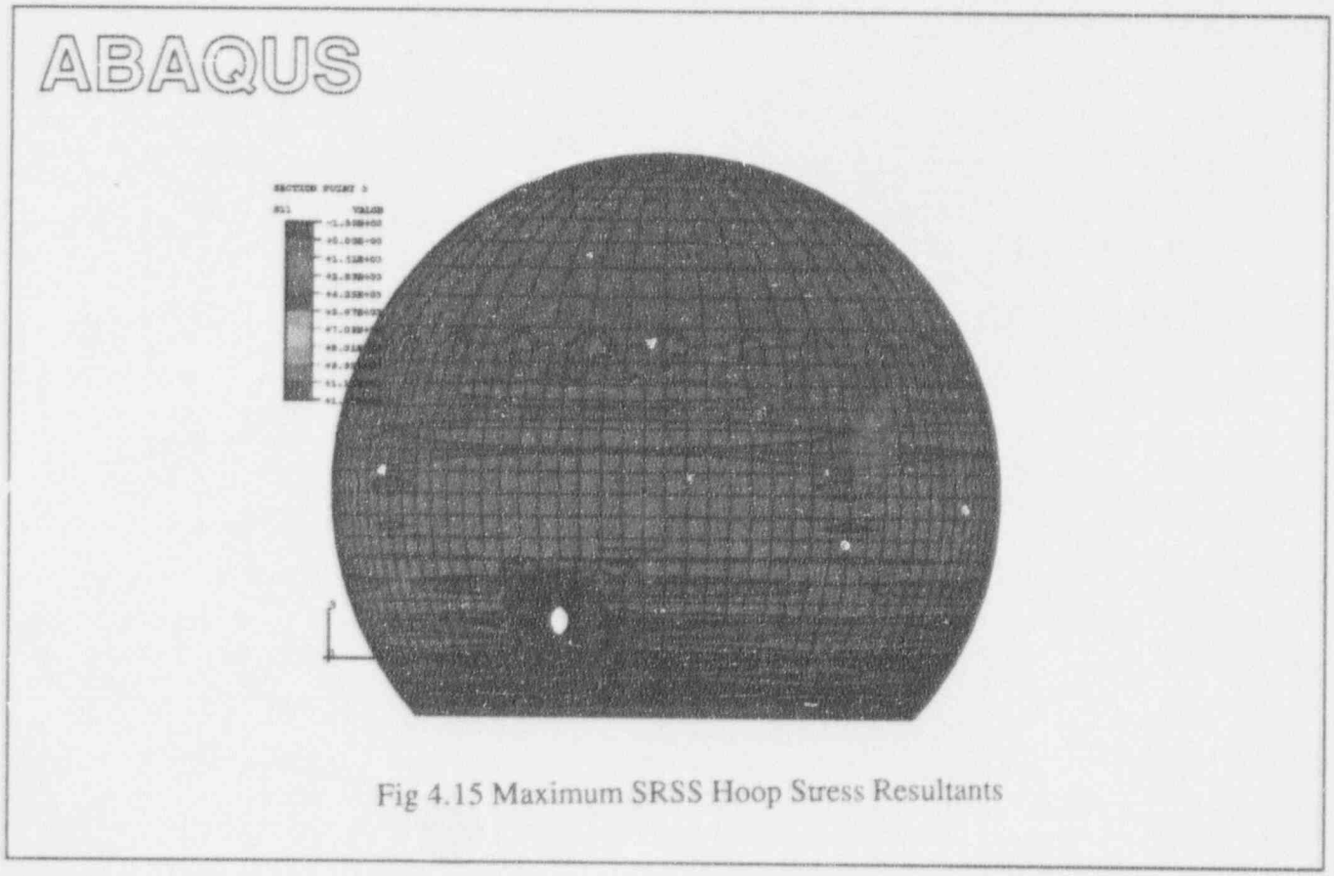

Fig 4.15 Maximum SRSS Hoop Stress Resultants

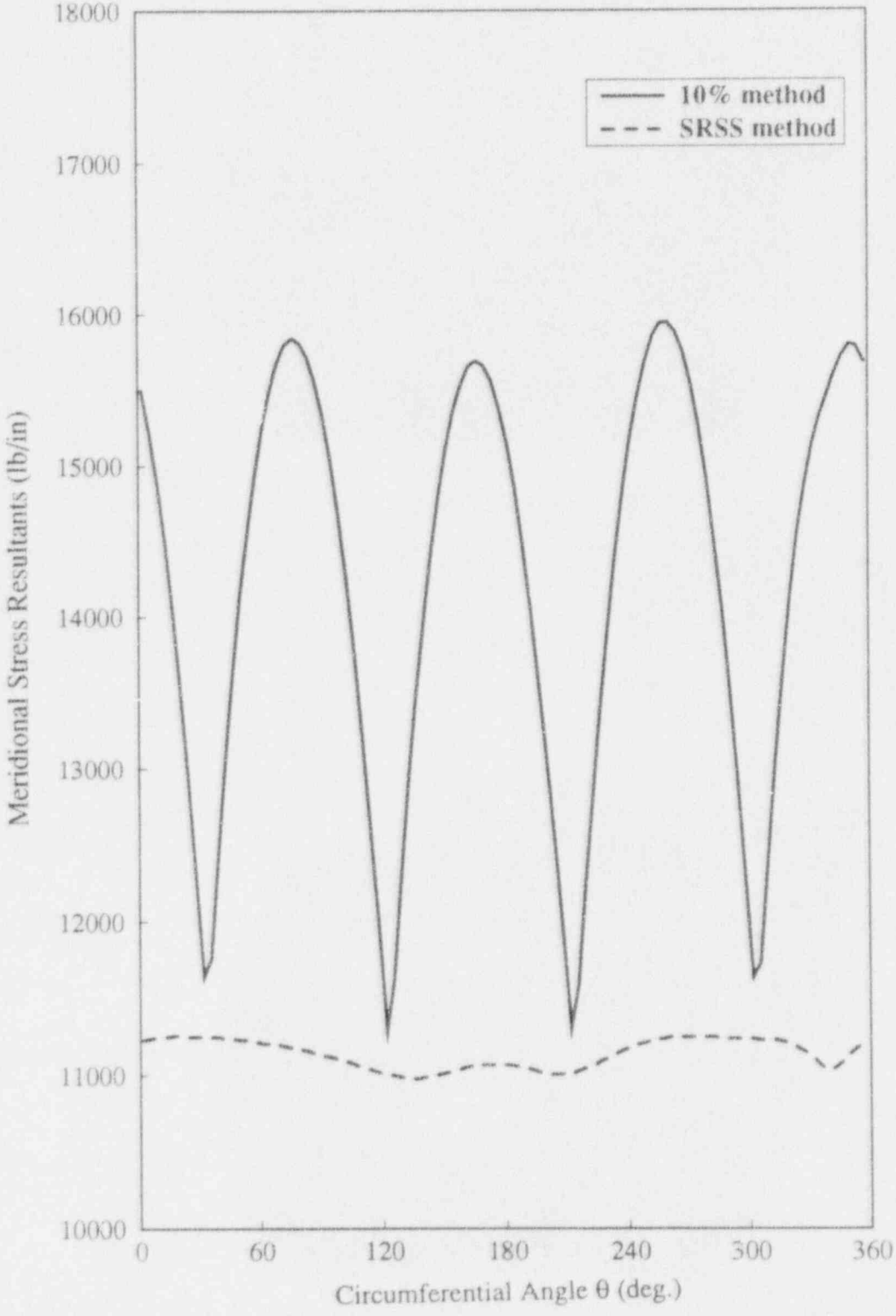

Fig 4.16 Maximum SRSS Meridional Stress Resultants at Support

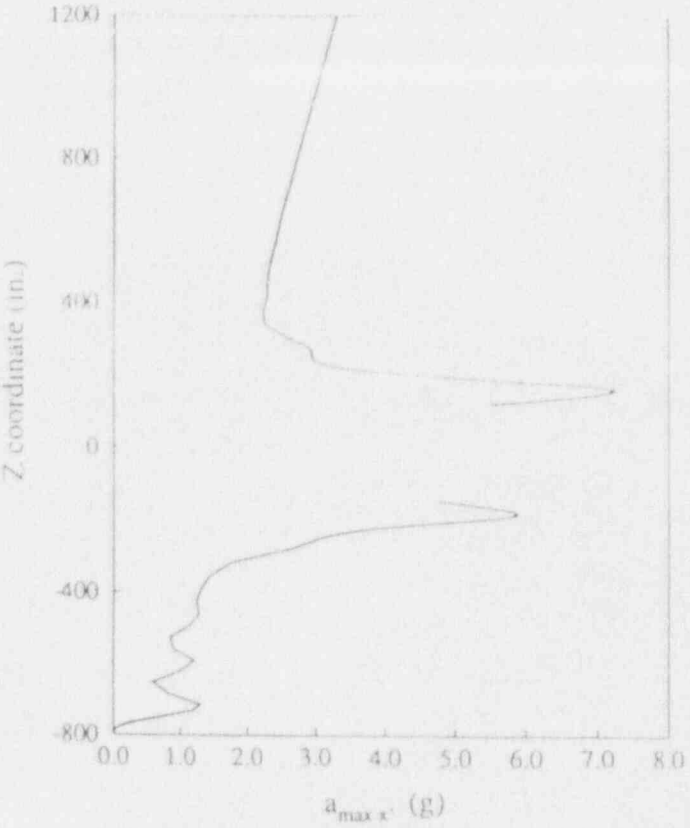

Fig 4.17 Variation of Maximum SRSS $a_{x'}$ along the Equipment Hatch Meridian (θ=210°)

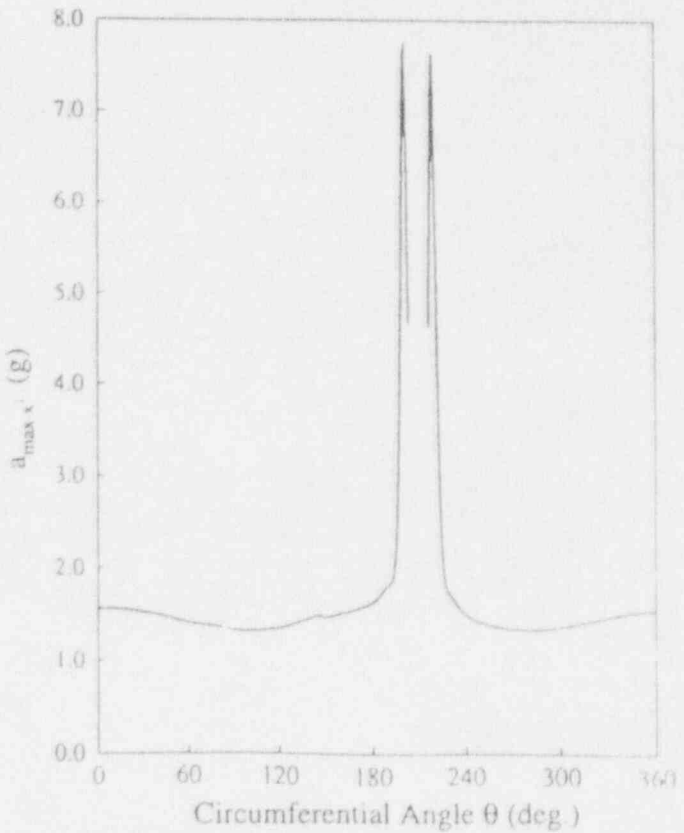

Fig 4.18 Variation of Maximum SRSS $a_{x'}$ along the Equator (Elev. = 156 ft.)

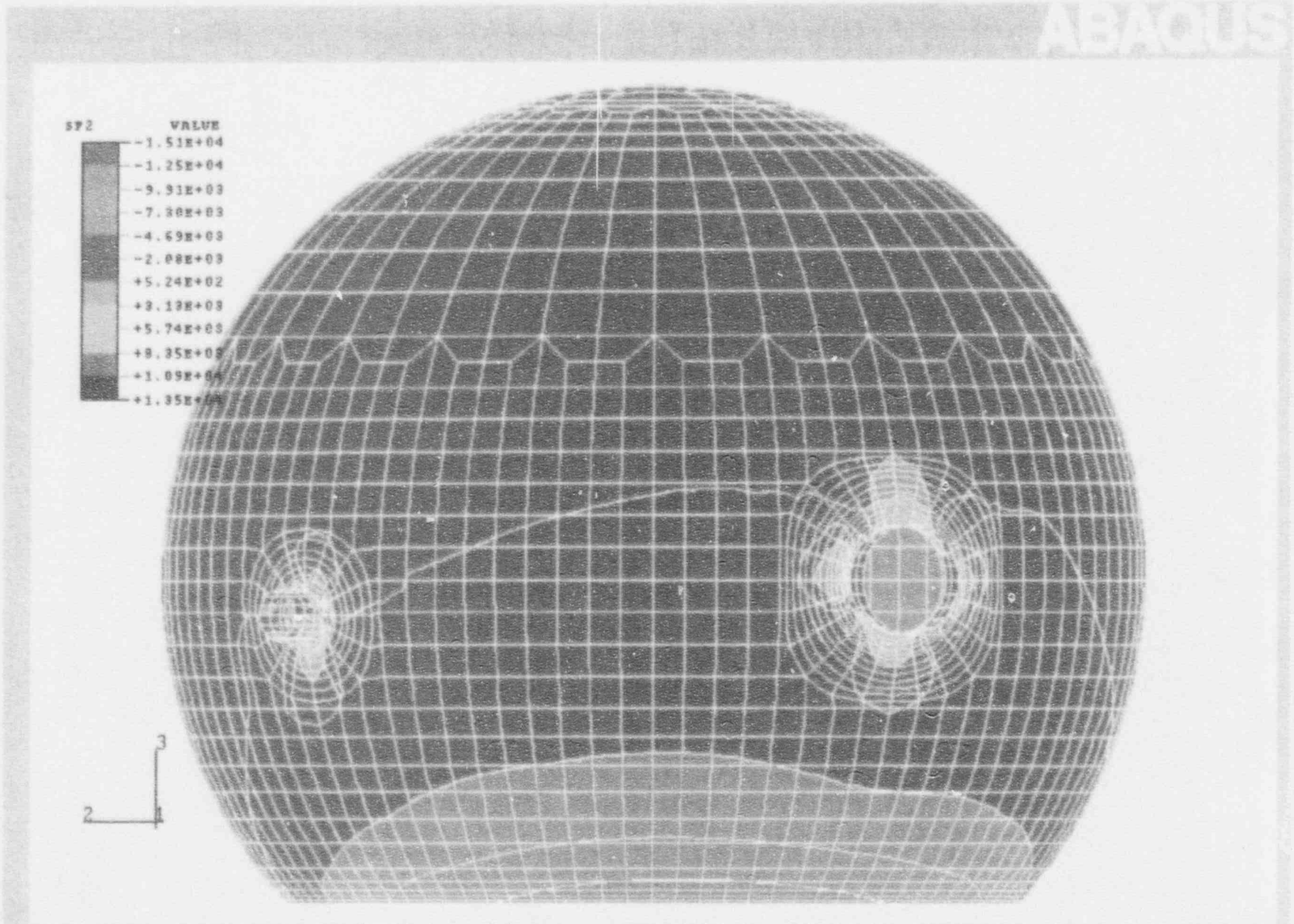

Fig 4.19 Meridional Stress Resultants

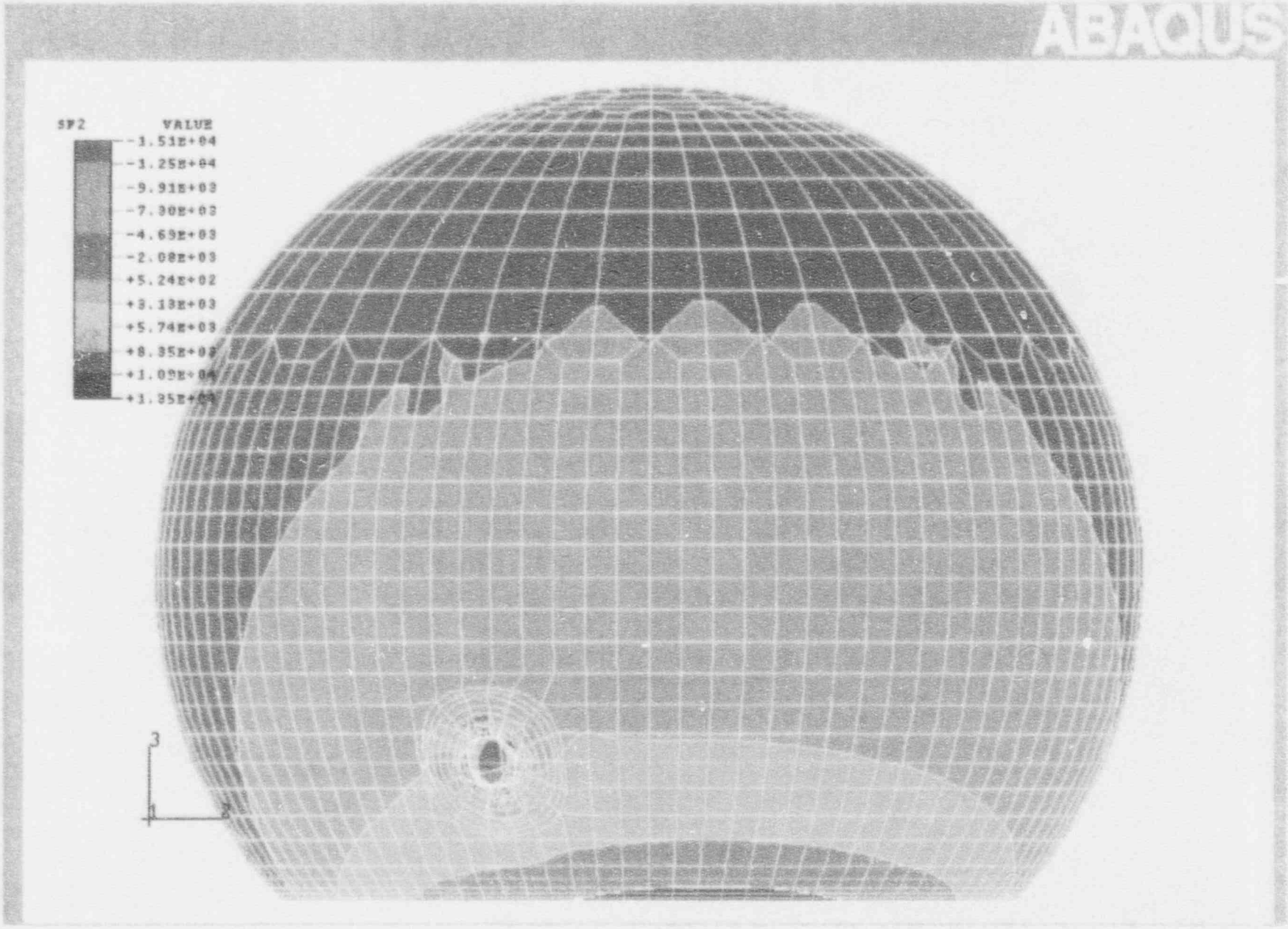

Fig 4.20 Meridional Stress Resultants

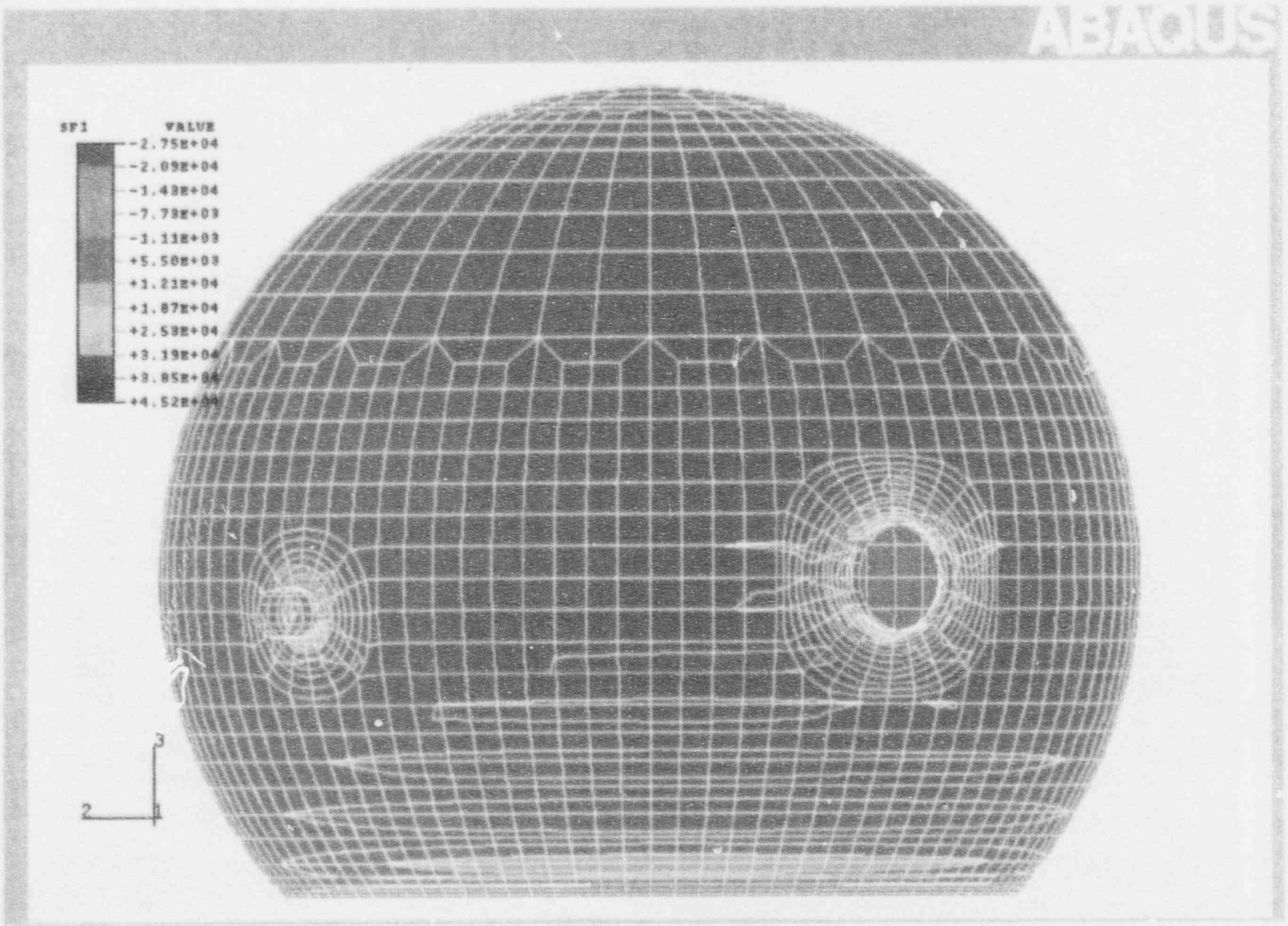

Fig 4.21 Hoop Stress Resultants

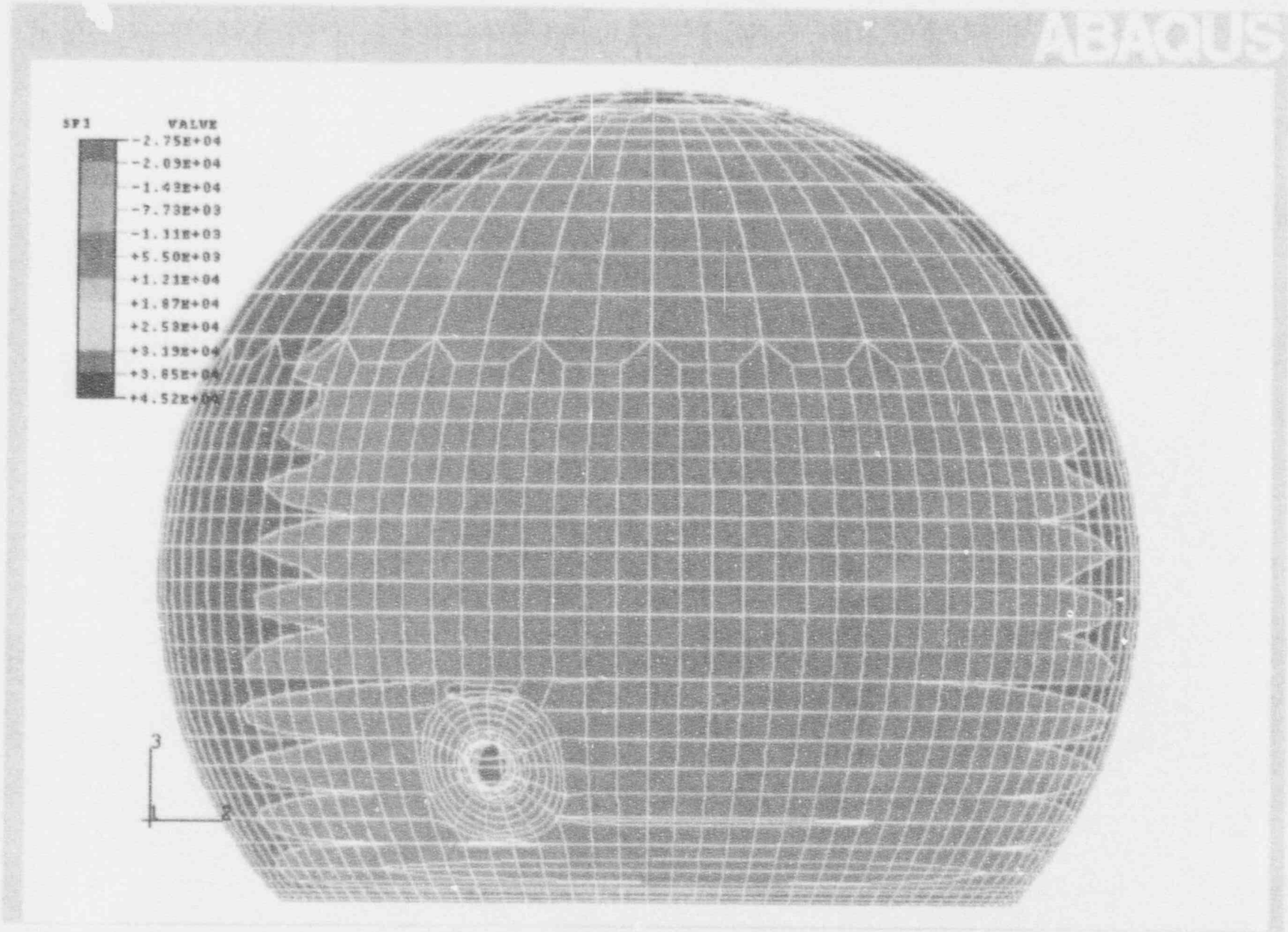

Fig 4.22 Hoop Stress Resultants

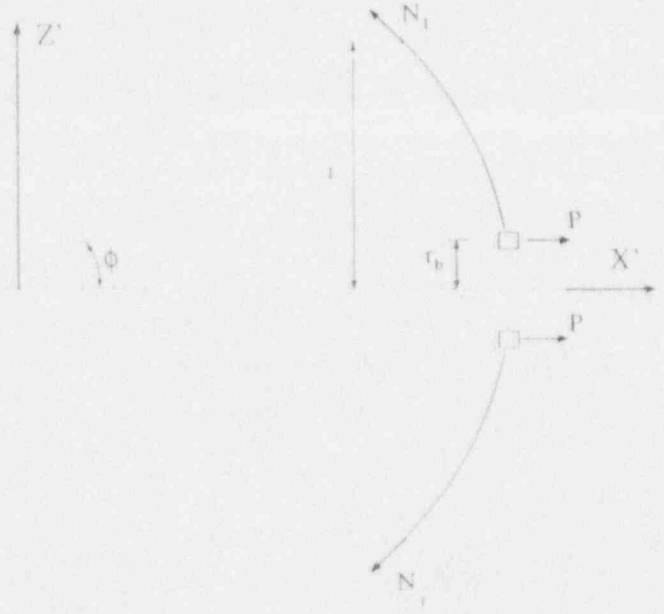

Fig 4.23 Reinforced Opening with Ring Load

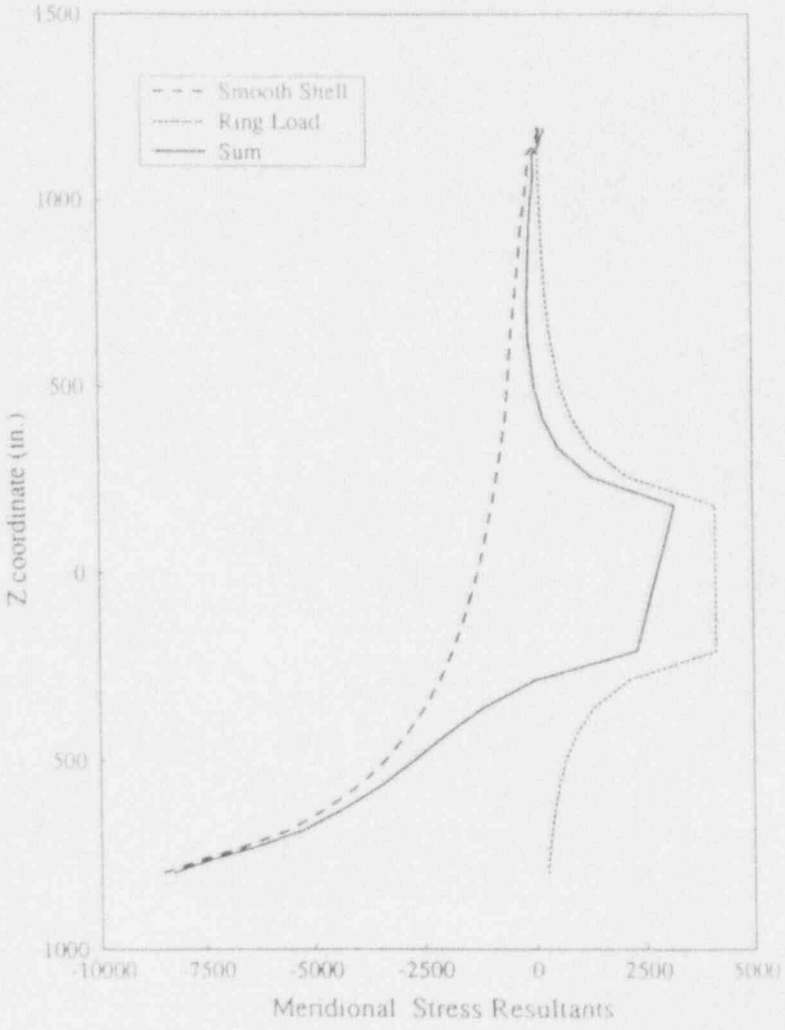

Fig 4.24 Meridional Stress Resultants along Equipment Hatch Meridian

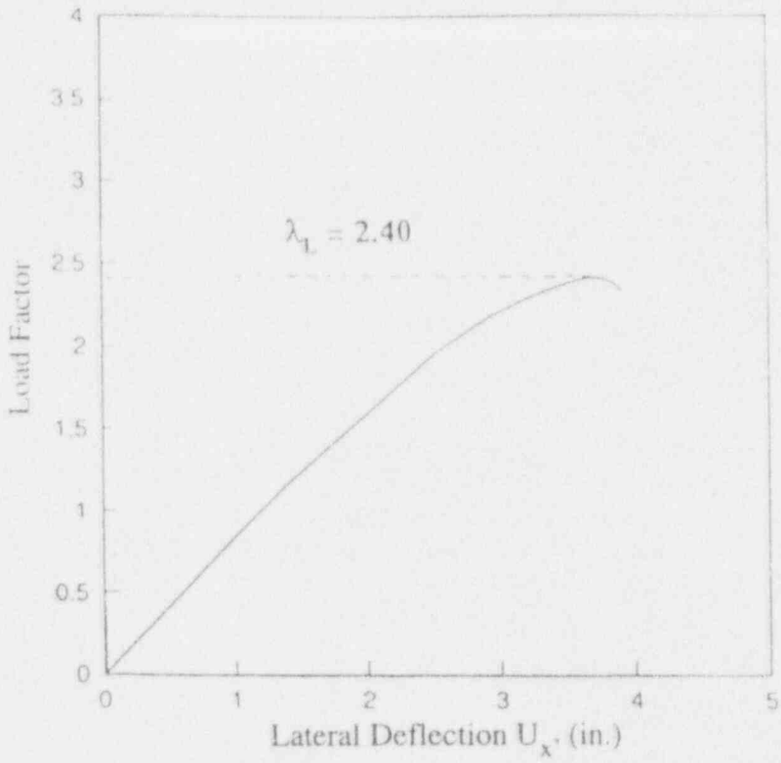

Fig 4.25 Load Deflection at the Top.

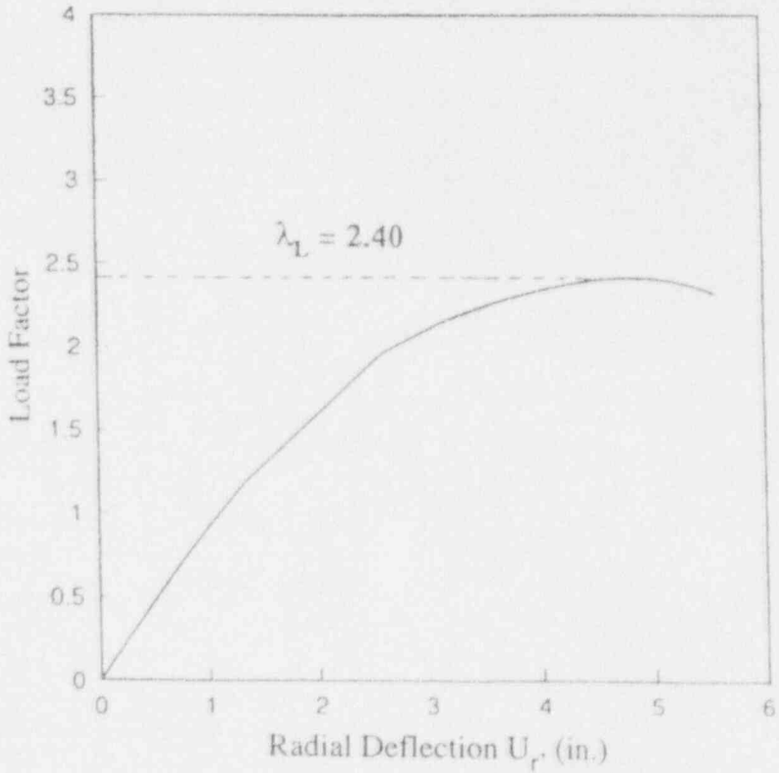

Fig 4.26 Load Deflection at the Base.

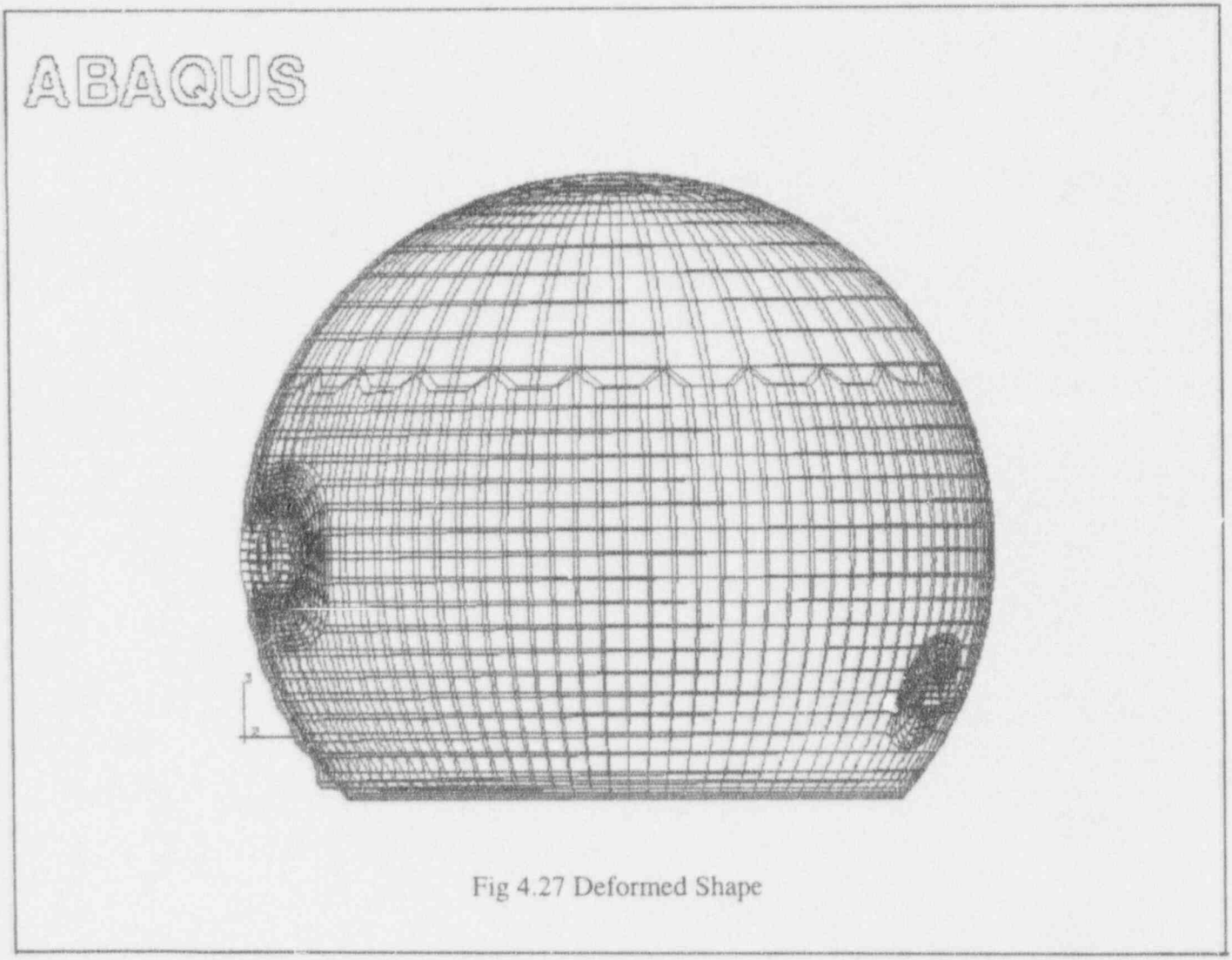

Fig 4.27 Deformed Shape

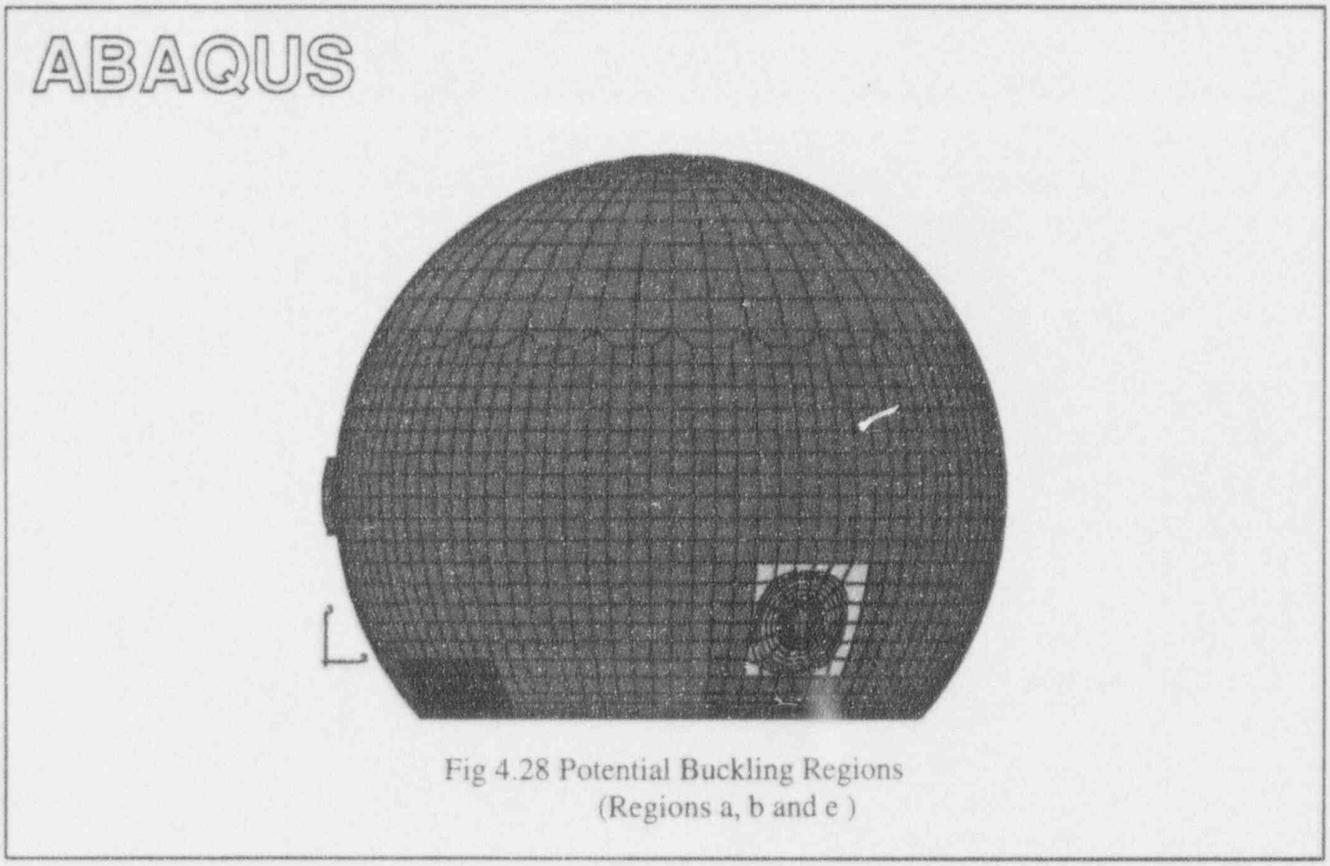

Fig 4.28 Potential Buckling Regions
(Regions a, b and e)

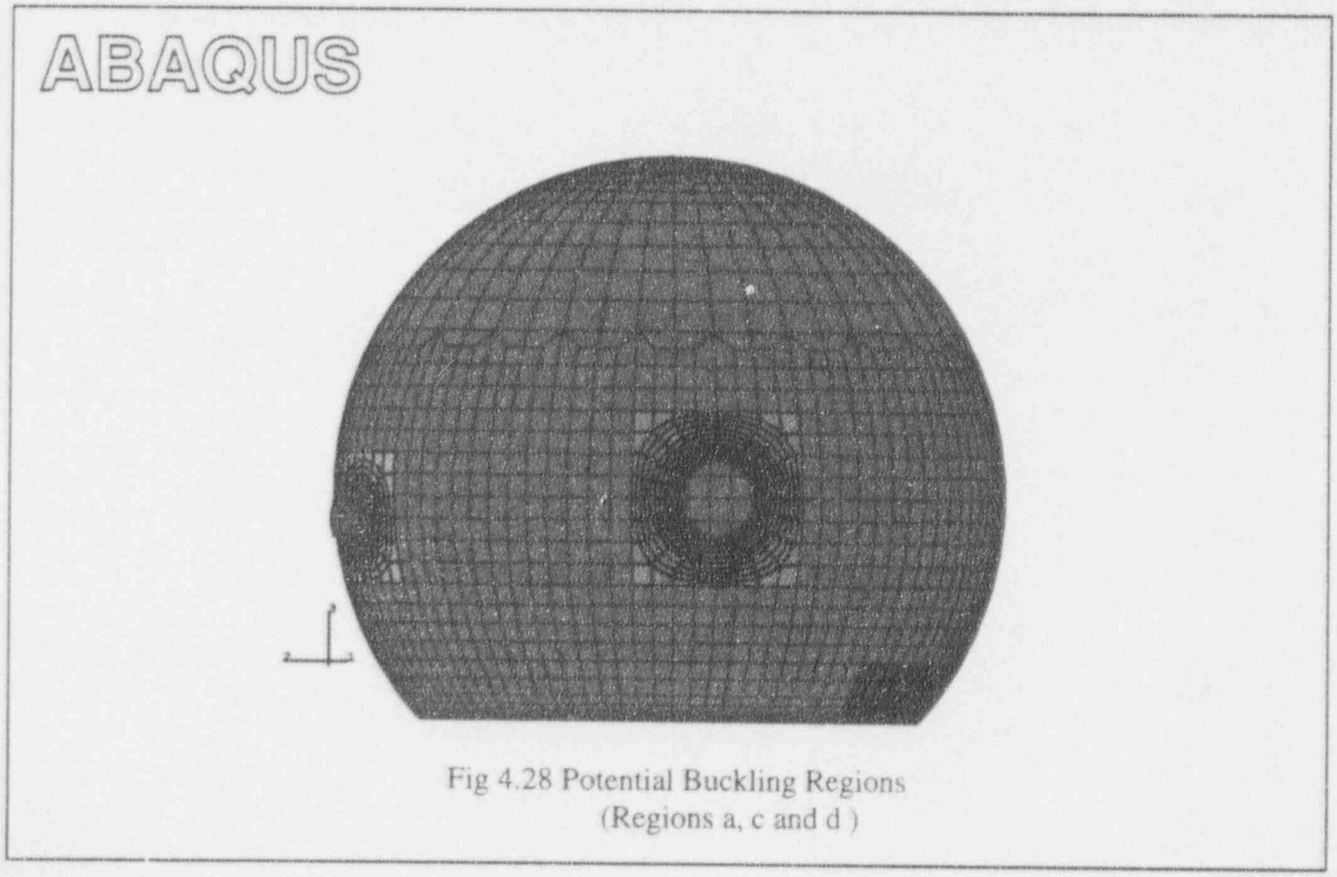

Fig 4.28 Potential Buckling Regions
(Regions a, c and d)

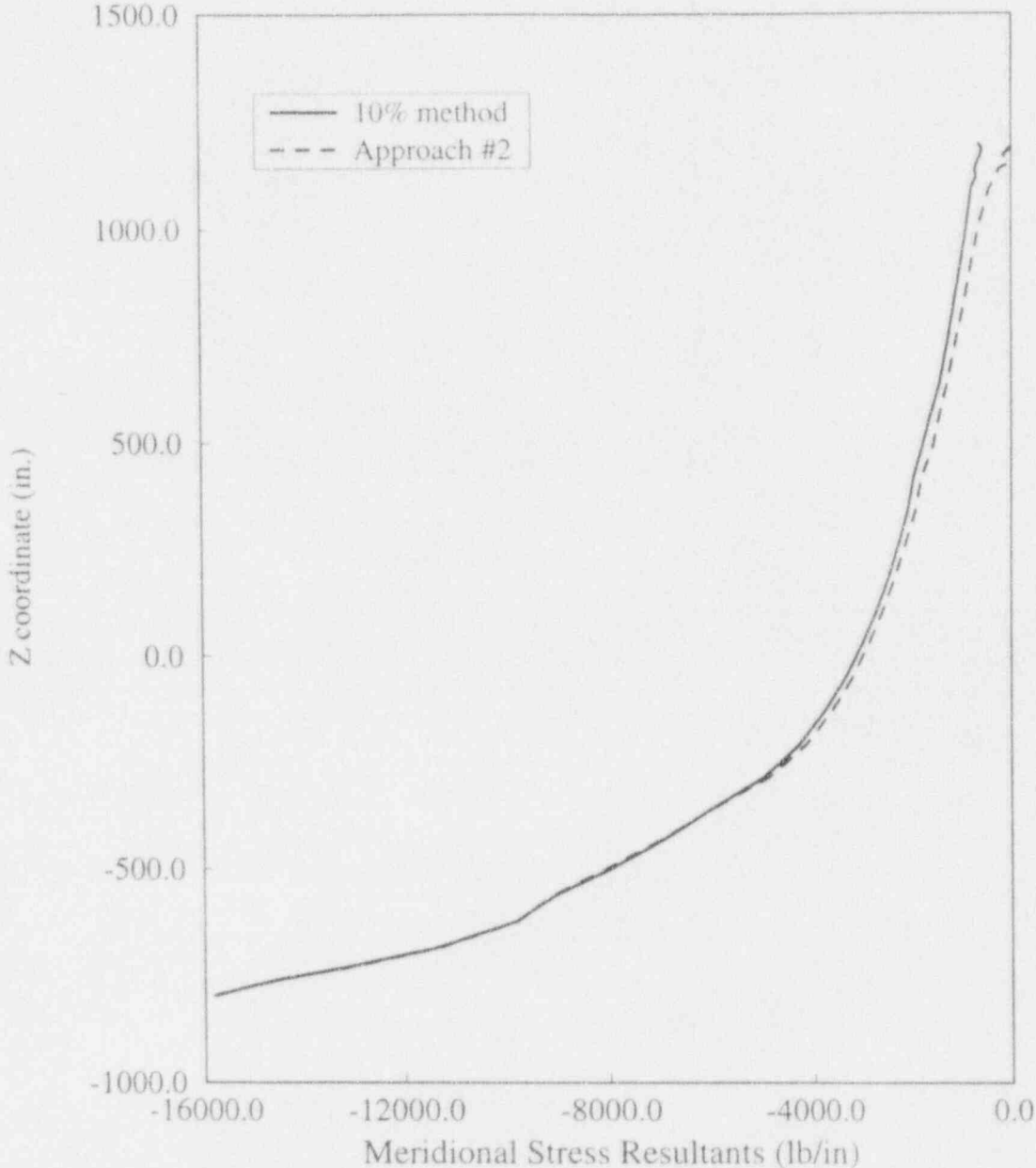

Fig 4.29 Comparison of Stress Field and Maximum SRSS Stresses (Load Case 1)

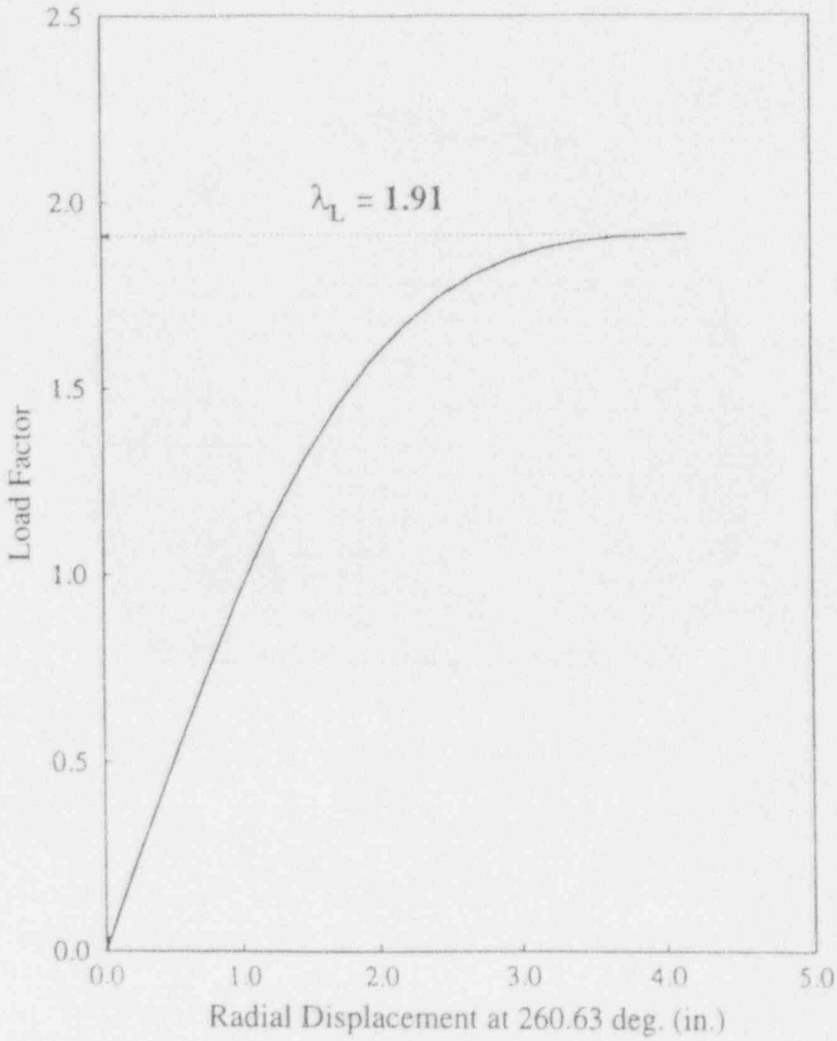

Fig 4.30 Load Deflection at the Base (Load Case 1)

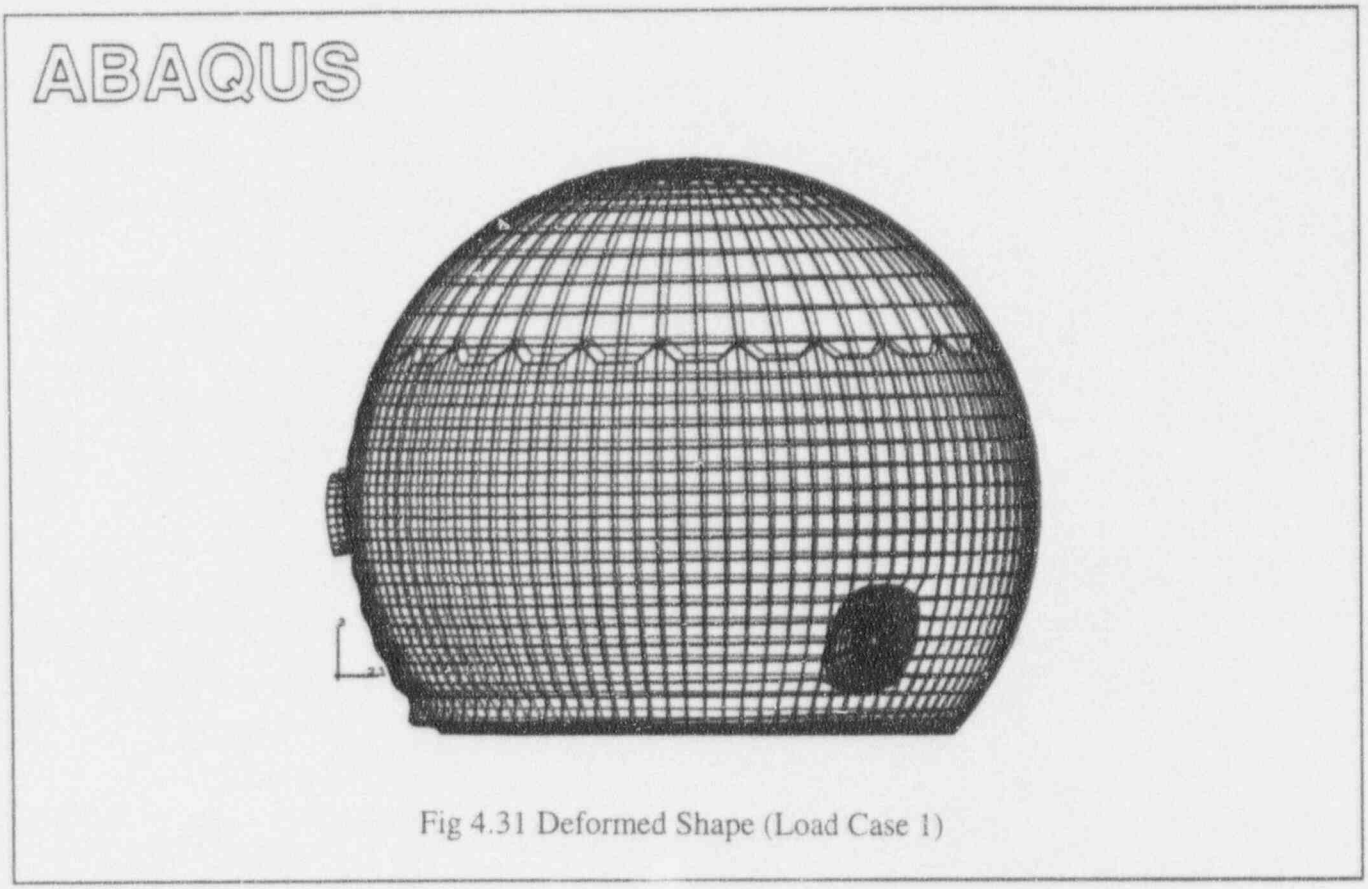

Fig 4.31 Deformed Shape (Load Case 1)

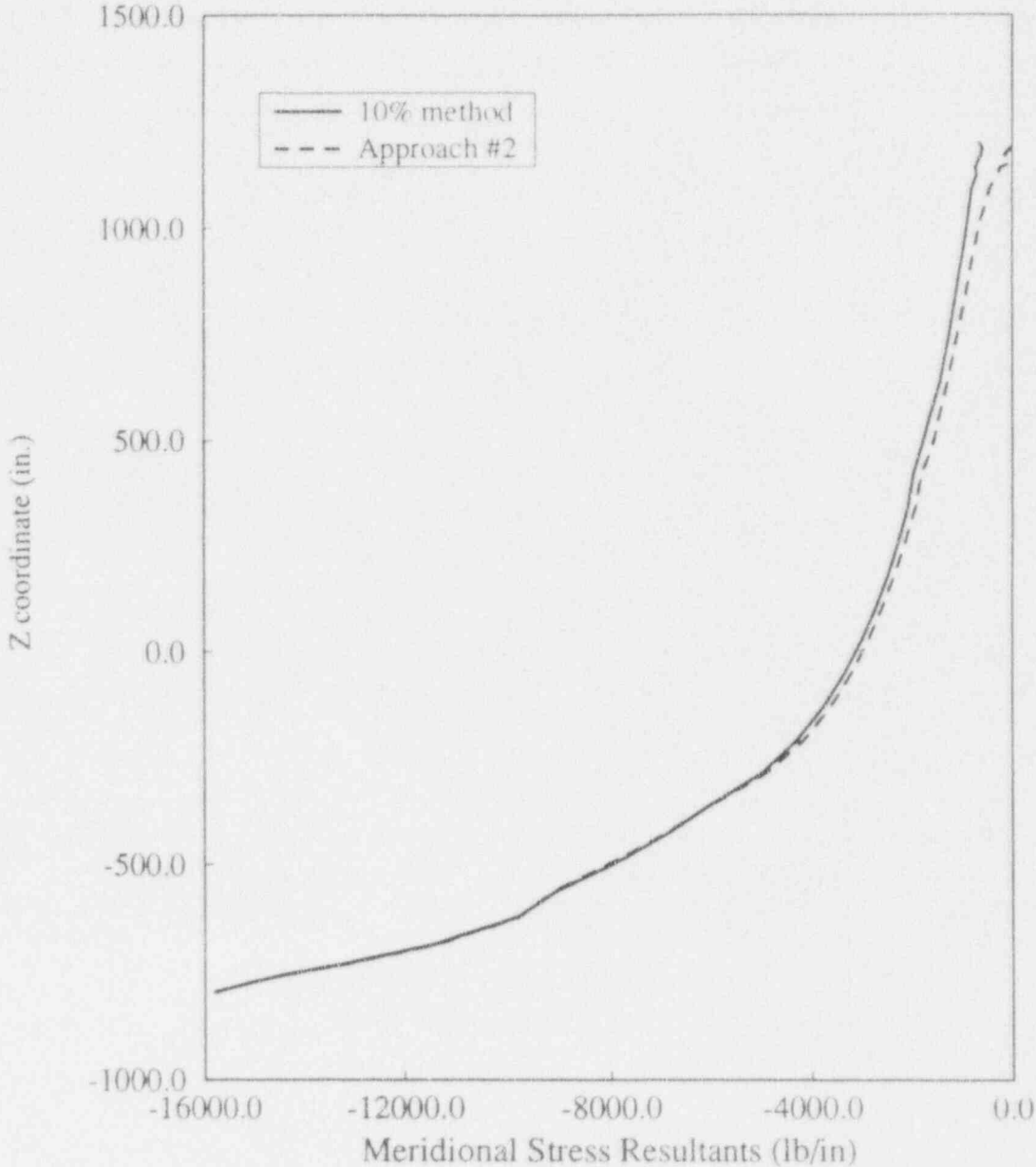

Fig 4.32 Meridional Stress Resultants along the 352.5^{o} meridian

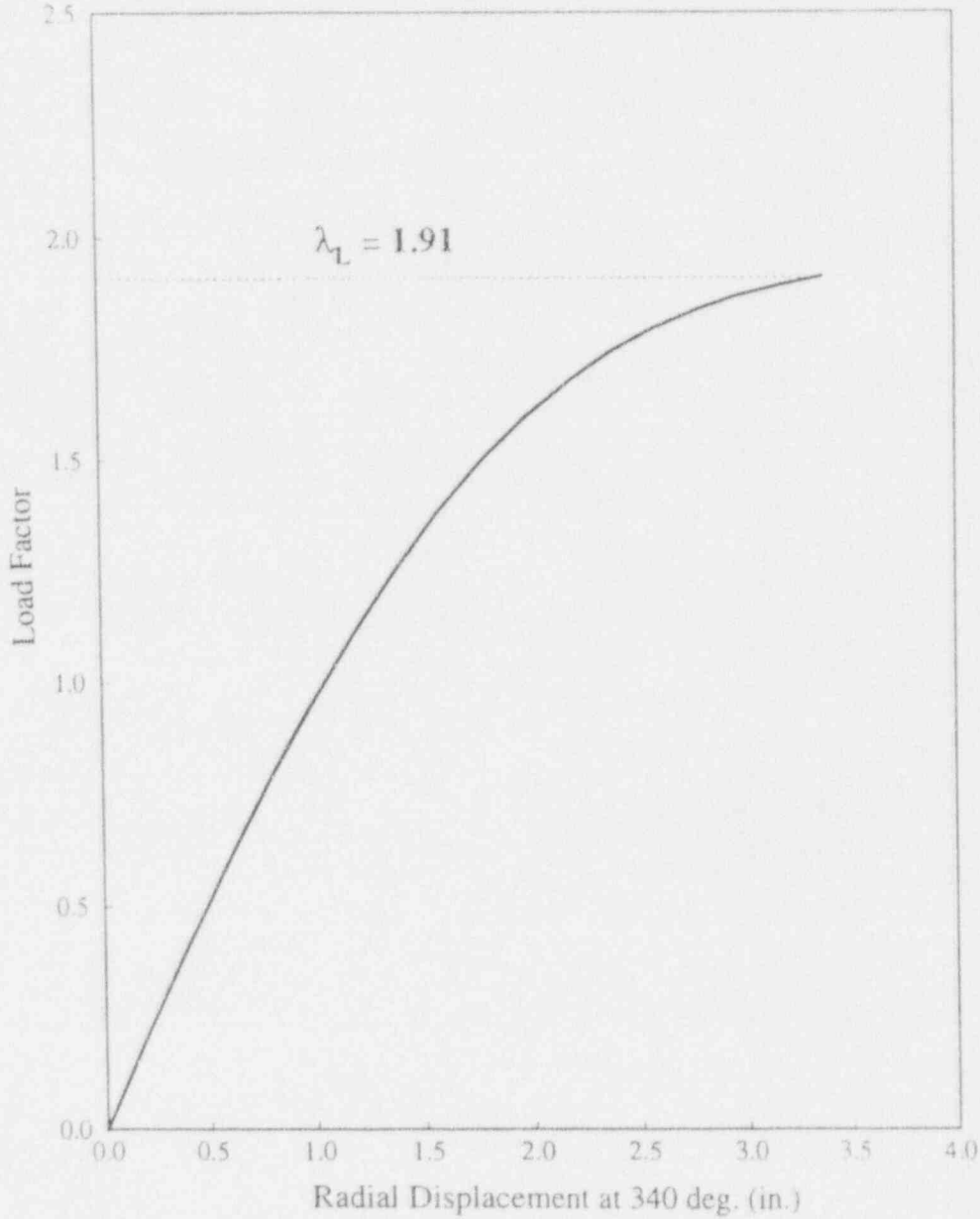

Fig 4.33 Load Deflection at the Base (Load Case 2)

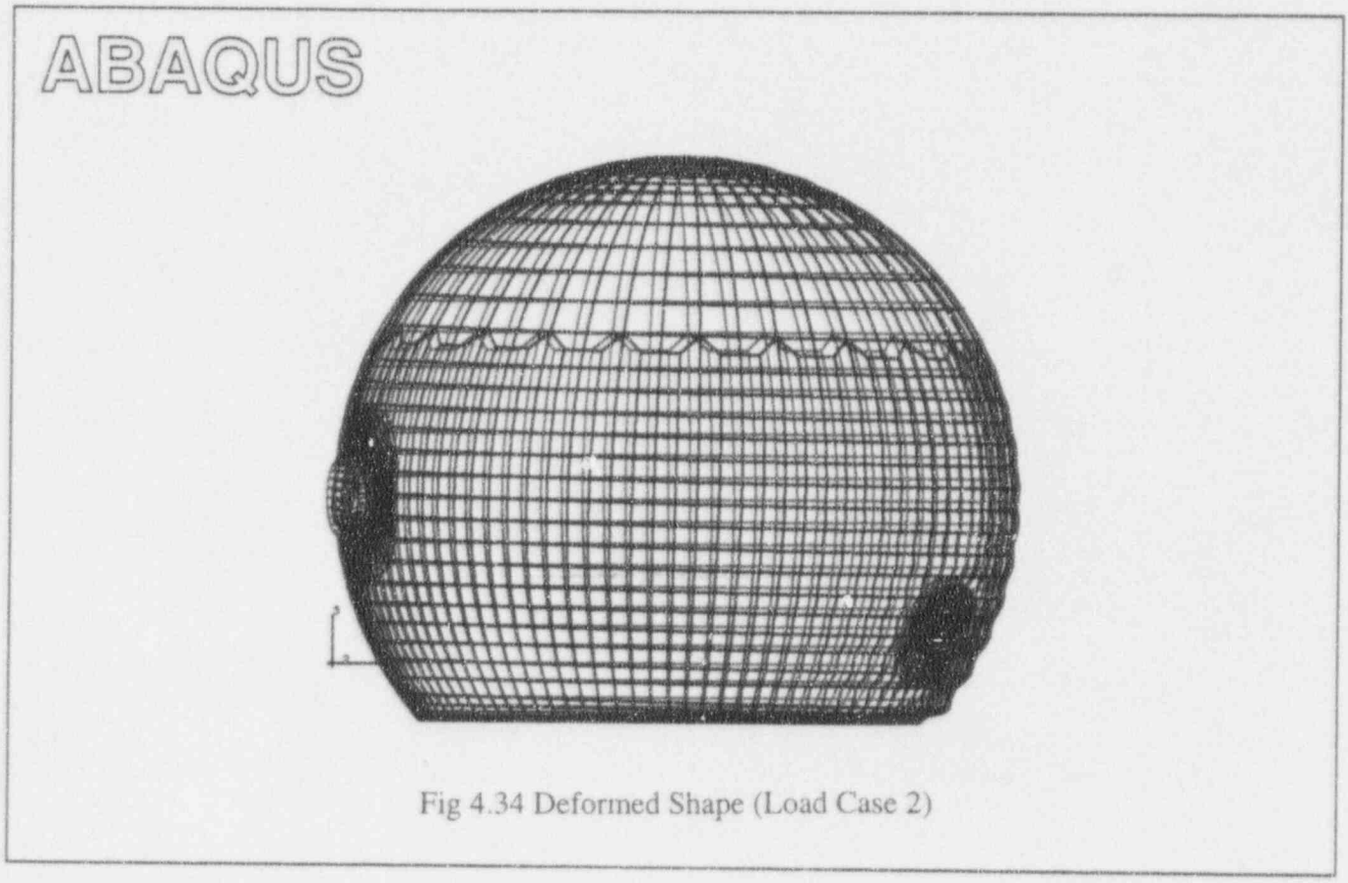

Fig 4.34 Deformed Shape (Load Case 2)

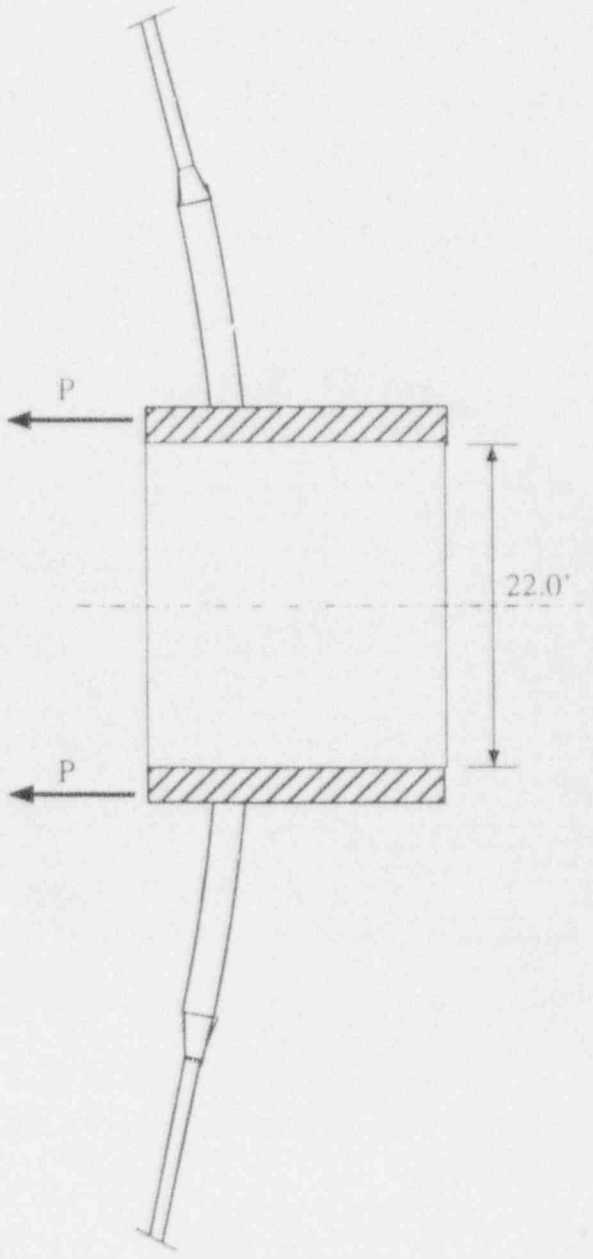

Fig 4.35 Reinforced Opening with Ring Load (Load Case 3)

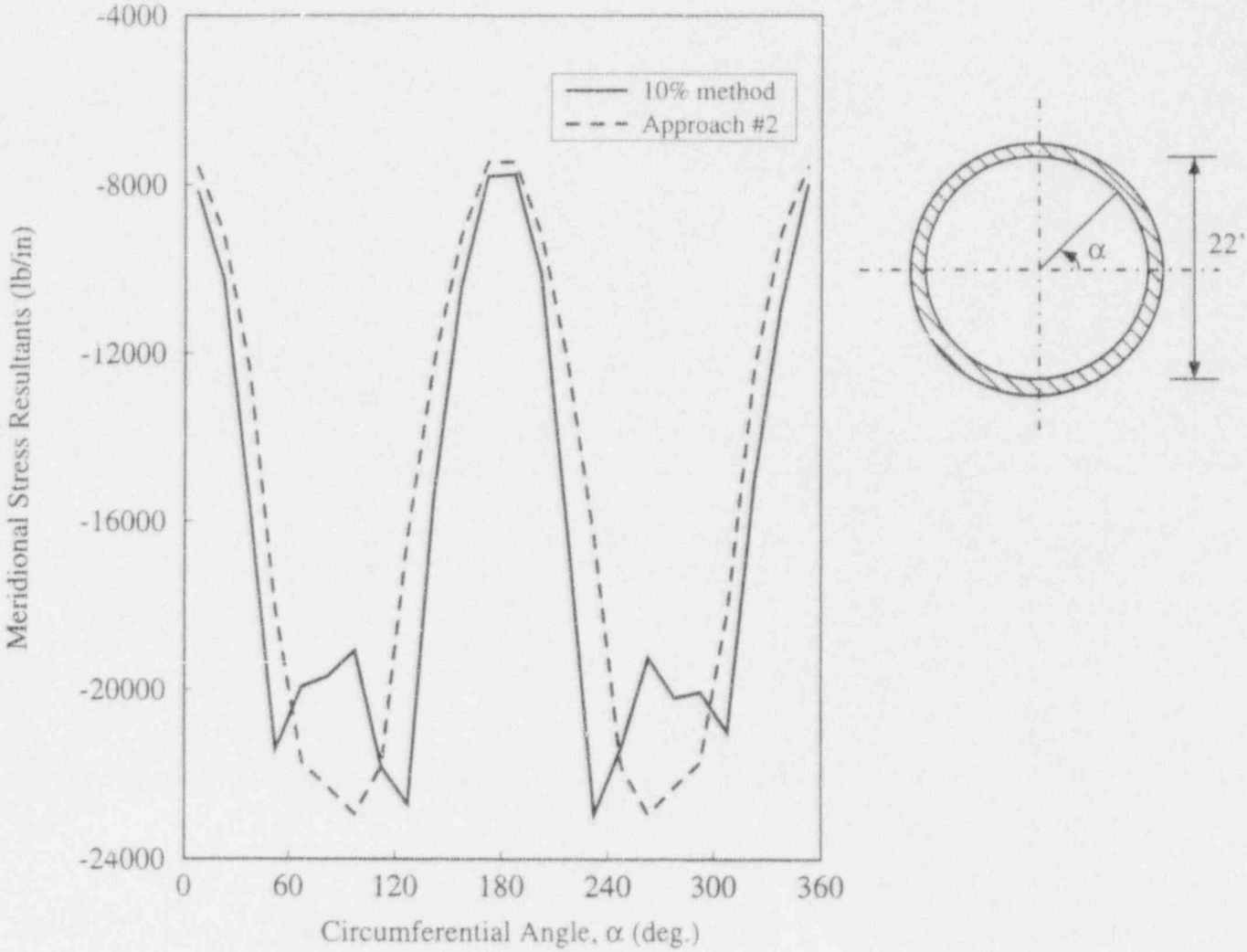

Fig 4.36 Meridional Stress Resultants Around the
Equipment Hatch Reinforcing Collar
(First Row of Elements in the Reinforcement)

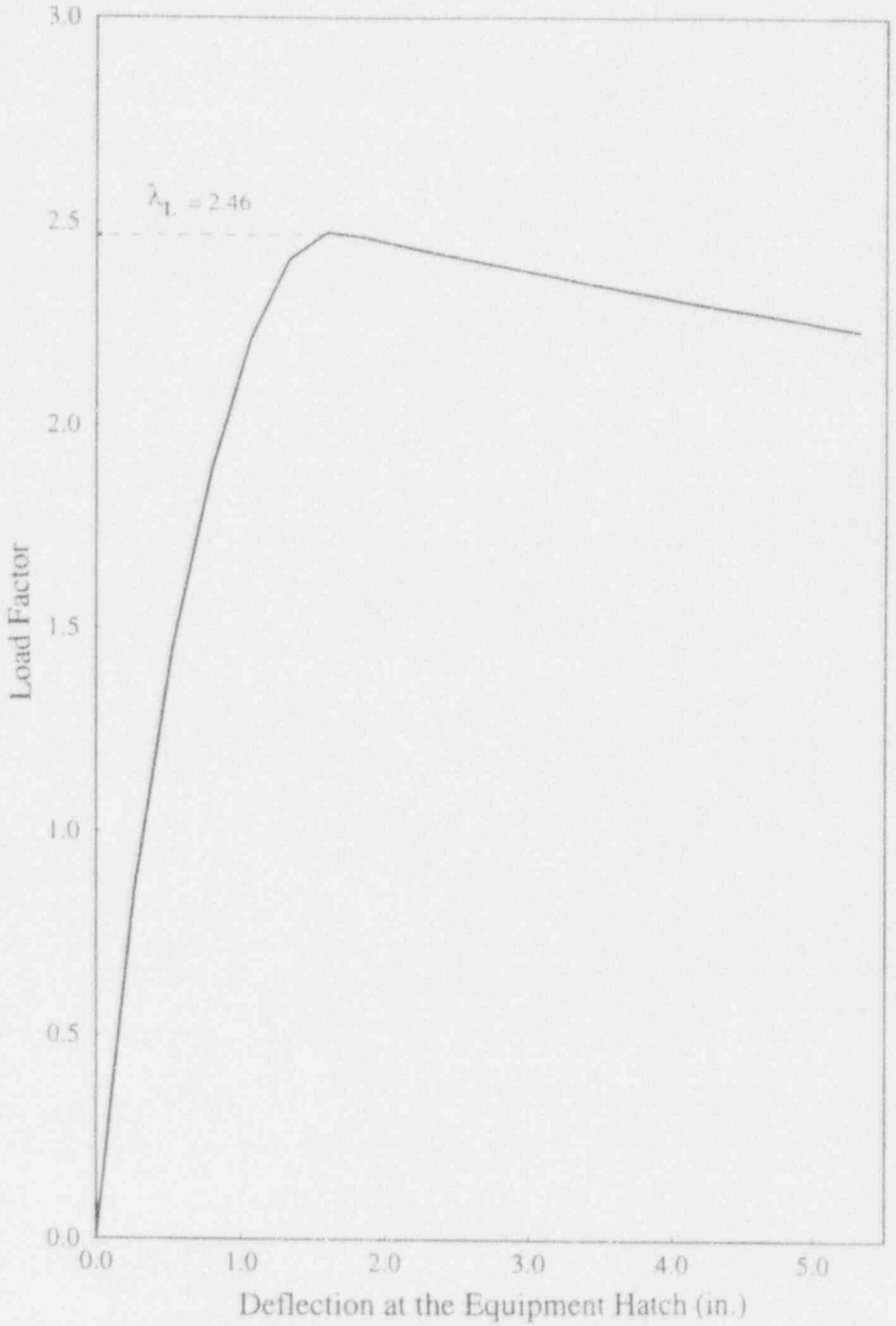

Fig 4.37 Load Deflection at the Equipment Hatch (Load Case 3)

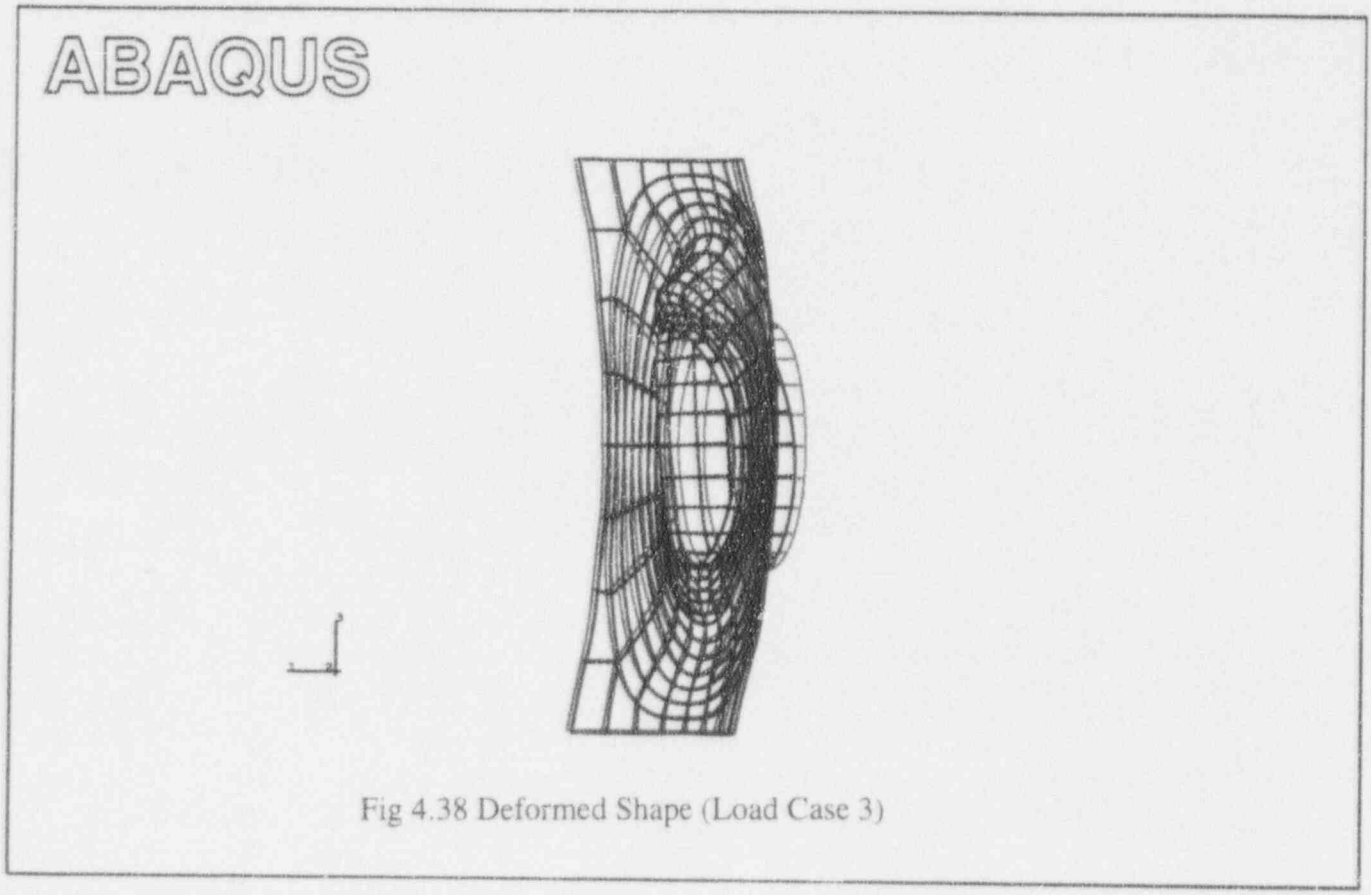

Fig 4.38 Deformed Shape (Load Case 3)

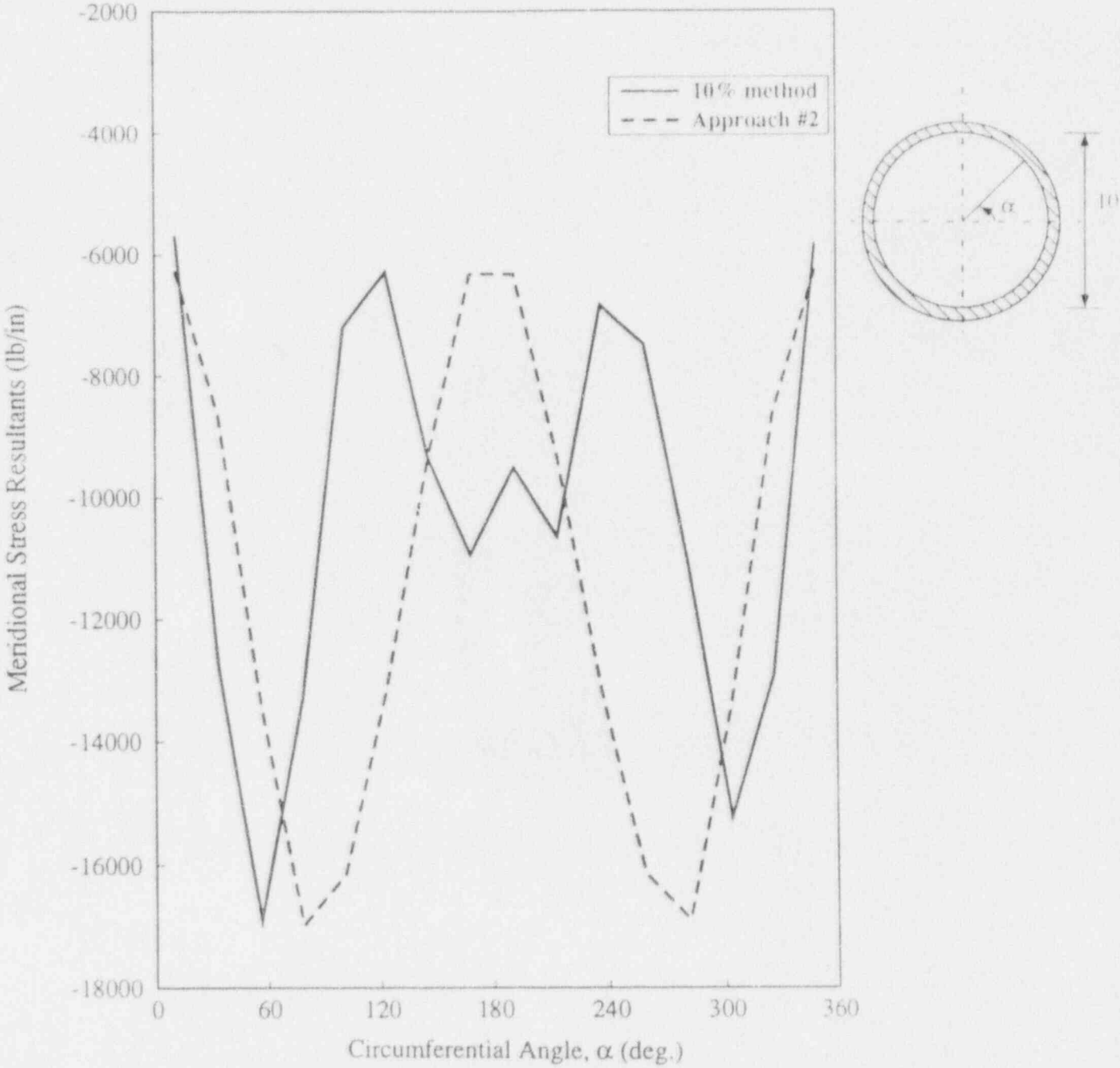

Fig 4.39 Meridional Stress Resultants Around the
Upper Air Lock Reinforcing Collar
(First Row of Elements in the Reinforcement)

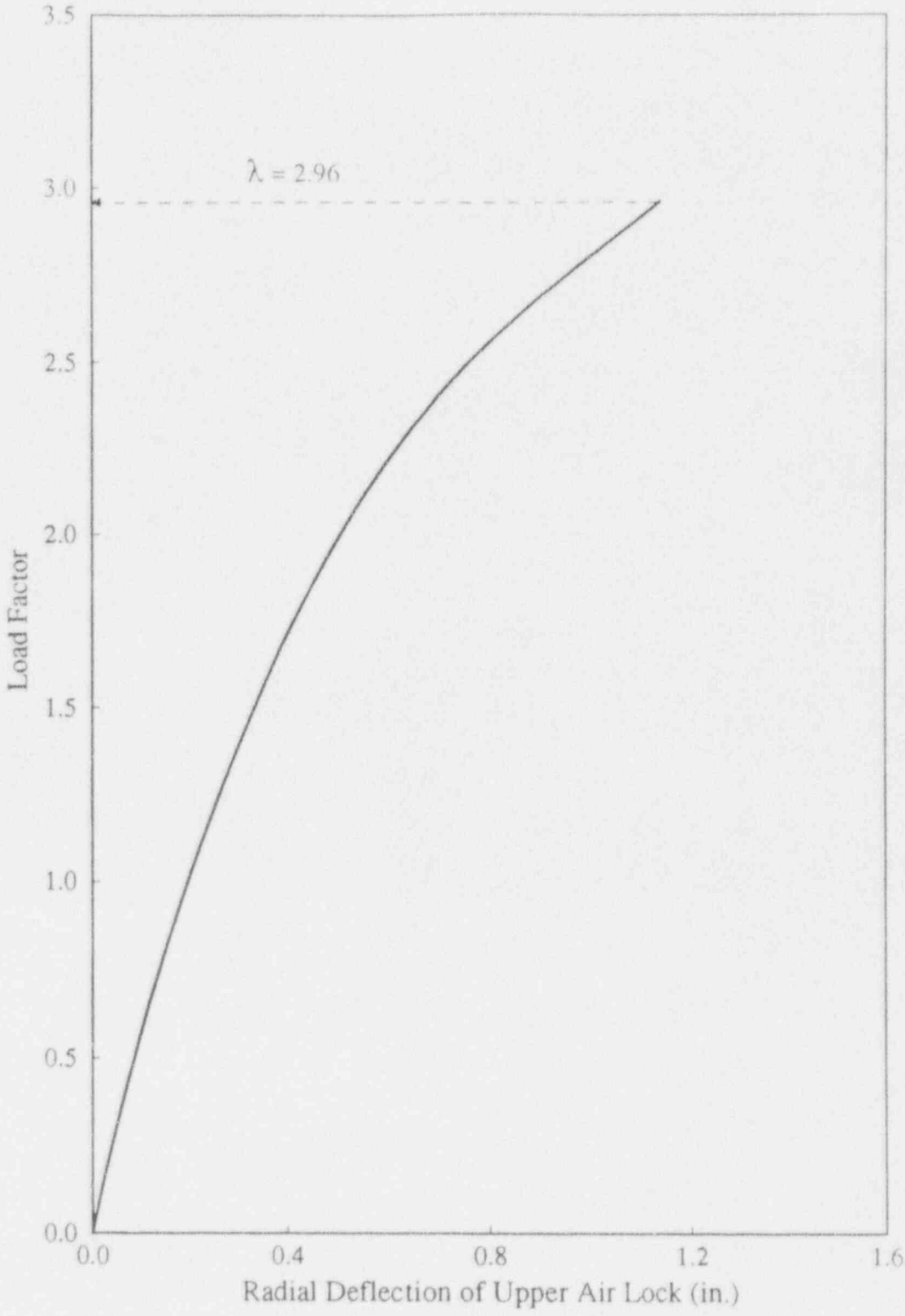

Fig 4.40 Load Deflection at the Upper Air Lock (Load Case 4)

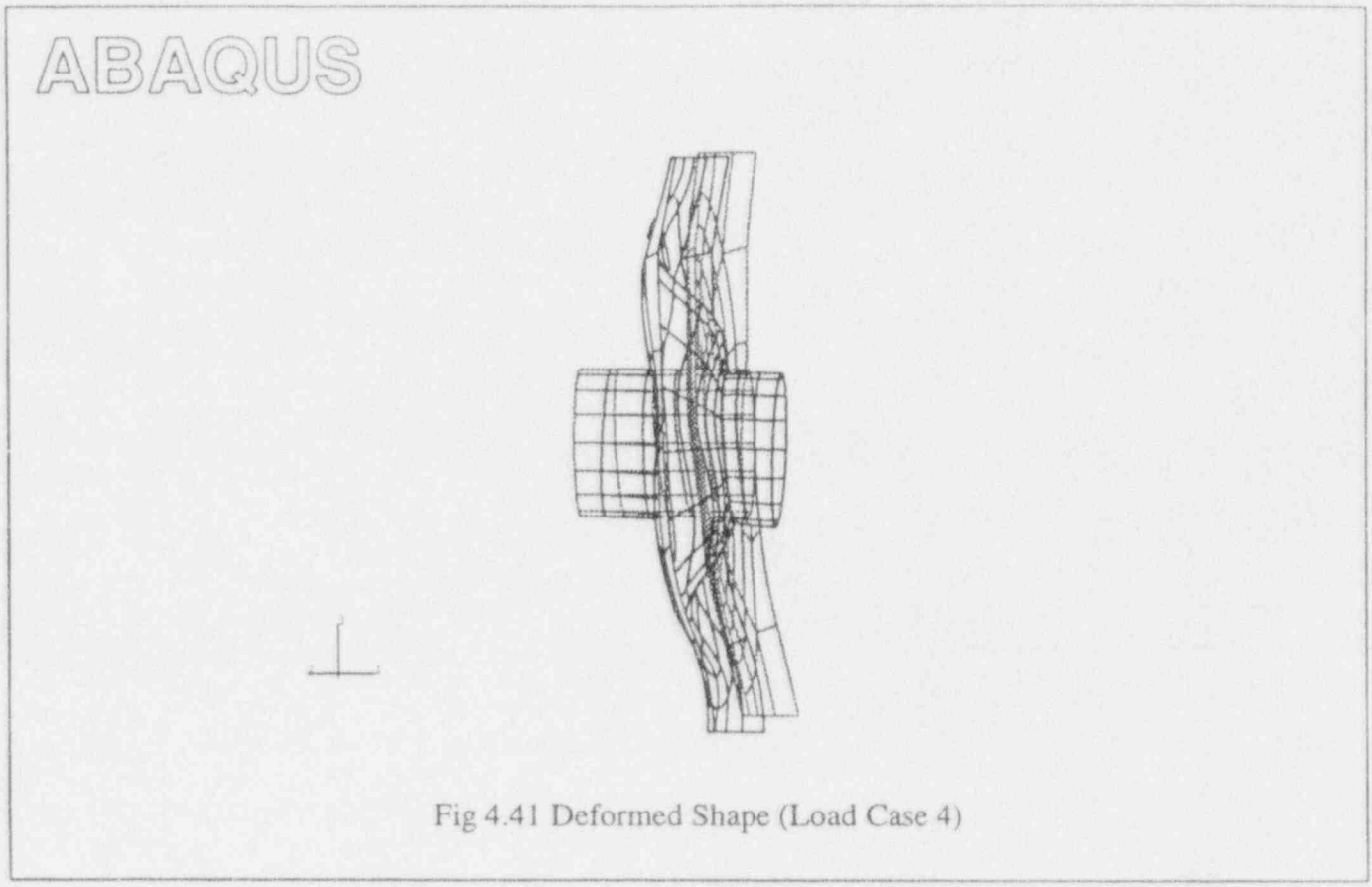

Fig 4.41 Deformed Shape (Load Case 4)

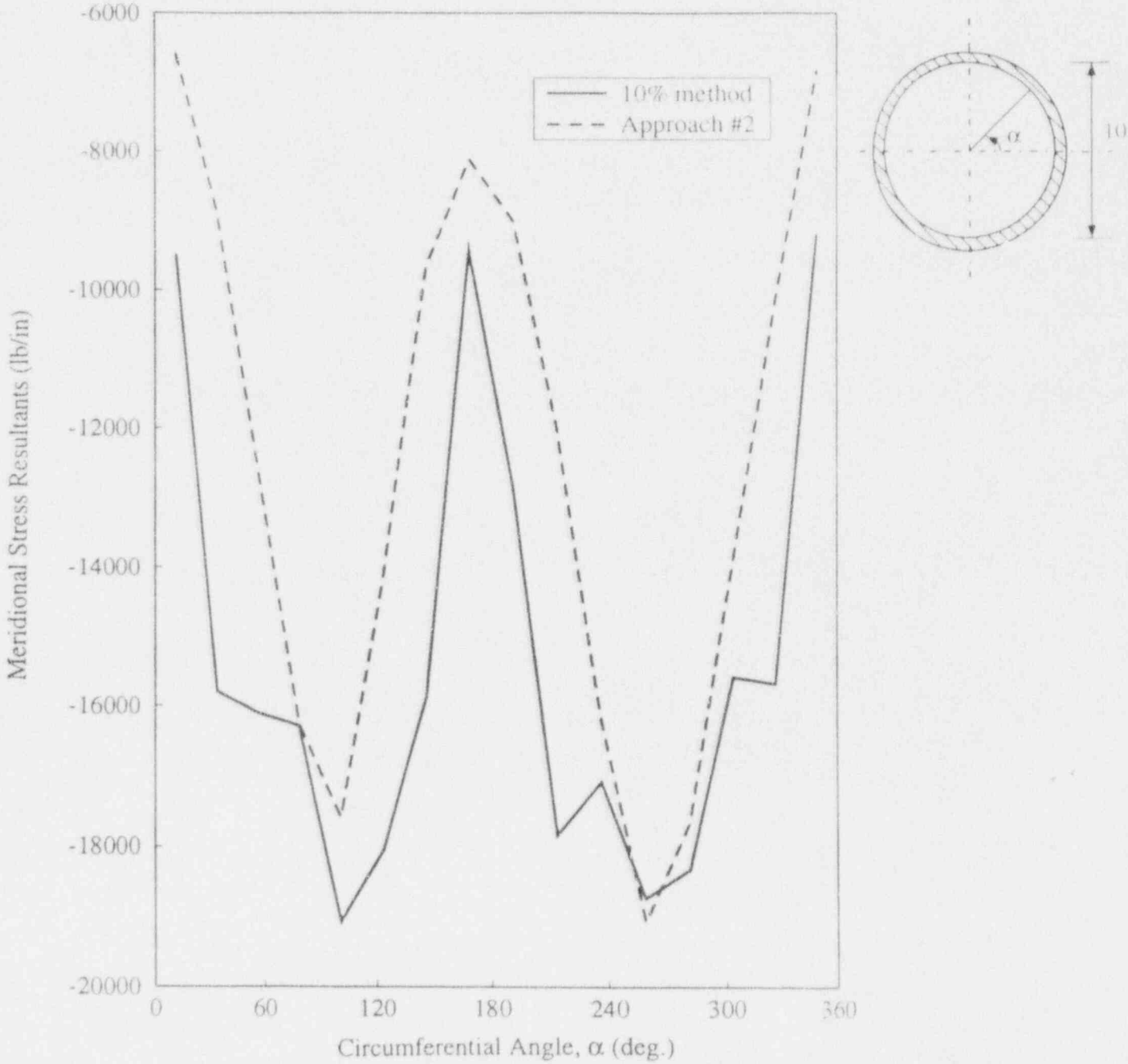

Fig 4.42 Meridional Stress Resultants Around the
Lower Air Lock Reinforcing Collar
(First Row of Elements in the Reinforcement)

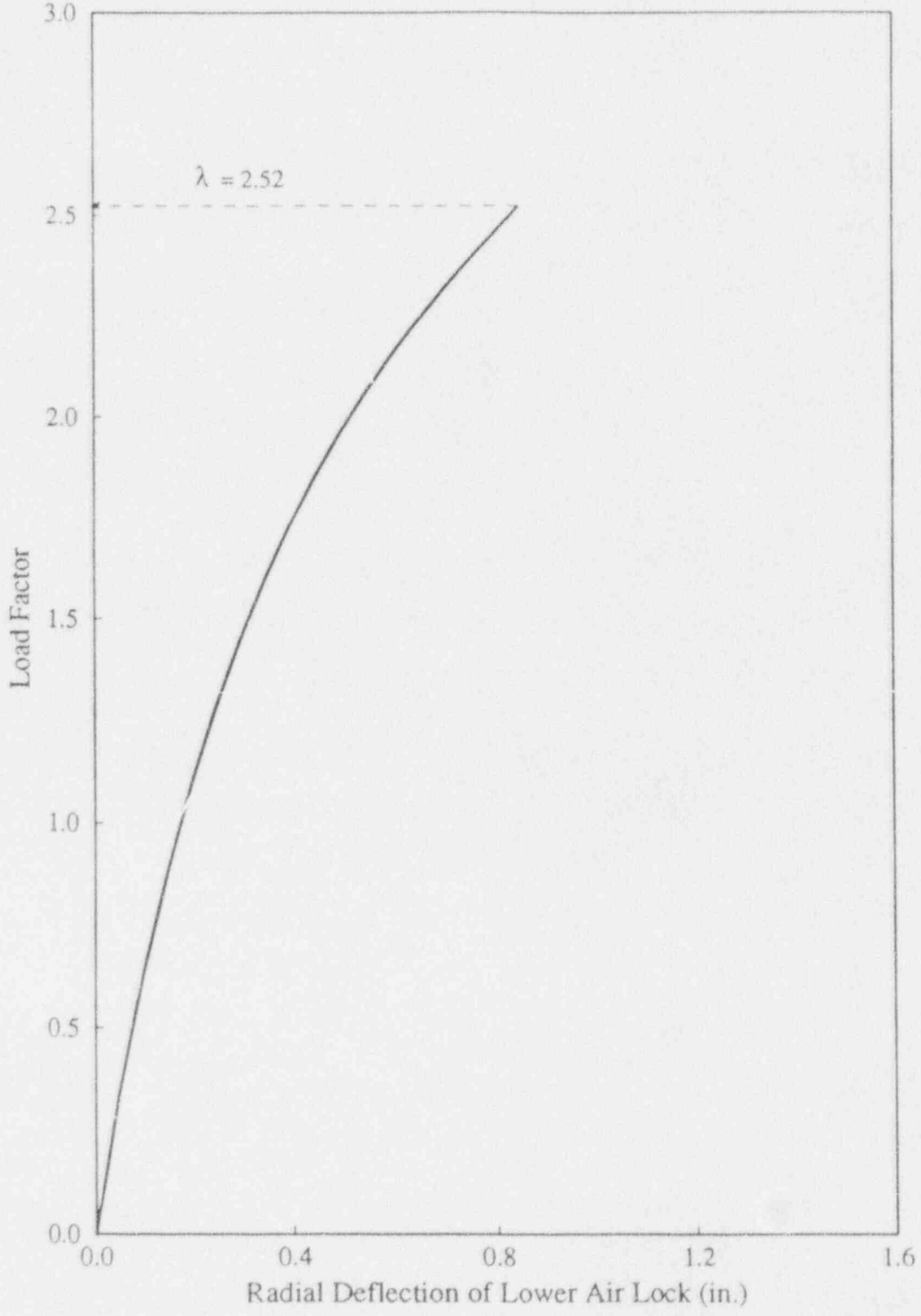

Fig 4.43 Load Deflection at the Lower Air Lock (Load Case 5)

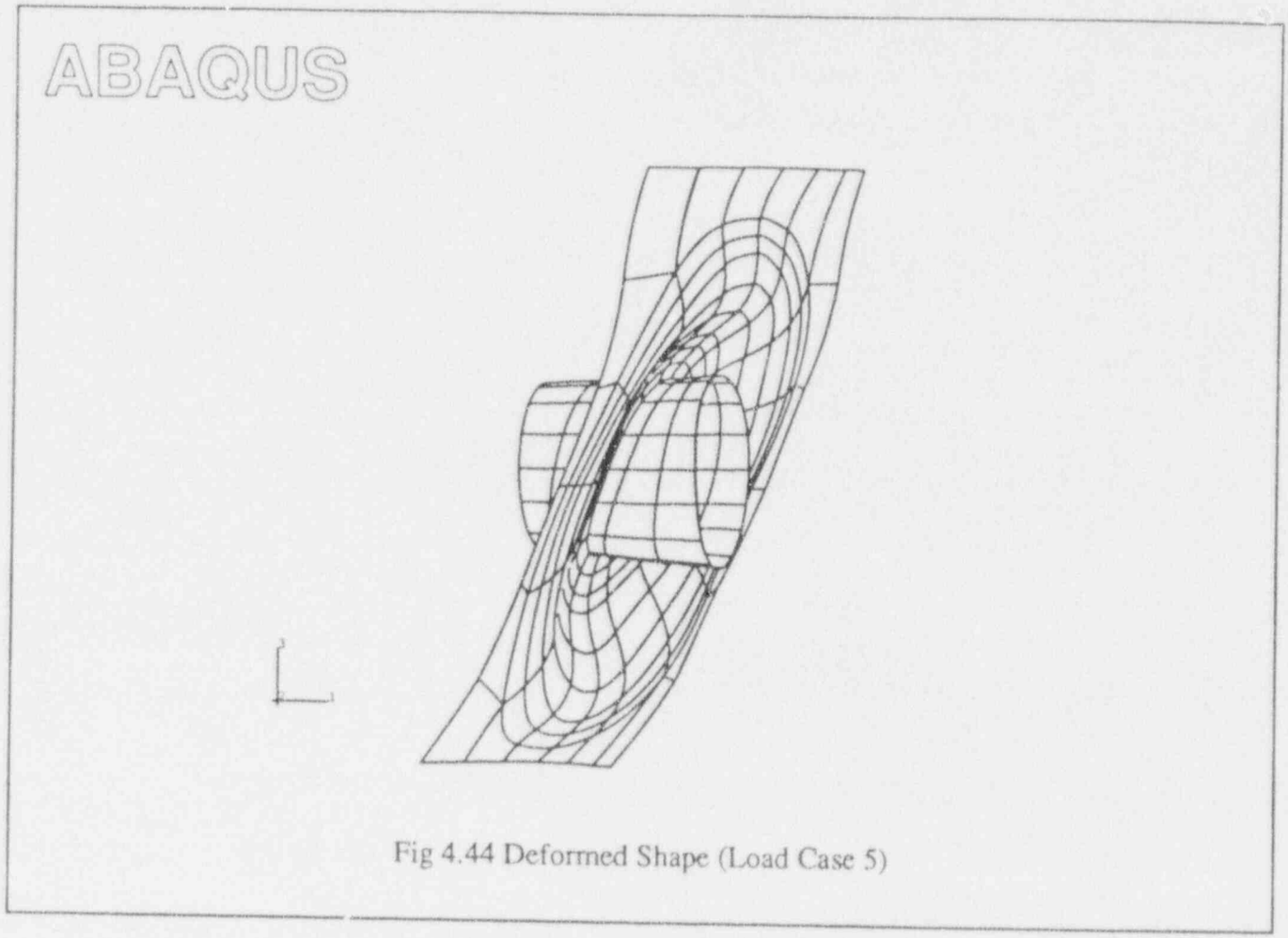

Fig 4.44 Deformed Shape (Load Case 5)

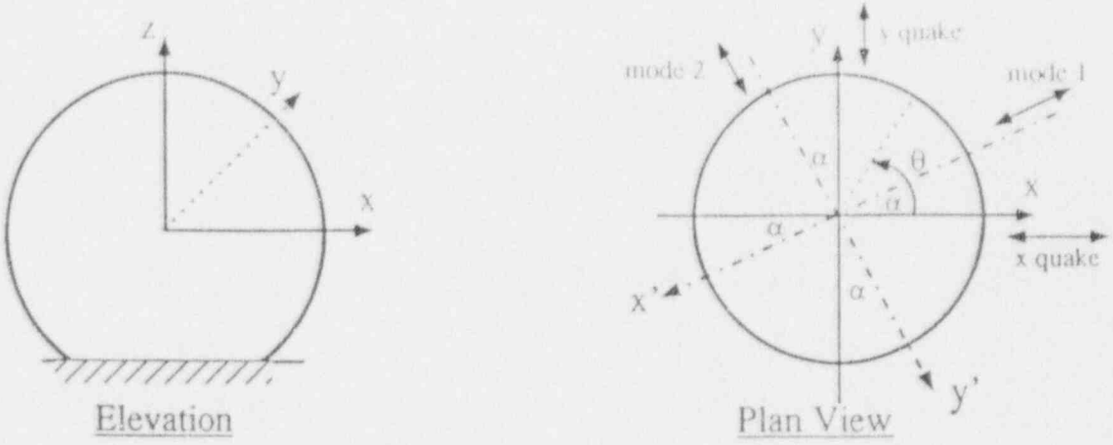

Fig A.1 Smooth Spherical Shell

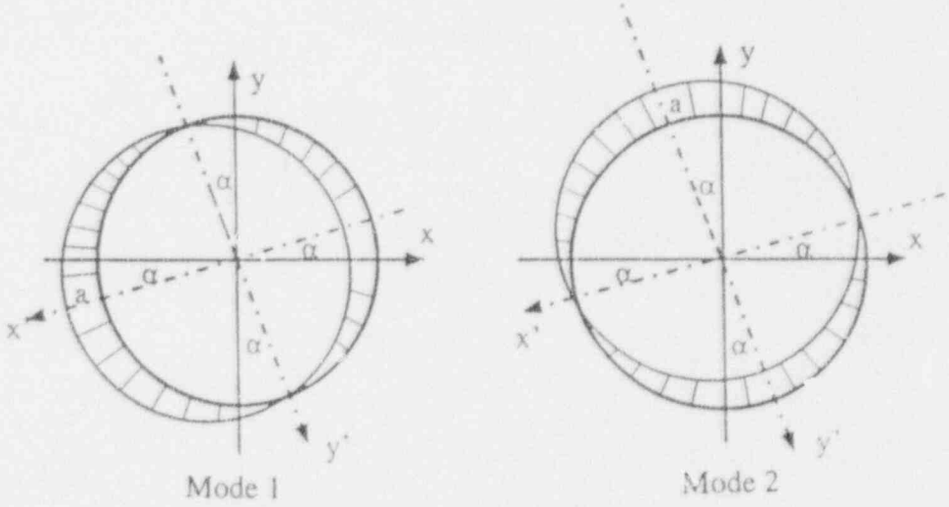

Fig A.2 Distribution of Meridional Stress Resultants
in Modes (1) & (2) at the Base

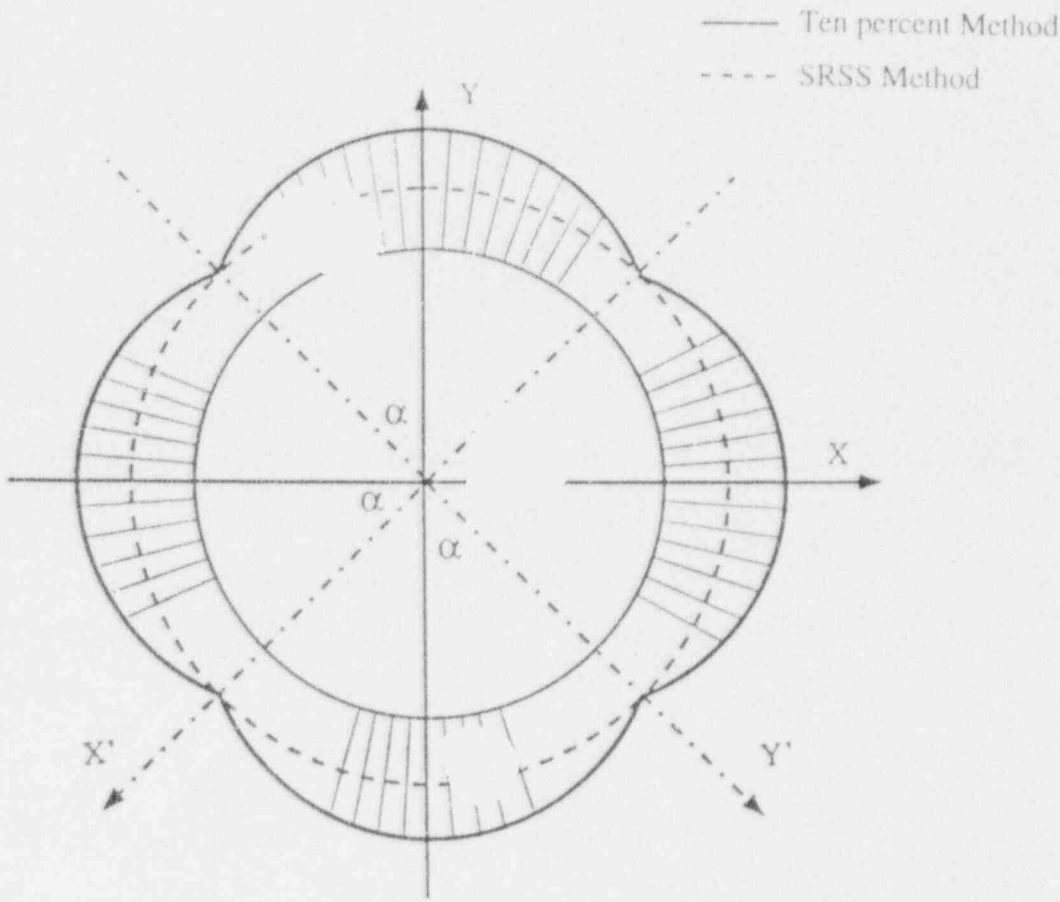

Fig A.3 Meridional Stress Resultants at the Base
(using the Ten Percent Method)

NRC FORM 335 (2-89) NRCM 1102, 3201, 3202

U.S. NUCLEAR REGULATORY COMMISSION

BIBLIOGRAPHIC DATA SHEET

(See instructions on the reverse)

1. REPORT NUMBER (Assigned by NRC, Add Vol., Supp., Rev., and Addendum Numbers, if any.)

NUREG/CR-6161
IS 5103

2. TITLE AND SUBTITLE

Buckling Evaluation of System 80+™ Containment

3. DATE REPORT PUBLISHED

MONTH	YEAR
August	1994

4. FIN OR GRANT NUMBER

L2582

5. AUTHOR(S)

L. Greimann, F. Fanous, S. Safar, R. Challa, D. Bluhm

6. TYPE OF REPORT

Technical

7. PERIOD COVERED *(Inclusive Dates)*

8. PERFORMING ORGANIZATION – NAME AND ADDRESS *(If NRC, provide Division, Office or Region, U.S. Nuclear Regulatory Commission, and mailing address; if contractor, provide name and mailing address.)*

Ames Laboratory
Iowa State University
Ames, Iowa 50011

9. SPONSORING ORGANIZATION – NAME AND ADDRESS *(If NRC, type "Same as above"; if contractor, provide NRC Division, Office or Region, U.S. Nuclear Regulatory Commission, and mailing address.)*

Division Of Engineering
Office of Nuclear Reactor Regulation
U.S. Nuclear Regulatory Commission
Washington, DC 20555

10. SUPPLEMENTARY NOTES

11. ABSTRACT *(200 words or less)*

The System 80+™ containment may be subjected to compressive forces which could cause it to become unstable. The stability of the containment shell under prescribed loading combinations was investigated with two analysis levels: axisymmetric and three dimensional. An axisymmetric shell model, including additional mass to account for penetrations and the spray header system, was analyzed using BOSOR4 and BOSOR5 finite difference codes. Loading combinations with pressure, temperature, self weight, and seismic satisfied the American Society of Mechanical Engineers (ASME) stress allowables. The buckling assessment was performed using the worst meridian assumption, including material nonlinearities and a sinusoidal axisymmetric imperfection. The minimum factor of safety for Service Level C was 2.35. A SSE seismic margin of 2.91 was calculated. The ABAQUS finite element code was selected for the three dimensional analysis and tested with classical and BOSOR solutions. The three dimensional model included the equipment hatch, two personnel airlocks, and additional mass for the spray system and small penetrations. Material nonlinearity and an axisymmetric sinusoidal imperfection were incorporated. A minimum factor of safety of 1.91 was predicted, which does not satisfy ASME Section NE3222.1 or Regulatory Guide 1.57. Code Case N-284 is satisfied. The analysis is conservative primarily because the SRSS 10% method provides a conservative estimate of modal coupling.

12. KEY WORDS/DESCRIPTORS *(List words or phrases that will assist researchers in locating the report.)*

13. AVAILABILITY STATEMENT

unlimited

14. SECURITY CLASSIFICATION

(This Page)
unclassified

(This Report)
unclassified

15. NUMBER OF PAGES

16. PRICE

NRC FORM 335 (2-89)

Federal Recycling Program

ISBN 0-16-045217-1

UNITED STATES
NUCLEAR REGULATORY COMMISSION
WASHINGTON, D.C. 20555-0001

OFFICIAL BUSINESS
PENALTY FOR PRIVATE USE, $300

SPECIAL FOURTH-CLASS RATE
POSTAGE AND FEES PAID
USNRC
PERMIT NO. G-67

120555139531 1 1AN1PL
US NRC-OADM
DIV FOIA & PUBLICATIONS SVCS
TPS-PDR-NUREG
2WFN-6F7
WASHINGTON DC 20555